A dynamic bactofilin cytoskeleton cooperates with an M23 endopeptidase to control bacterial morphogenesis

Sebastian Pöhl[1,*], Manuel Osorio-Valeriano[1,2,#,*], Emöke Cserti[1,*], Jannik Harberding[1], Rogelio Hernández-Tamayo[2,3,4], Jacob Biboy[5], Patrick Sobetzko[4,§], Waldemar Vollmer[5,6], Peter L. Graumann[3,4], Martin Thanbichler[1,2,4]

[1] Department of Biology, University of Marburg, Marburg, Germany
[2] Max Planck Institute for Terrestrial Microbiology, Marburg, Germany
[3] Department of Chemistry, University of Marburg, Marburg, Germany
[4] Center for Synthetic Microbiology (SYNMIKRO), Marburg, Germany
[5] Centre for Bacterial Cell Biology, Biosciences Institute, Newcastle University, Newcastle upon Tyne, United Kingdom
[6] Institute for Molecular Bioscience, The University of Queensland, Brisbane, Australia.

[#] Present address: Department of Cell Biology, Blavatnik Institute, Harvard Medical School, Boston, MA, USA.
[§] Present address: Faculty of Sciences and Technologies, Université de Lorraine, Nancy, France.

* These authors contributed equally to this work.

Address correspondence to
Martin Thanbichler (thanbichler@uni-marburg.de)

Keywords
Cell wall, peptidoglycan, cell shape, autolysin, LytM domain, bacterial cell division, divisome, elongasome, MreB, RodZ, CRIPSR interference, CRISPRi, dCas9

Abstract

Bactofilins have emerged as a widespread family of cytoskeletal proteins with important roles in bacterial morphogenesis, but their precise mode of action is still incompletely understood. In this study, we identify the bactofilin cytoskeleton as a key regulator of cell growth in the stalked budding alphaproteobacterium *Hyphomonas neptunium*. We show that, in this species, bactofilin polymers localize dynamically to the stalk base and the bud neck, with their absence leading to unconstrained growth of the stalk and bud compartments, indicating a central role in the spatial regulation of cell wall biosynthesis. Database searches reveal that in a range of different species bactofilin genes are clustered with genes for cell wall hydrolases of the M23 peptidase family, suggesting a functional connection between these two types of proteins. In support of this notion, we find that the *H. neptunium* M23 peptidase homolog LmdC interacts directly with bactofilin *in vitro* and is required for proper cell shape *in vivo*. Complementary studies in the spiral-shaped alphaproteobacterium *Rhodospirillum rubrum* again reveal a close association of its bactofilin and LmdC homologs, which co-localize at the inner curve of the cell, modulating the degree of cell curvature. Collectively, these findings demonstrate that bactofilins and M23 peptidases form a conserved functional module that promotes local changes in the mode of cell wall biosynthesis, thereby driving cell shape determination in morphologically complex bacteria.

Introduction

16 Bacteria come in a variety of different cell shapes, which can be further modified by the formation of
17 cellular extensions such as branches or stalks (Kysela et al., 2016; Yang et al., 2016). Their morphology can
18 change as a function of the cell cycle or in response to environmental cues to ensure optimal fitness in
19 the given ecological niche or growth conditions (van Teeseling et al., 2017; Yang et al., 2016). In the vast
20 majority of species, cell shape is determined by the peptidoglycan cell wall, a complex macromolecule
21 composed of glycan chains that are crosslinked by short peptides (Typas et al., 2012; Vollmer et al., 2008).
22 The synthesis of this mesh-like structure is achieved by an array of synthetic and lytic enzymes that are
23 typically combined into multi-protein complexes and associated with regulatory factors and cytoskeletal
24 elements to facilitate the coordination and spatiotemporal regulation of their activities (Egan et al., 2020;
25 Rohs and Bernhardt, 2021).

26 Basic spherical, rod-like and hyphal shapes are generated by the combined action of the cell division and
27 cell elongation machinery (Margolin, 2009; Rohs and Bernhardt, 2021). In most bacteria, cell division is
28 executed by the divisome, which is organized by the tubulin homolog FtsZ and mediates cell constriction
29 and the synthesis of the new cell poles prior to cytokinesis (McQuillen and Xiao, 2020). Cell elongation, by
30 contrast, can be achieved by various types of cell wall-biosynthetic complexes, including the so-called
31 elongasome, which is organized by the actin homolog MreB and mediates the dispersed incorporation of
32 new cell wall material along the lateral cell walls (Shi et al., 2018), or different cell pole-associated com-
33 plexes that promote polar growth of the cell body (Brown et al., 2011). More complex cell shapes are
34 generated with the help of accessory systems that either modulate the activity of the generic cell elon-
35 gation machinery or have peptidoglycan biosynthetic activity on their own, thereby locally modifying the
36 structure of the peptidoglycan layer (Taylor et al., 2019).

37 A particularly widespread family of cytoskeletal proteins implicated in cell shape modification are the
38 bactofilins. They are characterized by a conserved central Bactofilin A/B domain (InterPro ID: IPR007607;
39 Paysan-Lafosse et al., 2022) with a barrel-like β-helical fold that is typically flanked by short disordered
40 terminal regions (Kühn et al., 2010; Shi et al., 2015; Vasa et al., 2015). Bactofilins polymerize spontane-
41 ously without the need for nucleotide cofactors (Koch et al., 2011; Kühn et al., 2010), driven by head-to-
42 head and tail-to-tail interactions between the core domains of neighboring molecules (Deng et al., 2019).
43 Lateral interactions between individual protofilaments can then give rise to higher-order assemblies, such
44 as bundles or two-dimensional sheets (Kühn et al., 2010; Vasa et al., 2015; Zuckerman et al., 2015).
45 Previous work has suggested that bactofilin polymers typically associate with the inner face of the cyto-

46 plasmic membrane and localize to regions of high membrane curvature (Caccamo et al., 2020; Hay et al.,
47 1999; Kühn et al., 2010; Lin et al., 2017; Taylor et al., 2020). These structures have been co-opted as
48 localization determinants and assembly platforms by several different morphogenetic systems.

49 For instance, bactofilin homologs were reported to contribute to rod-shape maintenance in *Myxococcus*
50 *xanthus* (Koch et al., 2011), the establishment of helical cell shape in the human pathogen *Helicobacter*
51 *pylori* (Sycuro et al., 2010; Taylor et al., 2020) as well as the modulation of cell helicity in the spiral-shaped
52 bacterium *Leptospira biflexa* (Jackson et al., 2018). Apart from modulating general cell shape, they were
53 found to have an important role in the formation of cellular extensions known as stalks, which are wide-
54 spread among alphaproteobacterial species (Wagner and Brun, 2007). Stalks are elongated protrusions of
55 the cell envelope that are filled with a thin thread of cytoplasm and grow through zonal incorporation of
56 cell wall material at their base (Aaron et al., 2007; Randich and Brun, 2015). In *Caulobacter crescentus* and
57 *Asticcacaulis biprosthecum*, bactofilin polymers were shown to localize to the stalk base to direct proper
58 stalk formation. In *C. crescentus*, they recruit a cell wall synthase that contributes to stalk elongation, with
59 their absence leading to a reduction in stalk length (Kühn et al., 2010). In *A. biprosthecum*, by contrast,
60 bactofilin acts as a central topological regulator that is required to efficiently initiate stalk formation and
61 limit peptidoglycan biosynthesis to the stalk base. Its absence leads to the development of pseudostalks,
62 which are much shorter and wider than normal stalks and irregularly shaped, likely due to unrestrained
63 peptidoglycan biosynthesis through the entire stalk envelope (Caccamo et al., 2020).

64 While stalks are often accessory structures with highly specialized functions (Klein et al., 2013; Persat et
65 al., 2014; Wagner and Brun, 2007), stalked budding bacteria such as *Hyphomonas neptunium* and other
66 members of the *Hyphomonadaceae* and *Hyphomicrobiaceae* use them as integral parts of the cell with
67 key roles in cell growth and division (Moore, 1981). *H. neptunium* has a biphasic life cycle (Wali et al.,
68 1980), in which a non-replicative, motile swimmer cell sheds its single polar flagellum and differentiates
69 into a replicative, sessile stalked cell (**Figure 1—figure supplement 1**). Unlike most widely studied model
70 species, it does not divide by binary fission but instead produces new offspring through the formation of
71 buds at the tip of the stalk. As the terminal stalk segment gradually dilates, a flagellum is formed at the
72 pole opposite the stalk. After DNA replication and translocation of one of the sister chromosomes through
73 the stalk into the bud compartment (Jung et al., 2019), cytokinesis occurs at the bud neck, releasing a new
74 swimmer cell. While the newborn cell first needs to differentiate into stalked cells to start replication, the
75 stalked mother cell restores the stalk and then immediately re-enters the next budding cycle (Jung et al.,
76 2019; Wali et al., 1980). The developmental program of *H. neptunium* involves several switches in the

77 pattern of peptidoglycan biosynthesis (Cserti et al., 2017). After birth, swimmer cells increase in size by
78 dispersed incorporation of new cell wall material throughout the cell body. Stalk formation is then
79 achieved by zonal growth at the stalk base, followed by localized dispersed growth of the stalk-terminal
80 bud compartment and, finally, zonal peptidoglycan synthesis at the site of cell division. The pattern of
81 new cell wall synthesis is similar to the localization pattern of elongasome components (Cserti et al., 2017),
82 suggesting the involvement of this machinery in all growth phases. However, the underlying regulatory
83 mechanisms are still unknown.

84 In this study, we identify the bactofilin cytoskeleton as a central player in the regulation of cell growth of
85 *H. neptunium*. We show that the lack of bactofilins causes severe morphological defects, resulting from
86 unconstrained growth of the stalk and bud compartments. In line with this finding, bactofilin polymers
87 localize dynamically to the stalk base and then to the incipient bud neck prior to the onset of bud for-
88 mation, acting as a barrier that retains the cell wall biosynthetic machinery in the respective growth zones.
89 Notably, in a broad range of species, bactofilin genes lie adjacent to genes encoding putative M23 pepti-
90 dases. We show that the corresponding *H. neptunium* homolog, LmdC, is an essential bitopic membrane
91 protein with peptidoglycan hydrolase activity that interacts directly with bactofilin through its N-terminal
92 cytoplasmic tail. Its CRISPRi-mediated depletion also results in unconstrained cell growth, confirming its
93 functional connection to bactofilin. The conservation of this interaction is further verified by studies of
94 the spiral-shaped alphaproteobacterium *Rhodospirillum rubrum*. We show that the bactofilin and LmdC
95 homologs of this species co-localize at the inner curve of the cell, forming filamentous assemblies that
96 modulate the degree of cell curvature. Their interaction is abolished by amino acid exchanges in the
97 cytoplasmic tail of LmdC, confirming a key role of this region in the recruitment of LmdC. Together, these
98 results demonstrate a conserved functional interaction between bactofilins and M23 peptidases that is
99 important for the control of cell growth in morphologically complex bacteria.

Results

100 **The bactofilin cytoskeleton is required for cell shape determination in *H. neptunium***

101 The *H. neptunium* chromosome contains two open reading frames that encode bactofilin homologs,
102 HNE_0444 and HNE_2629 (Badger et al., 2006). Reciprocal BLAST analysis using the two bactofilins
103 described in the close relative *C. crescentus* identified HNE_2629 as a potential ortholog of *C. crescentus*
104 BacA (43% identity, 60% similarity). By contrast, HNE_0444 was only distantly related (<30% identity) to
105 either of the two proteins. Based on these results, we propose to designate the two bactofilin homologs
106 of *H. neptunium* BacA (HNE_2629) and BacD (HNE_0444), respectively. *bacA* forms a putative bicistronic
107 operon with *lmdC*, an essential gene encoding an M23 peptidase homolog (Cserti et al., 2017) (**Figure 1A**).
108 The two genes overlap by 17 base pairs, suggesting that their expression is closely coupled. *bacD*, by
109 contrast, is not part of an operon. Both BacA and BacD display the typical architecture of bactofilins, with
110 a central polymerization domain flanked by short non-structured N- and C-terminal regions (**Figure 1B**).

111 To investigate the role of bactofilins in *H. neptunium*, we generated mutant strains in which *bacA* and
112 *bacD* were deleted either individually or in combination and analyzed their phenotypes (**Figure 1**). The
113 Δ*bacA* and Δ*bacAD* cells showed severe morphological defects, as reflected by irregularly shaped, elon-
114 gated and/or oversized cells, buds directly fused with the mother cell body, branched stalks, and multiple
115 wide protrusions that emerged from the cells in an apparently random fashion (**Figure 1C-E**), reminiscent
116 of the pseudostalks reported for a bactofilin-deficient *A. biprosthecum* mutant (Caccamo et al., 2020).
117 Surprisingly, these growth defects did not have any major defects on the doubling time (**Figure 1—figure**
118 **supplement 2F**). The wild-type phenotype could be largely restored by expressing an ectopic copy of *bacA*
119 under the control of a copper-inducible promoter, even though BacA accumulated to lower-than-normal
120 levels under this condition, confirming the absence of polar effects (**Figure 1—figure supplement 2A-D**).
121 The deletion of *bacD*, by contrast, did not cause any obvious cell shape defects (**Figure 1C,E,F** and **Figure**
122 **1—figure supplement 2E**). Moreover, neither *bacD* deletion nor *bacD* overexpression had any influence
123 on the proportion of distorted or amorphous cells in the Δ*bacA* background (**Figure 1C,F** and **Figure 1—**
124 **figure supplement 2C,F**). These results demonstrate that BacA has a critical role in the regulation of cell
125 growth in *H. neptunium*, whereas BacD might be an auxiliary factor of so-far unknown function, similar to
126 BacB in *C. crescentus* (Kühn et al., 2010).

127 To obtain more insight into the dynamics of cell growth in the Δ*bacA* mutant and identify the initial pheno-
128 typic defects induced upon BacA depletion, we imaged a conditional *bacA* mutant after its transfer from
129 permissive to restrictive conditions on an agarose pad (**Figure 2A,B**). Following cells at the swimmer-to-

130 stalked cell transition, we observed that stalk formation initially proceeded as in the wild-type strain.
131 However, as BacA was gradually depleted, stalk elongation ceased and the stalk structure started to widen
132 and eventually develop multiple bulges that kept on expanding in an apparently uncontrolled manner.
133 Thus, BacA appears to be required to maintain the polar growth zone at the stalk base, with its absence
134 leading to unconstrained growth of the stalk cell wall. To follow the fate of bactofilin-deficient cells over
135 a prolonged period of time, we monitored Δ*bacAD* cells in a flow-cell system, which ensured optimal
136 nutrient supply throughout the course of the experiment and led to a looser packing of cells, thereby
137 facilitating their visual analysis (**Figure 2—figure supplement 1** and **Figure 2—video 1**). In this setup, cells
138 again started growth by the formation of irregularly shaped stalks that started to branch, with branches
139 developing either into extensive hyphal-like structures or large, amorphous compartments that may
140 represent morphologically aberrant buds. At irregular intervals, cells divided at the junctions between
141 hyphal and bulged cellular segments, releasing smaller amorphous fragments and, occasionally, also cells
142 with close-to-normal morphology. Wild-type cells, by contrast, showed the usual growth pattern when
143 cultivated under these conditions (**Figure 2—video 1**). Together, these results underscore the importance
144 of BacA in the spatiotemporal control of cell growth in *H. neptunium*.

145 To obtain more detailed information about the dynamics of cell wall biosynthesis in the absence of bacto-
146 filins, we performed pulse-labeling studies with the fluorescent D-amino acid HADA, which is rapidly incor-
147 porated into peptidoglycan when added to the culture medium, thus marking regions of ongoing cell wall
148 biosynthesis (Kuru et al., 2015). Wild-type cells showed the typical succession of growth modes, with
149 dispersed growth in swimmer cells, zonal growth at the stalk base in stalked cells and localized dispersed
150 growth in the nascent bud (**Figure 2C**). In the Δ*bacAD* background, by contrast, this switch in the growth
151 modes was abolished. Cells with close-to-normal morphology that had just initiated stalk formation still
152 showed a distinct fluorescent focus at the stalked pole, suggesting that the initial recruitment of the
153 machinery responsible for stalk formation occurred in a bactofilin-independent manner. However, all
154 other cell types, including amorphous cells with aberrant stalk- and bud-like extensions, only displayed
155 diffuse fluorescence, which points to uncontrolled growth through dispersed incorporation of new pepti-
156 doglycan throughout the entire cell envelope. These findings support the notion that the bactofilin cyto-
157 skeleton is required to limit cell wall biosynthesis to the different growth zones of *H. neptunium*.

158 **The *H. neptunium* bactofilin homologs assemble into stable filamentous structures**

159 Despite their severe cell shape defects, the Δ*bacA* and Δ*bacAD* mutants showed close-to-normal growth
160 rates. Moreover, muropeptide analysis showed that the global composition of their peptidoglycan re-

161 mained essentially unchanged (**Figure 2—figure supplement 2B** and **Figure 2—Dataset 1**). These findings
162 suggested that BacA might affect cell wall composition at a local scale or act mainly by modulating the
163 activity of the generic cell elongation machinery. To further investigate the role of bactofilins in *H. nep-*
164 *tunium*, we first aimed to verify the ability of the proteins to assemble into polymeric scaffolds. A model
165 of the structure of BacA generated with AlphaFold-Multimer (Evans et al., 2022) suggested that the
166 protein adopted a β-helical fold and polymerized through head-to-head and tail-to-tail interactions among
167 different subunits (**Figure 3A**), as revealed previously in experimental studies (Deng et al., 2019; Shi et al.,
168 2015). Consistent with this prediction, purified BacA produced a mixture of long filaments, filament bun-
169 dles and two-dimensional polymeric sheets *in vitro*, which could be readily visualized by transmission
170 electron microscopy (**Figure 3B**). Moreover, upon heterologous co-expression in *Escherichia coli*, fluores-
171 cently tagged derivatives of BacA and BacD co-localized into extended filamentous structures that were
172 associated with the cell envelope (**Figure 3C** and **Figure 3—figure supplement 1A**). The BacA fusion
173 formed qualitatively similar structures when produced alone, whereas the BacD fusion condensed into
174 tight foci in the absence of BacA (**Figure 3—figure supplement 1B,C**). These results confirm the polymeric
175 nature of bactofilin assemblies in *H. neptunium* and suggest that BacA and BacD interact with each other
176 *in vivo*.

177 **Bactofilins localize dynamically to the boundaries of the *H. neptunium* growth zones**

178 Next, we sought to investigate the localization dynamics of the bactofilin cytoskeleton *in vivo*. To this end,
179 we generated strains producing fluorescently tagged BacA or BacD derivatives in place of the native pro-
180 teins (**Figure 4—figure supplement 1**). Time-lapse microscopy analysis of cells producing a BacA-YFP
181 fusion on agarose pads (**Figure 4A**) revealed that the protein was localized to the new cell pole in swimmer
182 cells and remained associated with the stalk base during the initial phase of stalk formation. At some
183 point, it appeared to attach to the stalk structure and then move away from the base as new cell wall
184 material was inserted. Subsequently, stalk elongation ceased and the terminal stalk segment, delimited
185 by the bactofilin assembly, started to swell and develop into a bud, gradually displacing BacA-YFP in the
186 direction of the stalk base as its size increased. After cell division, both the mother cell and the newborn
187 swimmer cells showed a fluorescent focus, indicating that the bactofilin assembly was split during cell
188 division. To monitor the dynamics of the bactofilin cytoskeleton over multiple division cycles, we analyzed
189 the same strain in a flow-cell system (**Figure 4—figure supplement 2** and **Figure 4—videos 1-3**). Under
190 these conditions, the small, newborn swimmer cells were washed away immediately after cytokinesis,
191 preventing the formation of microcolonies around the mother cell. We observed that cell division
192 occurred at a small distance from the BacA-YFP focus, leaving a short stalk-terminal segment in between

193 the bactofilin assembly and the stalk tip. After cytokinesis, the stalk elongated again prior to the initiation
194 of the next budding event. Notably, BacA-YFP was only occasionally detected at the stalked pole during
195 the stalk restoration phase, suggesting that the bactofilin cytoskeleton no longer plays a major role in stalk
196 growth once the stalk structure has been established.

197 To verify the behavior observed in the time-lapse studies, we performed a population-wide analysis of the
198 BacA-YFP localization pattern, based on snap-shot images of exponentially growing cells. A demographic
199 analysis confirmed that the protein localizes to the new cell pole in swimmer cells, remains at the stalk
200 base in cells with short stalks and then moves to a position close to the distal end of the stalk before the
201 onset of budding, remaining associated with the bud neck up to the point of cell division (**Figure 4B**). A
202 very similar behavior was observed for a BacD variant fused to the yellow fluorescent protein Venus (Nagai
203 et al., 2002) (**Figure 4C**), consistent with the notion that the two bactofilin paralogs interact. In support of
204 this hypothesis, studies of a strain in which both proteins were fluorescently labeled showed that BacA
205 and BacD indeed co-localized to a large extent during all stages of the developmental cycle (**Figure 4D** and
206 **Figure 4—figure supplement 3**). However, at the onset of bud formation, the signals of the two proteins
207 were not always fully superimposable, with BacD assemblies occasionally detectable both at the bud neck
208 and in the mother cell (**Figure 4—figure supplement 4**). In the absence of BacA, BacD-Venus still formed
209 distinct foci, albeit at apparently random positions within the cell (**Figure 4—figure supplement 5**). Notab-
210 ly, a BacA-YFP variant carrying a previously reported mutation that disrupts the polymerization interface
211 (F130R) (Deng et al., 2019; Vasa et al., 2015; Zuckerman et al., 2015) was evenly distributed within the cell
212 and unable to functionally replace the wild-type protein, indicating that the formation of polymeric
213 assemblies is essential for proper BacA localization and function (**Figure 4—figure supplement 6**). Given
214 that the bactofilin assemblies are localized to the stalk and bud boundaries and required to prevent
215 unconstrained growth of these cellular structures, we hypothesized that the bactofilin cytoskeleton might
216 serve to limit the cell wall biosynthetic machinery to the different growth zones of *H. neptunium*.

217 To further investigate the role of bactofilin in the spatial regulation of cell wall biosynthesis, we generated
218 derivatives of the wild-type and Δ*bacAD* strains that produced a fluorescently (YFP-) labeled variant of
219 the membrane-bound elongasome protein RodZ, a core structural component of the complex connecting
220 the cytoplasmic MreB cytoskeleton to the periplasmic enzymatic machinery (Bendezú et al., 2009; van
221 den Ent et al., 2010; Alyahya et al., 2009). In the wild-type background, RodZ-YFP formed dynamic foci in
222 in the mother cell, at the (incipient) stalk base and the nascent bud (**Figure 5** and **Figure 5—videos 1,2**),
223 thus localizing to the different growth zones detected by HADA labeling (**Figure 2C**). These results are in

224 line with previous findings identifying the elongasome as a key determinant of cell growth in *H. neptunium*
225 (Cserti et al., 2017). Importantly, however, RodZ-YFP foci were never observed in the stalk, suggesting
226 that elongasome complexes are unable to cross the stalk base and the bud neck, even though their free
227 components appear to be able to diffuse through the stalk to facilitate the *de novo* assembly of elonga-
228 somes in the incipient bud compartment. In the Δ*bacAD* mutant, the localization behavior of RodZ-YFP
229 resembled that in the wild-type background as long as the cells were the early stages of the cell cycle,
230 with dynamic foci detectable throughout the cell envelope and at the (future) stalk base (**Figure 5** and
231 **Figure 5—video 3**). However, at later stages, the elongasome was no longer excluded from the nascent
232 stalk structure and, in many cases, even appeared to be enriched this region, leading to its remodeling
233 into an increasingly amorphous cellular extension (**Figure 5** and **Figure 3—videos 3-5**). The bactofilin cyto-
234 skeleton itself or the high degree of positive inner cell curvature induced in its presence at the stalk base
235 thus appear to act as a barrier that excludes elongasome complexes from the stalk and thus facilitates
236 proper morphogenesis and bud development.

237 **The assembly state of BacA changes at different stages of *H. neptunium* development**

238 Since bactofilins form highly stable polymers *in vitro* (Kühn et al., 2010; Zuckerman et al., 2015), the dyna-
239 mic localization observed for BacA and BacD was unexpected. To further characterize the dynamics of the
240 bactofilin cytoskeleton in *H. neptunium*, we followed the movement of individual BacA-YFP molecules in
241 swimmer, stalked and budding cells (**Figure 6—video 1**). First, we used single-molecule tracking data to
242 generate high-resolution images of the bactofilin assemblies in each of the three cell types. The results
243 confirmed the cell cycle-dependent localization patterns observed by widefield fluorescence microscopy
244 (**Figure 6A** and **Figure 6—figure supplement 1**). In addition, they revealed clusters in medial regions of
245 the stalk, which may represent transient polymers formed during the reshuffling of bactofilin molecules
246 between the stalk base and the (incipient) bud neck. When calculating the average mean squared dis-
247 placement of the tracked BacA-YFP molecules, we found that their mobility decreased gradually from the
248 swimmer over the stalked cell to the budding cell stage (**Figure 6B**). For each cell type, the distribution of
249 step sizes in the single-particle tracks suggests the existence of two distinct diffusion regimes, with a static
250 ($D= 0.02 \pm 0.0004\ \mu m^2\ s^{-1}$) and a mobile ($D= 0.35 \pm 0.004\ \mu m^2\ s^{-1}$) population, likely representing the poly-
251 merized and freely diffusible states, respectively (**Figure 6C** and **Figure 6—figure supplement 2**). In swim-
252 mer cells, the static fraction comprised only ~60% of the molecules. Its proportion increased to ~70% in
253 stalked cells and finally reached ~80% in budding cells. The F130R variant, by contrast, showed less than
254 15% of static molecules (**Figure 6B,C** and **Figure 6—figure supplement 2** and **Figure 6—video 1**) consistent
255 with the notion that it is impaired in polymerization but still able to assemble under certain conditions

256 after undergoing a structural change that generates an alternative polymerization interface (Deng et al.,
257 2019). Collectively, these results show that, in *H. neptunium*, the assembly state of the bactofilin cytoske-
258 leton changes as cells progress through their developmental cycle. Moreover, despite the inherent stabi-
259 lity of bactofilin polymers, all cell types display a sizeable fraction of mobile BacA-YFP molecules, which
260 could potentially reflect the dynamic reorganization of bactofilin assemblies during cell growth.

261 **Bactofilin genes are often clustered with genes encoding M23 peptidases**

262 After identifying a critical role of BacA in *H. neptunium* morphogenesis, we set out to gain further insight
263 into its mechanism of action. Notably, in several species in which bactofilins play a role in cell shape deter-
264 mination, the corresponding bactofilin genes are located adjacent to genes encoding a putative M23 pep-
265 tidase homologous to LmdC (**Figure 7A**). To determine whether this gene arrangement was more widely
266 conserved, we performed a comprehensive bioinformatic analysis in which we searched all bacterial
267 genome sequences available for putative bactofilin genes that were located immediately upstream or
268 downstream of open reading frames encoding proteins with a predicted M23 peptidase domain. This
269 analysis identified a total of 226 species from a wide variety of bacterial phyla (**Figure 7B** and **Figure 7—**
270 **Dataset 1**), suggesting a conserved functional association between bactofilins and M23 peptidases.

271 **The M23 peptidase LmdC of *H. neptunium* has peptidoglycan hydrolase activity *in vitro***

272 Like many of its homologs, *H. neptunium* LmdC is a predicted bitopic membrane protein with a short N-
273 terminal cytoplasmic region, a transmembrane helix, large periplasmic region composed of a predicted
274 coiled-coil domain, and a C-terminal M23 peptidase domain (**Figure 8A**). Members of the M23 peptidase
275 family usually have Zn^{+}-dependent hydrolase activity and cleave bonds within the peptide side chains of
276 in the peptidoglycan meshwork (Firczuk et al., 2005; Grabowska et al., 2015). However, there are also
277 various representatives that have lost their enzymatic activity because of mutations in residues required
278 for metal cofactor binding and have instead adopted regulatory roles in cell wall biosynthesis (Figueroa-
279 Cuilan et al., 2021; Goley et al., 2010; Gurnani Serrano et al., 2021; Möll et al., 2010; Poggio et al., 2010;
280 Uehara et al., 2010). An amino acid alignment showed that the M23 peptidase domain of LmdC features
281 all residues reported to be critical for Zn^{2+} binding, suggesting that it could act as a genuine peptidoglycan
282 hydrolase (**Figure 8B**). In a structural model of LmdC generated with AlphaFold2 (Jumper et al., 2021), the
283 periplasmic coiled-coil and M23 peptidase domains form an elongated, rigid unit with two flanking non-
284 structured regions that is flexibly linked to the transmembrane helix (**Figure 8C**). Notably, LmdC homologs
285 were shown to form a distinct clade among the M23 peptidases that is broadly conserved among species
286 but particularly enriched in alpha- and deltaproteobacteria (Figueroa-Cuilan et al., 2021).

287 To clarify whether LmdC was indeed catalytically active, we purified a C-terminal fragment of the protein
288 including the M23 peptidase domain and assayed its activity *in vitro*. Peptidoglycan from *H. neptunium*
289 shows only a low degree of cross-linkage and hardly any pentapeptides (Cserti et al., 2017), likely due to
290 a high level of autolytic activity. We therefore used normally crosslinked, pentapeptide-enriched peptido-
291 glycan from *E. coli* strain D456 (lacking PBPs 4, 5 and 6) (Edwards and Donachie, 1993) as a substrate to
292 enable a comprehensive analysis of the cleavage specificity of LmdC. Upon treatment with the protein,
293 the proportion of dimeric muropeptide species strongly decreased, regardless of the length of the cross-
294 linked peptides and without the formation of major additional monomer peaks (**Figure 8D**). The activity
295 of LmdC was particularly high at a pH value of 5, but the physiological significance of this effect remains
296 to be determined. Collectively, these results demonstrate that LmdC is a DD-endopeptidase cleaving the
297 bond between the meso-diaminopimelic acid residue of one peptide and D-alanine at position 4 of the
298 other peptide, thereby reducing the degree of cross-linkage within the peptidoglycan layer (**Figure 8E**).

299 **LmdC is critical for morphogenesis in *H. neptunium* and physically interacts with BacA**

300 To clarify whether LmdC was also required for proper growth in *H. neptunium*, we aimed to generate a
301 mutant strain lacking LmdC activity. However, all attempts to delete the *lmdC* gene or the entire putative
302 *lmdC-bacA* operon or to generate non-functional truncated *lmdC* alleles were unsuccessful, in line with a
303 previous report suggesting that *lmdC* is essential for viability (Cserti et al., 2017). It was also not possible
304 to generate a conditional *lmdC* mutant producing the gene under the control of a copper-inducible pro-
305 moter, suggesting that its expression level needs to be precisely regulated.

306 To address this issue, we developed a CRISPR interference (CRISPRi) system (Larson et al., 2013) that en-
307 abled the inducible down-regulation of target genes in *H. neptunium*. It is based on a newly constructed
308 integrative plasmid (pdCas9Entry) that carries the gene for a nuclease-deficient variant of *Streptococcus*
309 *pyogenes* Cas9 (dCas9) under the control of a copper-inducible promoter as well as a cassette for the
310 construction and constitutive expression of a gene-specific small guide RNA (sgRNA) (**Figure 9A** and **Figure**
311 **9—figure supplement 1A**). A derivative of this plasmid encoding an sgRNA directed against the 5' region
312 of the *lmdC* gene was then inserted into the *H. neptunium* chromosome (**Figure 9B**). Induction with copper
313 led to the formation of an sgRNA-dCas9 complex that targeted the non-coding strand of *lmdC*, generating
314 a road-block that prevented the movement of RNA polymerase and, thus, gene expression (**Figure 9C,D**).
315 Importantly, the block of *lmdC* expression led to cell shape defects very similar to those observed for the
316 Δ*bacA* mutant, as reflected by a large proportion of distorted and amorphous cells, which still showed
317 close-to-normal growth rates (**Figure 9E,F** and **Figure 9—figure supplement 1B,C**). Induced cells of a con-

318 trol strain carrying the empty pdCas9Entry plasmid did not show any obvious phenotype, indicating that
319 the presence of dCas9 alone did not have any adverse effects on cell growth or viability (**Figure 9D,E** and
320 **Figure 9—figure supplement 1C**). These results suggest that LmdC and BacA are part of the same morpho-
321 genetic pathway.

322 To further investigate whether the peptidoglycan hydrolase LmdC was functionally linked to bactofilins in
323 *H. neptunium*, we aimed to conduct *in vivo* co-localization studies. However, all attempts to generate
324 functional fluorescent protein fusion to full-length or C-terminally truncated LmdC failed, because the
325 fusion proteins were either unstable or did not produce any fluorescence signal *in vivo*. As a complemen-
326 tary approach, we analyzed the interaction between LmdC and BacA *in vitro* by biolayer interferometry.
327 To this end, a synthetic peptide comprising the predicted cytoplasmic region of LmdC (amino acids 1-38)
328 was immobilized on a biosensor and probed with increasing concentrations of purified BacA protein. The
329 results showed that BacA interacts with the LmdC peptide with an apparent equilibrium dissociation
330 constant (K_D) of ~15 µM. By contrast, an unrelated peptide used as a negative control was not bound with
331 appreciable affinity (**Figure 9G,H**). This result confirms a direct interaction between BacA and LmdC and
332 identifies the N-terminal cytoplasmic region of LmdC as the interaction determinant for BacA association.

333 ***R. rubrum* BacA recruits LmdC to the inner curve of the cell to modulate cell curvature**

334 Our bioinformatic analysis suggests that bactofilins and M23 peptidases may be functionally associated in
335 a large number of species. To further explore this possibility, we turned our efforts to the spiral-shaped
336 bacterium *Rhodospirillum rubrum*, which contains a putative *lmdC-bacA* operon similar to that in *H. nep-*
337 *tunium* (Munk et al., 2011) (**Figure 10A**). The *R. rubrum* BacA homolog Rru_A1867 ($BacA_{Rs}$) is 37% identical
338 (57% similar) to BacA of *H. neptunium* and also consists of a central Bactofilin A/B domain flanked by
339 terminal non-structured regions (**Figure 10B**). The LmdC homolog Rru_A1868 ($LmdC_{Rs}$) is 39% identical
340 (55% similar) to *H. neptunium* LmdC and has a similar predicted molecular structure (Varadi et al., 2022).
341 The deletion of $bacA_{Rs}$ led to a noticeable increase in cell curvature (**Figure 10C** and **Figure 10—figure**
342 **supplement 1A**), as also reflected in a significant increase in cell sinuosity (**Figure 10D**). A very similar
343 effect was observed for cells lacking $lmdC_{Rs}$ or both $bacA_{Rs}$ and $lmdC_{Rs}$, indicating that the two gene pro-
344 ducts act in the same pathway and jointly contribute to cell shape maintenance in *R. rubrum* (**Figure 10C,D**
345 **and Figure 10—figure supplement 1A**). In the two mutant strains, the global composition of peptido-
346 glycan was largely unchanged, supporting the notion that the $BacA_{Rs}$-$LmdC_{Rs}$ pathway modifies the cell
347 wall only locally or acts by modulating the activity of the standard cell elongation machinery (**Figure 10—**
348 **figure supplement 1B**).

349 Complementation studies showed that the expression of a plasmid-borne copy of *bacA* under the control
350 of a weak constitutive promoter attenuated the curvature defect, albeit only partially, likely due to inade-
351 quate expression levels (**Figure 10—figure supplement 2**). The generation of an analogous plasmid to
352 complement the deletion of $lmdC_{Rs}$ failed, because it was not possible to introduce the construct into
353 *Escherichia coli* for plasmid propagation, suggesting that the expression of $lmdC_{Rs}$ was toxic to the cells.
354 To further test this hypothesis, we constructed a plasmid enabling the expression of the gene under a
355 tightly controlled, inducible promoter in *E. coli*. Upon induction, a large part of the cell population lyzed,
356 whereas control cells carrying an empty plasmid did not show any phenotypic defects (**Figure 10—figure**
357 **supplement 3**). These results indicate that, similar to its *H. neptunium* homolog, $LmdC_{Rs}$ is an active en-
358 zyme with peptidoglycan hydrolase activity.

359 To further test the hypothesis that LmdC was functionally linked to bactofilin in *R. rubrum*, we set out to
360 perform *in vivo* co-localization studies. However, all attempts to generate fluorescently labeled variants
361 of full-length LmdC failed, because the corresponding *R. rubrum* expression plasmids appeared to be toxic
362 to *E. coli*. Importantly, our *in vitro* studies had shown that the interaction of LmdC with the bactofilin
363 cytoskeleton was mediated by its N-terminal cytoplasmic region (**Figure 9G,H**). To avoid the issues caused
364 by the full-length protein, we therefore generated a reporter fusion encoding only the predicted N-termi-
365 nal cytoplasmic region and the transmembrane helix (amino acids 1-80) of $LmdC_{Rs}$ fused to the green
366 fluorescent protein mNeonGreen (Shaner et al., 2012) ($LmdC^{N}_{Rs}$-mNG) (**Figure 10—figure supplement 4A-**
367 **C**). A low-copy plasmid carrying the corresponding allele under the control of the native $lmdC_{Rs}$ promoter
368 was then introduced into an *R. rubrum* $\Delta lmdC_{Rs}$ mutant producing a fully functional fusion of $BacA_{Rs}$ to the
369 red fluorescent protein mCherry ($BacA_{Rs}$-CHY) (Shaner et al., 2004) in place of the wild-type protein (**Fig-**
370 **ure 10—figure supplement 2**). We found that $BacA_{Rs}$-CHY and $LmdC^{N}_{Rs}$-mNG were consistently localized
371 to the same subcellular positions, forming patchy or filamentous structures that were preferentially, but
372 not exclusively, positioned at the inner curve of the cell (**Figure 10E**). A very similar behavior was observed
373 in the presence of wild-type $LmdC_{Rs}$ (**Figure 10—figure supplement 4D**). To further validate the enrich-
374 ment of the two fusion proteins at the inner curve, we quantified their fluorescence signals along the
375 inner and outer curves of multiple individual cells, concatenated the resulting fluorescence profiles and
376 ordered them according to their total length. In both cases, cells consistently displayed higher signal
377 intensities at the inner curve (**Figure 10F,G**), supporting the notion that $BacA_{Rs}$-$LmdC_{Rs}$ assemblies pro-
378 mote cell wall biosynthesis in the inner curve to reduce overall cell curvature. Notably, a $BacA_{Rs}$-mNG
379 fusion showed a reduced enrichment in the absence of $LmdC_{Rs}$, whereas $LmdC^{N}_{Rs}$-mNG completely lost its
380 asymmetric distribution in the $\Delta bacA_{Rs}$ background (**Figure 10H-J**). These results identify $BacA_{Rs}$ polymers

381 as recruitment platforms for LmdC$_{Rs}$, although an interaction between the two proteins appears to be
382 required for normal BacA$_{Rs}$ localization.

383 **LmdC recruitment depends on the conserved cytoplasmic β-hairpin motif**

384 The N-terminal cytoplasmic region of LmdC$_{Rs}$ contains a β-hairpin motif (**Figure 11A**) that is conserved
385 among LmdC homologs. To determine whether this structural feature was involved in BacA binding, we
386 exchanged two small clusters of amino acids that protruded from its surface and might thus serve as
387 interaction determinants, using LmdC$^{N}_{Rs}$-mNG as a reporter. Cluster I (R25, H26, L27) was located within
388 the first β-strand, whereas cluster II (R30, S31) was close to the β-turn (**Figure 11B**). The modifications in
389 cluster I completely abolished the enrichment of LmdC at the inner curve of the cell, indicating that the β-
390 hairpin motif is a critical part of the BacA binding site (**Figure 11C,D**). Notably, the loss of interaction
391 between the two proteins also led to a reduced inner-curve enrichment of BacA$_{Rs}$-CHY, as previously
392 observed in the Δ*lmdC*$_{Rs}$ background (**Figure 10I,J**). This observation confirms that LmdC$_{Rs}$ binding is re-
393 quired for BacA to adopt its proper spatial organization. Similar defects were caused by the modification
394 of cluster II (**Figure 11C,E**). However, in this case, BacA$_{Rs}$-CHY was also no longer enriched at the inner
395 curve, suggesting that the mutant protein may still show a residual, yet aberrant interaction with BacA$_{Rs}$
396 that has a negative effect on BacA$_{Rs}$ localization. Collectively, these findings confirm a functional associ-
397 ation between the bactofilin cytoskeleton and LmdC$_{Rs}$ in *R. rubrum*. Moreover, they support the notion
398 that bactofilins and LmdC-like M23 peptidases form a conserved morphogenetic module that is involved
399 in the establishment of complex bacterial cell shapes.

Discussion

400 Although bactofilins are widely conserved among bacteria, their cellular functions are still incompletely
401 understood. Here, we show that BacA homologs critically contribute to cell shape determination in two
402 morphologically distinct members of the alphaproteobacteria, the stalked budding bacterium *H. neptu-*
403 *nium* and the spiral-shaped bacterium *R. rubrum*. In both cases, they functionally interact with LmdC-type
404 DD-endopeptidases to promote local changes in the pattern of peptidoglycan biosynthesis. Bactofilins
405 thus complement the activities of the MreB and FtsZ cytoskeletons in the regulation of cell growth and
406 act as versatile cell shape modifiers that facilitate the establishment of complex bacterial morphologies.

407 In *H. neptunium*, the bactofilin cytoskeleton localizes dynamically to the stalk base and the bud neck, pro-
408 moting stalk growth and subsequent bud formation (**Figure 4**). While flanked by zones of active growth,
409 the stalk itself is usually devoid of cell wall biosynthetic machinery (Cserti et al., 2017) (**Figure 5**). In bacto-
410 filin-deficient cells, however, the stalk and bud growth zones are no longer confined and expand into the
411 stalk envelope, leading to stalk widening and the formation of irregular bulges due to uncontrolled pep-
412 tidoglycan incorporation and bud expansion (**Figure 2** and **Figure 5**). Bulges or larger amorphous segments
413 at some point separate from the mother cell and then continue to grow as independent cells, indicating
414 that chromosome replication and segregation as well as cell division still occur under these conditions.
415 Together, these observations suggests that bactofilin polymers establish barriers that normally prevent
416 the entry of elongasome complexes from the mother cell or nascent bud compartments into the stalk.

417 The precise mechanism underlying the function of bactofilin in cell morphogenesis remains to be clarified.
418 It is conceivable that bactofilin polymers act by tethering peptidoglycan biosynthetic proteins or estab-
419 lishing physical barriers that hinder the mobility of elongasome complexes (**Figure 12A**). However, we
420 observed a close functional association of bactofilins with M23 peptidases that appears to be widely con-
421 served among species, suggesting that their activity may be intimately tied to cell wall hydrolysis. The
422 transition zones between the stalk and the adjacent mother cell and bud compartments are characterized
423 by a high degree of positive inner cell curvature, which is in stark contrast to the negative curvature in the
424 remaining parts of the cell. The hydrolytic activity of *H. neptunium* LmdC may be critical to remodel the
425 cell wall in these zones and thus facilitate the extrusion of the stalk. Importantly, MreB is thought to move
426 along regions of negative inner cell curvature (Hussain et al., 2018; Wong et al., 2019). The positively
427 curved transition zones generated by the bactofilin-LmdC assemblies could therefore represent topo-
428 logical barriers that are difficult to cross by elongasome complexes, thereby helping to restrict their move-
429 ment to the mother cell and bud compartments. Moreover, the narrow diameter stalks and their exceed-

430 ingly high degree of negative inner cell curvature may reduce the stability of elongasome complexes that
431 may form spontaneously in the stalk region. These effects may also be important during the stalk elonga-
432 tion phase following cell division, when bactofilin assemblies are no longer present at the stalk base.

433 Notably, a role in stalk formation has also been reported for the bactofilin homologs of *C. crescentus* and
434 *A. biprosthecum*. In *C. crescentus*, the major bactofilin BacA was shown to act as a localization determinant
435 for the bifunctional penicillin-binding protein PbpC, a cell wall synthase that contributes to stalk elonga-
436 tion (Kühn et al., 2010) and the proper sorting of a stalk-specific protein (Hughes et al., 2013). However,
437 the absence of BacA only leads to a moderate reduction in stalk length and leaves overall cell shape
438 unaffected, indicating that this protein has only a minor role in *C. crescentus* stalk formation. In *A. bipros-*
439 *thecum*, by contrast, the deletion of *bacA* completely abolishes stalk formation in rich medium and leads
440 to the formation of wide cellular protrusions, named pseudostalks, under phosphate-limiting conditions
441 (Caccamo et al., 2020). Similar to the amorphous extensions observed for the *H. neptunium* Δ*bacAD* mu-
442 tant, these structures grow through disperse incorporation of new peptidoglycan and develop into viable
443 offspring. Their formation was also attributed to the entry of cell wall biosynthetic proteins into nascent
444 stalks (Caccamo et al., 2020), suggesting that the *H. neptunium* and *A. biprosthecum* BacA homologs share
445 the same barrier function during stalk formation. However, in *H. neptunium*, another layer of regulation
446 has been added in which bactofilins establish a second barrier close to the stalk tip that enables the for-
447 mation of stalk-terminal buds. Bud expansion requires the relocation of elongasome complexes from the
448 mother cell to the nascent bud at the onset of bud formation, as likely reflected by the fact that compo-
449 nents of the elongasome (MreB, RodZ) and new cell wall biosynthesis can be detected within the stalk
450 during a short time window at the end of the stalk elongation phase (Cserti et al., 2017). This process may
451 be facilitated by the (partial) disassembly of the bactofilin complex at the stalk base and the diffusion of
452 its components to the bud compartment, but the mechanistic details remain to be investigated. Another
453 open question concerns the factors that control the dynamic localization of bactofilin to the stalked pole
454 and the future bud neck in the terminal segment of the stalk. In *A. biprosthecum*, the recruitment of BacA
455 assemblies to the sites of stalk biosynthesis is dependent on the cell wall hydrolase SpmX (Caccamo et al.,
456 2020). However, an *H. neptunium* mutant lacking this protein shows normal morphology (Leicht et al.,
457 2020), suggesting the existence of a different localization determinant.

458 Intriguingly, bactofilins not only mediate stalk formation and stalk-terminal budding but also the forma-
459 tion of curved cell shapes. We show that both BacA and LmdC are required to establish the normal degree
460 of cell helicity in *R. rubrum*, with their absence leading to hyper-curved cells (**Figure 10C,D**). This result

461 suggests that the two proteins form an accessory module that counteracts the activity of a so-far unknown
462 system responsible for generating spiral cell shape in *R. rubrum* (**Figure 12B**). Cell curvature was shown to
463 promote cell motility (Martinez et al., 2016). It is tempting to speculate that the expression of *bacA* and
464 *lmdC* could be controlled in response to external cues to ensure optimal cell helicity and, thus, fitness in
465 different environments. Our results show that *R. rubrum* cells contain multiple BacA-LmdC complexes that
466 are distributed along the entire cell envelope but localize preferentially to the inner cell curvature (**Figure**
467 **10E,G**). In this system, it is immediately obvious that BacA acts as a localization determinant for LmdC,
468 since the preferential localization of LmdC to the inner curve is abolished in its absence (**Figure 10I,J**). To
469 reduce cell curvature, the hydrolytic activity of LmdC must ultimately stimulate the insertion of new pep-
470 tidoglycan at the inner curve of the cell, which increases the rate of cell elongation in this region and thus
471 straightens the cell body. A similar mechanism may also be at work in the spirochete *L. biflexa*, where the
472 loss of the bactofilin paralog LbbD, whose gene lies adjacent to a gene for putative M23 peptidase
473 (LEPBI_I1430) (**Figure 7A**), was found to induce a strong increase in cell helicity (Jackson et al., 2018). A
474 different variation of this theme is found in *H. pylori*. There, the bactofilin homolog CcmA also forms
475 multiple assemblies along the cell envelope, which interact with a membrane-spanning protein complex
476 including an M23 peptidase (Csd1) homologous to LmdC (Sichel et al., 2022; Taylor et al., 2020). However,
477 these assemblies are enriched at the outer curve of the cell, where they stimulate peptidoglycan synthesis
478 to locally increase the rate of cell elongation over that at the inner curve, leading to twisting of the cell
479 body.

480 Notably, in all systems characterized so far in molecular detail, the function of bactofilin-M23 peptidase
481 complexes involves the stimulation of cell wall biosynthesis in a confined region of the cell envelope that
482 entails a local change in cell envelope curvature. In *H. neptunium*, these complexes are only localized to
483 narrow bands at the stalk base and bud neck, generating sharp bends at the transition zones between the
484 stalk and the adjacent mother cell and bud compartments. In spiral-shaped bacteria, by contrast, they are
485 scattered along the entire length of the cell, thereby establishing an elongated zone of increased longi-
486 tudinal growth that changes overall cell curvature. The same mechanistic principle may also explain the
487 morphogenetic role of bactofilins in so-far uninvestigated systems.

488 Collectively, our results underscore the role of bactofilins as versatile modulators of bacterial cell shape.
489 In association with M23 peptidases, they form cell wall biosynthetic complexes that introduce local
490 changes in cell envelope curvature. In doing so, they complement the activities of the tubulin and actin
491 cytoskeletons in cell shape determination and thus expand the morphogenetic potential of bacteria,

492 enabling the generation of complex cell shapes that go beyond the generic rod-like or spherical morpho-
493 logies. It will be interesting to investigate the molecular function of bactofilins in a range of morphologic-
494 ally diverse species to obtain a comprehensive picture of the functionalities provided by these cytoskeletal
495 proteins and the conservation of their mode of action.

Materials and methods

496 **Media and growth conditions**

497 *H. neptunium* LE670 (ATCC 15444) (Leifson, 1964) and its derivatives were grown in Artificial Sea Salt (ASS)
498 medium at 28 °C under aerobic conditions, shaking at 210 rpm in baffled flasks. ASS medium was
499 composed of 0.5% Bacto Peptone (Thermo Fisher Scientific, USA), 0.1% yeast extract, 1 mM $MgSO_4$,
500 0.5 mM $CaCl_2$ and 1.5% Instant Ocean Sea Salt (Spectrum Brands, USA), dissolved in deionized water. For
501 solid media, 1.5% agar was added prior to autoclaving. When appropriate, antibiotics were used at the
502 following concentrations (µg/mL in liquid/solid medium): rifampicin (1/2), kanamycin (100/200). The ex-
503 pression of genes under the control of the copper-inducible P_{Cu} promoter or the zinc-inducible P_{Zn}
504 promoter (Jung et al., 2015) was induced by the addition of $CuSO_4$ or $ZnSO_4$ to the concentrations
505 indicated in the text. To assess the growth of *H. neptunium*, cells were grown to exponential phase, diluted
506 in fresh medium to an optical density at 580 nm (OD_{580}) of 0.02, and transferred into 24-well polystyrene
507 microtiter plates (Becton Dickinson Labware, USA). Growth was then followed at 32 °C under double-
508 orbital shaking in an EPOCH 2 microplate reader (BioTek, USA) by measuring the OD_{580} at 20-min intervals.

509 *R. rubrum* S1 (ATCC 11170) (Molisch, 1907; Pfennig and Trüper, 1971; van Niel, 1944) and its derivatives
510 were grown in Bacto Tryptic Soy Broth (BD Diagnostic Systems, USA) at 28 °C under aerobic conditions,
511 shaking at 210 rpm in Erlenmeyer flasks. When appropriate, media were supplemented with antibiotics
512 at the following concentrations (µg/mL in liquid/solid medium): kanamycin (30/30), cefalexin (15/-).

513 *E. coli* strains were cultivated aerobically (shaking at 210 rpm) at 37 °C in LB medium. For plasmid-bearing
514 strains, antibiotics were added at the following concentrations (µg/mL in liquid/solid medium): kanamycin
515 (30/50), rifampicin (25/50), ampicillin (50/200). To grow *E. coli* WM3064, media were supplemented with
516 2,6-diaminopimelic acid (DAP) to a final concentration of 300 µM.

517 **Determination of growth rates**

518 Exponentially growing cultures were diluted to an OD_{580} of ~0.01, transferred to a 96-well plate and incu-
519 bated at 30°C with double-orbital shaking at 355 cpm in an Epoch 2 microplate reader (BioTek, Germany).
520 Growth was monitored by measuring the OD_{600} at 10-min intervals until the stationary phase was reached.
521 OD_{600} measurements obtained in the exponential phase were used to calculate the growth rate μ (increase
522 in OD_{600} per hour). The doubling time t_d was then calculated using the equation $t_d = \ln(2)/\mu$.

523 **Plasmid and strain construction**

524 The bacterial strains, plasmids, and oligonucleotides used in this study are listed in **Supplementary file 1**.
525 *E. coli* TOP10 (Thermo Fisher Scientific, USA) was used as host for cloning purposes. All plasmids were
526 verified by DNA sequencing. *H. neptunium* and *R. rubrum* were transformed by conjugation using the DAP-
527 auxotrophic strain *E. coli* WM3064 as a donor (Jung et al., 2015). The integration of non-replicating plas-
528 mids at the chromosomal P_{Cu} or P_{Zn} locus of *H. neptunium* was achieved by single homologous recombi-
529 nation (Jung et al., 2015). Gene replacement in *H. neptunium* and *R. rubrum* was achieved by double-
530 homologous recombination using the counter-selectable *sacB* marker (Cserti et al., 2017). Proper chromo-
531 somal integration or gene replacement was verified by colony PCR.

532 **Live-cell imaging**

533 Cells of *H. neptunium* and *R. rubrum* were grown to exponential phase in the appropriate medium and, if
534 suitable, induced with $CuSO_4$ prior to imaging. For depletion experiments, cells were grown in the pres-
535 ence of inducer, washed three times with inducer-free medium and then further cultivated in the absence
536 of inducer for the indicated period of time prior to analysis. To acquire still images, cells were transferred
537 onto 1% agarose pads (in water). For time-lapse analysis, cells were immobilized on pads made of 1%
538 agarose in ASS medium, and the cover slides were then sealed with VLAP (1:1:1 mixture of vaseline,
539 lanolin, and paraffin) to prevent dehydration. Imaging was performed using a Zeiss Axio Imager.M1
540 microscope equipped with a Zeiss alpha Plan-Apochromat 100x/1.40 Oil DIC objective and a pco.edge 3.1
541 sCMOS camera (PCO, Germany) or a Zeiss Axio Imager.Z1 microscope equipped with a Zeiss alpha Plan-
542 Apochromat 100x/1.46 Oil DIC M27 or a Plan-Apochromat 100x/1.40 Oil Ph3 M27 objective and a
543 pco.edge 4.2 sCMOS camera (PCO, Germany). An X-Cite 120PC metal halide light source (EXFO, Canada)
544 and ET-DAPI, ET-YFP or ET-TexasRed filter cubes (Chroma, USA) were used for fluorescence detection.
545 Microfluidic experiments were performed using a CellASIC ONIX EV262 Microfluidic System, equipped
546 with an F84 manifold and B04A microfluidic plates (Merck Millipore, Germany), which were flushed with
547 PBS buffer for 30 min before usage. Exponentially growing cells were flushed into the flow cells, cultivated
548 under continuous medium flow (0.4 ml/h), and imaged at regular intervals using the Axio Image.Z1 micros-
549 cope described above. To visualize sites of ongoing peptidoglycan synthesis, cells were grown to the
550 exponential phase, incubated for 1 min with 1 mM HADA and washed four times in ASS medium prior to
551 imaging.

552 Images were recorded with VisiView 3.3.0.6 (Visitron Systems, Germany) and processed with ImageJ
553 (Schneider et al., 2012) and Adobe Illustrator CS6 (Adobe Systems, USA). The subcellular distribution of

554 fluorescence signals was analyzed with BacStalk (Hartmann et al., 2020). Pearson's correlation coefficients
555 were determined using the JACoP plug-in (Bolte and Cordelieres, 2006) for ImageJ. Cell sinuosity was
556 determined using the ImageJ plug-in MicrobeJ (Ducret et al., 2016), with each analysis performed in
557 triplicate and 100 cells analyzed per strain and experiment. Results were displayed as SuperPlots (Lord et
558 al., 2020) generated using the SuperPlotsOfData web application (Goedhart, 2021).

559 To analyze the distribution of fluorescently tagged BacA and LmdC variants along the outline of *R. rubrum*
560 cells, the fluorescence intensity along the outer and inner curve was determined for 200 cells per strain
561 using Fiji (Schindelin et al., 2012). After concatenation of the two fluorescence profiles obtained for each
562 cell, the combined profiles were plotted as demographs, using R 4.2.3 (R Development Core Team, 2012)
563 and the Cell-Profiles package (github.com/ta-cameron/Cell-Profiles/wiki/Vignette) (Cameron et al., 2014).

564 **Single-particle tracking and diffusion analysis**

565 Cells were cultivated overnight in ASS medium, transferred into fresh medium and grown to exponential
566 phase prior to imaging by slimfield microscopy (Plank et al., 2009). In this approach, the back aperture of
567 the objective is underfilled by illumination with a collimated laser beam of reduced width, generating an
568 area of ~10 µm in diameter with a light intensity high enough to enable the visualization of single
569 fluorescent protein molecules at very high acquisition rates. The single-molecule level was reached by
570 bleaching of most molecules in the cell for 100 to 1,000 frames, followed by tracking of the remaining and
571 newly synthesized molecules for ~3,000 frames. Images were taken at 30 ms intervals using an Olympus
572 IX-71 microscope equipped with a UAPON 100x/ NA 1.49 TIRF objective, a back-illuminated electron-
573 multiplying charge-coupled device (EMCCD) iXon Ultra camera (Andor Solis, USA) in stream acquisition
574 mode, and a LuxX 457-100 (457 nm, 100 mW) light-emitting diode laser (Omicron-Laserage Laserprodukte
575 GmbH, Germany) as an excitation light source. The laser beam was focused onto the back focal plane and
576 operated during image acquisition with up to 2 mW (60 W/cm^2 at the image plane). Andor Solis 4.21
577 software was used for camera control and stream acquisition. Prior to analysis, frames recorded before
578 reaching the single-molecule level were removed from the streams, using photobleaching curves as a
579 reference. Subsequently, the streams were cropped to an equal length of 2,000 frames and the proper
580 pixel size (100 nm) and time increment were set in the imaging metadata using Fiji (Schindelin et al., 2012).
581 Single particles were tracked with u-track 2.2 (Jaqaman et al., 2008). Trajectories were only considered
582 for further statistical analysis if they had a length of at least five steps. Data analysis was performed using
583 SMTracker 2.0 (Oviedo-Bocanegra et al., 2021). An estimate of the diffusion coefficient and insight into
584 the kind of diffusive motion exhibited were obtained from mean-squared-displacement (MSD)-versus-

585 time-lag curves. In addition, the frame-to-frame displacements of all molecules in x and the y direction
586 were fitted to a two-population Gaussian mixture model to determine the proportions of mobile and static
587 molecules in each condition (Oviedo-Bocanegra et al., 2021).

588 **Transmission electron microscopy**

589 Images of *H. neptunium* cells, 10 µl of early exponential cell cultures were applied onto glow-discharged
590 electron microscopy grids (Formvar/Carbon Film on 300 Mesh Copper; Plano GmbH, Germany) and
591 incubated for 1 min at room temperature. The grid was manually blotted with Whatman filter paper to
592 remove excess liquid. Subsequently, the cells were negatively stained for 5 sec with 5 µl of 1% uranyl
593 acetate. After three washes with H_2O, the grids were dried and imaged in a 100 kV JEM-1400 Plus trans-
594 mission electron microscope (JEOL, USA). To image BacA polymers, purified BacA-His_6 was dialyzed against
595 low-salt buffer (50 mM HEPES pH 7.2, 10 mM NaCl, 5 mM $MgCl_2$, 0.1 mM EDTA, 1 mM ß-mercaptoethanol)
596 for 16 h. The protein was spotted onto carbon-coated grids and allowed to settle for 2 min. The grids were
597 blotted dry, stained with 1:2 diluted supernatant of saturated 2 % uranyl acetate (in H_2O) for 1 min, dried
598 and imaged using a Zeiss CEM902 electron microscope, operated at 80 kV and equipped with a 2048x2048
599 pixel CCD camera. Image processing was carried out using Photoshop CS2 and Illustrator CS5 (Adobe
600 Systems, USA).

601 **Immunoblot analysis**

602 Antibodies against BacA were raised by immunization of rabbits with purified BacA-His_6 protein
603 (Eurogentec, Belgium). Cells were harvested in the exponential growth phase. Immunoblot analysis was
604 conducted as described previously (Thanbichler and Shapiro, 2006), using anti-BacA antiserum (1:10.000),
605 a monoclonal anti-mNeonGreen antibody (Chromotek, Germany; Cat. #: 32f6; RRID: AB_2827566), a
606 polyclonal anti-GFP antibody (Sigma, Germany; Cat. #: G1544; RRID: AB_439690), a polyclonal anti-
607 mCherry antibody (BioVision, USA; Cat. #: 5993; RRID: AB_1975001) or a monoclonal anti-HA antibody
608 (Merck Millipore, USA; Cat. #: 05-904; RRID: AB_11213751) at dilutions of 1:10,000, 1:1,000, 1:10,000,
609 1:10,000 or 1:1,000, respectively. Goat anti-rabbit immunoglobulin G conjugated with horse-radish per-
610 oxidase (Perkin Elmer, USA) or goat anti-mouse immunoglobulin G conjugated with horse-radish per-
611 oxidase (Sigma, Germany) were used as secondary antibodies. Immunocomplexes were detected with the
612 Western Lightning Plus-ECL chemiluminescence reagent (Perkin Elmer, USA). The signals were recorded
613 with a ChemiDoc MP imaging system (BioRad, Germany) and analyzed using Image Lab software (BioRad,
614 Germany).

615 **Peptidoglycan analysis**

616 Cultures of exponentially growing cells of the *H. neptunium* wild type and its mutant derivatives EC28
617 (Δ*bacA*), EC23 (Δ*bacD*) and EC33 (Δ*bacAD*) were rapidly cooled to 4°C and harvested by centrifugation at
618 16,000 ×g for 30 min. The cells were resuspended in 6 ml of ice-cold H_2O and added dropwise to 6 ml of a
619 boiling solution of 8% sodium dodecylsulfate (SDS) that was stirred vigorously. After 30 min of boiling, the
620 suspension was cooled to room temperature. Peptidoglycan was isolated from the cell lysates as
621 described previously (Glauner, 1988) and digested with the muramidase cellosyl (kindly provided by
622 Hoechst, Frankfurt, Germany). The resulting muropeptides were reduced with sodium borohydride and
623 separated by HPLC following an established protocol (Bui et al., 2009; Glauner, 1988). The identity of
624 eluted fragments was assigned based on the known retention times of muropeptides, as reported
625 previously (Cserti et al., 2017; Glauner, 1988).

626 **Protein purification**

627 To purify BacA-His_6, *E. coli* Rosetta(DE3)pLysS (Invitrogen) was transformed with pEC86 and grown in LB
628 medium at 37 °C to an OD_{600} of 0.8. Isopropyl-β-D-1-thiogalactopyranoside (IPTG) was added to a final
629 concentration of 0.5 mM and the incubation was continued for another 3 h. The cells were harvested by
630 centrifugation for 15 min at 7,500 ×g and 4 °C and washed with buffer B2 (50 mM NaH_2PO_4, 300 mM NaCl,
631 10 mM imidazole, adjusted to pH 8.0 with NaOH). Subsequently, they were resuspended in buffer B2
632 containing 100 µg/mL phenylmethylsulfonyl fluoride, 10 µg/mL DNase I and 1 mM β-mercaptoethanol
633 and lysed by three passages through a French press at 16,000 psi. After the removal of cell debris by
634 centrifugation at 30,000 ×g for 30 min, the supernatant was applied onto a 5 mL HisTrap HP column (GE
635 Healthcare) equilibrated with buffer B3 (50 mM NaH_2PO_4, 300 mM NaCl, 20 mM imidazole, adjusted to
636 pH 8.0 with NaOH). The column was washed with 10 column volumes (CV) of the same buffer, and protein
637 was eluted at a flow rate of 1 mL/min with a linear imidazole gradient obtained by mixing buffers B3 and
638 B4 (50 mM NaH_2PO_4, 300 mM NaCl, 250 mM imidazole, adjusted to pH 8.0 with NaOH). Fractions
639 containing high concentrations of BacA-His_6 were pooled and dialyzed against 3 L of buffer B5 (20 mM
640 Tris/HCl pH 8.0, 10 mM NaCl, 1 mM β-mercaptoethanol) at 4 °C. After the removal of precipitates by
641 centrifugation at 30,000 ×g for 30 min, the protein solution was aliquoted and snap-frozen in liquid nitro-
642 gen. Aliquots were stored at -80 °C until further use.

643 To purify LmdC, the protein was first produced as a His_6-SUMO-LmdC fusion (Marblestone et al., 2006).
644 To this end, *E. coli* Rosetta(DE3)pLysS cells carrying plasmid pLY015 were grown at 37 °C in 3 L of LB
645 medium supplemented with ampicillin and chloramphenicol. At an OD_{600} of 0.6, the culture was chilled to

646 18°C, and protein synthesis was induced by the addition of 1 mM IPTG prior to overnight incubation at 18
647 °C. The cultures were harvested by centrifugation at 10,000 ×g for 20 min at 4 °C and washed with lysis
648 buffer (50 mM Tris/HCl pH 8.0, 300 mM NaCl). Cells were resuspended in lysis buffer supplemented with
649 5 mM imidazole, 10 mg/mL DNase I and 100 mg/mL PMSF. After three passages through a French press
650 (16,000 psi), the cell lysate was clarified by centrifugation (30,000 ×g, 30 min, 4 °C). Protein was then
651 purified using zinc-affinity chromatography using a 1 mL Zn-NTA column (Cube Biotech) equilibrated with
652 lysis buffer containing 5 mM imidazole. Protein was eluted with a linear gradient of 5 to 250 mM imidazole
653 in lysis buffer at a flow rate of 1 mL/min. Fractions containing high concentrations of His_6-SUMO-LmdC
654 were pooled and dialyzed against 3 L of low-salt lysis buffer (20 mM Tris/HCl pH 7.6, 50 mM NaCl, 10%
655 (v/v) glycerol). After the addition of Ulp1 protease (Marblestone et al., 2006) and dithiothreitol (1 mM),
656 the protein was incubated for 4 h at 4 °C to cleave off the His_6-SUMO tag. The solution was centrifuged
657 for 30 min at 38,000 ×g and 4 °C to remove precipitates and then subjected to ion exchange chromato-
658 graphy using a 1 mL HiTrap Q HP column (Cytiva, USA) equilibrated with low-salt lysis buffer. His_6-SUMO
659 passed the column in the flow-through, and LmdC was eluted with a linear gradient of 150-1000 mM NaCl
660 in low-salt buffer. Fractions containing LmdC were concentrated in an Amicon Ultra-4 10K spin concen-
661 trator (MWCO 10,000; Merck, Germany). After the removal of precipitates by centrifugation at 30,000 ×g
662 for 30 min, LmdC was further purified by size exclusion chromatography (SEC) on a HighLoad 16/60
663 Superdex 200 pg column (GE Healthcare, USA) equilibrated with SEC buffer (20 mM Tris/HCl pH 7.4, 150
664 mM NaCl). Fractions containing pure protein were pooled and concentrated. After the removal of
665 precipitates by centrifugation at 30,000 ×g, the protein solution was snap-frozen in liquid N_2 and stored
666 at -80 °C until further use.

667 **LmdC enzymatic activity assay**

668 To test the enzymatic activity of LmdC, peptidoglycan from *E. coli* D456 (Edwards and Donachie, 1993)
669 was mixed with 10 µM LmdC in buffer A (20 mM Hepes/NaOH pH 7.5, 50 mM NaCl, 1 mM $ZnCl_2$) or buffer
670 B (20 mM sodium acetate pH 5.0, 50 mM NaCl, 1 mM $ZnCl_2$) in a final volume of 50 µL and incubated at
671 37°C for 16 h in a thermal shaker set at 900 rpm. A mixture of peptidoglycan in buffer B without LmdC was
672 used as a control. The reactions were stopped by heating at 100°C for 10 min. The peptidoglycan was then
673 further digested overnight with cellosyl, and the reactions were stopped by heating at 100°C for 10 min.
674 After centrifugation of the samples at 14,000 rpm for 10 min, the supernatants were recovered, reduced
675 with sodium borohydride, acidified to pH 4.0 – pH 4.5 with dilute 20% phosphoric acid and subjected to
676 HPLC analysis as previously described (Glauner, 1988).

677 **Bio-layer interferometry**

678 Bio-layer interferometry analyses were conducted using a BLItz system equipped with High Precision
679 Streptavidin (SAX) Biosensors (Sartorius, Germany). As a ligand, a custom-synthetized N-terminally biotin-
680 ylated peptide comprising residues Met1 to Gln38 of LmdC (GenScript, USA) was immobilized on the
681 biosensors. After the establishment of a stable baseline, association reactions were monitored at various
682 analyte concentrations. At the end of each binding step, the sensor was transferred into an analyte-free
683 buffer to follow the dissociation kinetics. The extent of non-specific binding was assessed by monitoring
684 the interaction of analyte with unmodified sensors. All analyses were performed in BLItz binding buffer
685 (25 mM HEPES/KOH pH 7.6, 100 mM KCl, 10 mM $MgSO_4$, 1 mM DTT, 10 mM BSA, 0.01% Tween).

686 **Bioinformatic analysis**

687 Protein similarity searches were performed with BLAST (Altschul et al., 1990), using the BLAST server of
688 the National Institutes of Health (https://blast.ncbi.nlm.nih.gov/Blast.cgi). Transmembrane helices were
689 predicted with DeepTMHMM (Hallgren et al., 2022), coiled-coil regions with PCOILS (Lupas, 1996). The
690 positions of conserved functional domains were determined using the PFAM server (Mistry et al., 2021).
691 AlphaFold2 (Jumper et al., 2021) and AlphaFold-Multimer (Evans et al., 2022), as implemented in the
692 AlphaFold.ipynb notebook on Google Colab, were used to predict the tertiary or quaternary structure of
693 proteins, respectively. SuperPlots (Lord et al., 2020) were used to visualize cell length distributions and to
694 evaluate the statistical significance of differences between multiple distributions, employing the
695 PlotsOfData web app (Postma and Goedhart, 2019).

Acknowledgements

We thank Julia Rosum for excellent technical assistance, Svenja Urban and Ying Liu for help with the construction of plasmids, Daniela Vollmer for the purification of peptidoglycan, and Maria Perez-Burgos and Lotte Søgaard-Andersen for help with the transmission electron microscopy analyses.

Additional information

Funding

Funder	Grant reference number	Author
University of Marburg	Core funding	Peter L. Graumann Martin Thanbichler
Max Planck Society	Max Planck Fellowship	Martin Thanbichler
German Research Foundation (DFG)	450420164	Martin Thanbichler
German Research Foundation (DFG)	26942323 – TRR 174	Peter L. Graumann
United Kingdom Biotechnology and Biological Sciences Research Council	BB/W013630/1	Waldemar Vollmer
Max Planck Society	PhD fellowship of the International Max Planck Research School for Environmental, Cellular and Molecular Microbiology (IMPRS-Mic)	Manuel Osorio-Valeriano
The funders had no role in the design of the study, the collection and interpretation of the data, or the decision to submit the work for publication.		

Author contributions

S.P., M.O.V., E.C. and M.T. conceived the study. S.P., M.O.V., E.C. and J.H. constructed plasmids and strains and performed the growth analyses and subcellular localization studies. M.O.V. purified proteins and conducted the biochemical studies. J.H. established the CRISPRi system for *H. neptunium*. R.H.-T. performed the single-particle tracking analysis. J.B. conducted the peptidoglycan analysis. P.S. analyzed the co-conservation of BacA and LmdC homologs. S.P., M.O.V., E.C., R.H.-T., P.S., J.B., W.V. and M.T. analyzed the data. W.V., P.L.G. and M.T. supervised the study. W.V., P.L.G. and M.T. secured funding. S.P., M.O.V. and M.T. wrote the paper, with input from all other authors.

Data availability

All relevant data generated in this study are included in the manuscript and the supplemental information.

Competing interests

The authors declare no competing interests.

References

705 Aaron M, Charbon G, Lam H, Schwarz H, Vollmer W, Jacobs-Wagner C. 2007. The tubulin homologue FtsZ
706 contributes to cell elongation by guiding cell wall precursor synthesis in *Caulobacter crescentus*.
707 *Molecular Microbiology* **64**:938-952.

708 Altschul SF, Gish W, Miller W, Myers EW, Lipman DJ. 1990. Basic local alignment search tool. *Journal of*
709 *Molecular Biology* **215**:403-410.

710 Alyahya, SA, Alexander R, Costa T, Henriques Ao, Emonet T, Jacobs-Wagner C. 2009. RodZ, a component
711 of the bacterial core morphogenetic apparatus. *Proceedings of the National Academy of Sciences U S*
712 *A* **106**: 1239-1244.

713 Badger JH, Hoover TR, Brun YV, Weiner RM, Laub MT, Alexandre G, Mrazek J, Ren Q, Paulsen IT, Nelson
714 KE *et al.* 2006. Comparative genomic evidence for a close relationship between the dimorphic
715 prosthecate bacteria *Hyphomonas neptunium* and *Caulobacter crescentus*. *Journal of Bacteriology*
716 **188**:6841-6850.

717 Bendezú FO, Hale CA, Bernhardt TG, de Boer PAJ. 2009. RodZ (YfgA) is required for proper assembly of the
718 MreB actin cytoskeleton and cell shape in *E. coli*. *EMBO Journal* **28**: 193-204.

719 Bolte S, Cordelieres FP. 2006. A guided tour into subcellular colocalization analysis in light microscopy.
720 *Journal of Microscopy* **224**:213-232.

721 Brown PJ, Kysela DT, Brun YV. 2011. Polarity and the diversity of growth mechanisms in bacteria. *Seminars*
722 *in Cell & Developmental Biology* **22**:790-798.

723 Bui NK, Gray J, Schwarz H, Schumann P, Blanot D, Vollmer W. 2009. The peptidoglycan sacculus of
724 *Myxococcus xanthus* has unusual structural features and is degraded during glycerol-induced
725 myxospore development. *Journal of Bacteriology* **191**:494-505.

726 Caccamo PD, Jacq M, VanNieuwenhze MS, Brun YV. 2020. A division of labor in the recruitment and
727 topological organization of a bacterial morphogenic complex. *Current Biology* **30**:3908-3922.

728 Cameron TA, Anderson-Furgeson J, Zupan JR, Zik JJ, Zambryski PC. 2014. Peptidoglycan synthesis
729 machinery in *Agrobacterium tumefaciens* during unipolar growth and cell division. *MBio* **5**:e01219–14.

730 Chen B, Gilbert LA, Cimini BA, Schnitzbauer J, Zhang W, Li G-W, Park J, Blackburn EH, Weissman JS, Qi LS,
731 Huang B. 2013. *Cell* 155: 1479-1491.

732 Cserti E, Rosskopf S, Chang YW, Eisheuer S, Selter L, Shi J, Regh C, Koert U, Jensen GJ, Thanbichler M. 2017.
733 Dynamics of the peptidoglycan biosynthetic machinery in the stalked budding bacterium *Hyphomonas*
734 *neptunium*. *Molecular Microbiology* **103**:875-895.

735 Deng X, Gonzalez Llamazares A, Wagstaff JM, Hale VL, Cannone G, McLaughlin SH, Kureisaite-Ciziene D,
736 Löwe J. 2019. The structure of bactofilin filaments reveals their mode of membrane binding and lack
737 of polarity. *Nature Microbiology* **4**:2357-2368.

738 Ducret A, Quardokus EM, Brun YV. 2016. MicrobeJ, a tool for high throughput bacterial cell detection and
739 quantitative analysis. *Nature Microbiology* **1**:16077.

740 Edwards D, Donachie WD. 1993. Construction of a triple deletion of penicillin-binding proteins 4, 5, and 6
741 in *Escherichia coli*. In: Bacterial growth and lysis, eds: de Pedro M, Höltje J-V, Löffelhardt W (New York
742 and London: Plenum Press), pp. 369–374.

743 Egan AJF, Errington J, Vollmer W. 2020. Regulation of peptidoglycan synthesis and remodelling. *Nature*
744 *Reviews Microbiology* **18**:446-460.

745 Evans R, O'Neill M, Pritzel A, Antropova N, Senior A, Green T, Žídek A, Bates R, Blackwell S, Yim J *et al.*
746 2022. Protein complex prediction with AlphaFold-Multimer. bioRxiv, DOI:
747 10.1101/2021.1110.1104.463034

748 Figueroa-Cuilan WM, Randich AM, Dunn CM, Santiago-Collazo G, Yowell A, Brown PJB. 2021. Diversifi-
749 cation of LytM protein functions in polar elongation and cell division of *Agrobacterium tumefaciens*.
750 *Frontiers in Microbiology* **12**:729307.

751 Firczuk M, Mucha A, Bochtler M. 2005. Crystal structures of active LytM. *Journal of Molecular Biology*
752 **354**:578-590.

753 Glauner B. 1988. Separation and quantification of muropeptides with high-performance liquid chromato-
754 graphy. *Analytical Biochemistry* **172**:451-464.

755 Goedhart J. 2021. SuperPlotsOfData – a web app for the transparent display and quantitative comparison
756 of continuous data from different conditions. *Molecular Biology of the Cell* **32**:470-474.

757 Goley ED, Comolli LR, Fero KE, Downing KH Shapiro, L. 2010. DipM links peptidoglycan remodelling to
758 outer membrane organization in *Caulobacter*. *Molecular Microbiology* **77**:56-73.

759 Grabowska M, Jagielska E, Czapinska H, Bochtler M, Sabala I. 2015. High resolution structure of an M23
760 peptidase with a substrate analogue. *Scientific Reports* **5**:14833.

761 Gurnani Serrano CK, Winkle M, Martorana AM, Biboy J, More N, Moynihan P, Banzhaf M, Vollmer W,
762 Polissi A. 2021. ActS activates peptidoglycan amidases during outer membrane stress in *Escherichia*
763 *coli*. *Molecular Microbiology* **116**:329-342.

764 Hallgren J, Tsirigos KD, Pedersen MD, Almagro Armenteros JJ, Marcatili P, Nielsen H, Krogh A, Winther O.
765 2022. DeepTMHMM predicts alpha and beta transmembrane proteins using deep neural networks.
766 bioRxiv, DOI: 10.1101/2022.04.08.487609

767 Hartmann R, van Teeseling MCF, Thanbichler M, Drescher K. 2020. BacStalk: A comprehensive and
768 interactive image analysis software tool for bacterial cell biology. *Molecular Microbiology* **114**:140-150.

769 Hay NA, Tipper DJ, Gygi D, Hughes C. 1999. A novel membrane protein influencing cell shape and multi-
770 cellular swarming of *Proteus mirabilis*. *Journal of Bacteriology* **181**:2008-2016.

771 Hughes HV, Lisher JP, Hardy GG, Kysela DT, Arnold RJ, Giedroc DP, Brun YV. 2013. Co-ordinate synthesis
772 and protein localization in a bacterial organelle by the action of a penicillin-binding-protein. *Molecular*
773 *Microbiology* **90**:1162-1177.

774 Hussain S, Wivagg CN, Szwedziak P, Wong F, Schaefer K, Izore T, Renner LD, Holmes MJ, Sun Y, Bisson-
775 Filho AW*, et al.* 2018. MreB filaments align along greatest principal membrane curvature to orient cell
776 wall synthesis. *Elife* **7**:e32471.

777 Jackson KM, Schwartz C, Wachter J, Rosa PA, Stewart PE. 2018. A widely conserved bacterial cytoskeletal
778 component influences unique helical shape and motility of the spirochete *Leptospira biflexa*. *Molecular*
779 *Microbiology* **108**:77-89.

780 Jaqaman K, Loerke D, Mettlen M, Kuwata H, Grinstein S, Schmid SL, Danuser G. 2008. Robust single-
781 particle tracking in live-cell time-lapse sequences. *Nature Methods* **5**:695-702.

782 Jumper J, Evans R, Pritzel A, Green T, Figurnov M, Ronneberger O, Tunyasuvunakool K, Bates R, Zidek A,
783 Potapenko A*, et al.* 2021. Highly accurate protein structure prediction with AlphaFold. *Nature* **596**:583-
784 589.

785 Jung A, Eisheuer S, Cserti E, Leicht O, Strobel W, Möll A, Schlimpert S, Kühn J, Thanbichler M. 2015.
786 Molecular toolbox for genetic manipulation of the stalked budding bacterium *Hyphomonas neptunium*.
787 *Applied and Environmental Microbiology* **81**:736-744.

788 Jung A, Rassbach A, Pulpetta RL, van Teeseling MCF, Heinrich K, Sobetzko P, Serrania J, Becker A,
789 Thanbichler M. 2019. Two-step chromosome segregation in the stalked budding bacterium
790 *Hyphomonas neptunium*. *Nature Communications* **10**:3290.

791 Klein EA, Schlimpert S, Hughes V, Brun YV, Thanbichler M, Gitai Z. 2013. Physiological role of stalk
792 lengthening in *Caulobacter crescentus*. *Communicative & Integrative Biology* **6**:e24561.

793 Koch MK, McHugh CA, Hoiczyk E. 2011. BacM, an N-terminally processed bactofilin of *Myxococcus*
794 *xanthus*, is crucial for proper cell shape. *Molecular Microbiology* **80**:1031-1051.
795 Kühn J, Briegel A, Mörschel E, Kahnt J, Leser K, Wick S, Jensen GJ, Thanbichler M. 2010. Bactofilins, a
796 ubiquitous class of cytoskeletal proteins mediating polar localization of a cell wall synthase in
797 *Caulobacter crescentus*. *EMBO Journal* **29**:327-339.
798 Kuru E, Tekkam S, Hall E, Brun YV, Van Nieuwenhze MS. 2015. Synthesis of fluorescent D-amino acids and
799 their use for probing peptidoglycan synthesis and bacterial growth *in situ*. *Nature Protocols* **10**:33-52.
800 Kysela DT, Randich AM, Caccamo PD, Brun YV. 2016. Diversity takes shape: understanding the mechanistic
801 and adaptive basis of bacterial morphology. *PLoS Biology* **14**:e1002565.
802 Larson MH, Gilbert LA, Wang X, Lim WA, Weissman JS, Qi LS. 2013. CRISPR interference (CRISPRi) for
803 sequence-specific control of gene expression. *Nature Protocols* **8**: 2180-2196.
804 Leicht O, van Teeseling MCF, Panis G, Reif C, Wendt H, Viollier PH, Thanbichler M. 2020. Integrative and
805 quantitative view of the CtrA regulatory network in a stalked budding bacterium. *PLoS Genetics*
806 **16**:e1008724.
807 Leifson E. 1964. *Hyphomicrobium neptunium sp. n*. *Antonie Van Leeuwenhoek* **30**:249-256.
808 Letunic I, Bork P. 2021. Interactive Tree Of Life (iTOL) v5: an online tool for phylogenetic tree display and
809 annotation. *Nucleic Acids Research* **49**:W293-W296.
810 Lin L, Osorio Valeriano M, Harms A, Søgaard-Andersen L, Thanbichler M. 2017. Bactofilin-mediated
811 organization of the ParAB*S* chromosome segregation system in *Myxococcus xanthus*. *Nature*
812 *Communications* **8**:1817.
813 Lord SJ, Velle KB, Mullins RD, Fritz-Laylin LK. 2020. SuperPlots: Communicating reproducibility and
814 variability in cell biology. *Journal of Cell Biology* **219**:e202001064.
815 Lupas A. 1996. Prediction and analysis of coiled-coil structures. *Methods in Enzymology* **266**:513-525.
816 Marblestone JG, Edavettal SC, Lim Y, Lim P, Zuo X, Butt TR. 2006. Comparison of SUMO fusion technology
817 with traditional gene fusion systems: enhanced expression and solubility with SUMO. *Protein Science*
818 **15**:182-189.
819 Margolin W. 2009. Sculpting the bacterial cell. *Current Biology* **19**:R812-R822.
820 Martinez LE, Hardcastle JM, Wang J, Pincus Z, Tsang J, Hoover TR, Bansil R, Salama NR. 2016. *Helicobacter*
821 *pylori* strains vary cell shape and flagellum number to maintain robust motility in viscous environments.
822 *Molecular Microbiology* **99**:88-110.
823 McQuillen R, Xiao J. 2020. Insights into the structure, function, and dynamics of the bacterial cytokinetic
824 FtsZ-ring. *Annual Review of Biophysics* **49**:309-341.
825 Mistry J, Chuguransky S, Williams L, Qureshi M, Salazar GA, Sonnhammer ELL, Tosatto SCE, Paladin L, Raj
826 S, Richardson LJ*, et al.* 2021. Pfam: The protein families database in 2021. *Nucleic Acids Research*
827 **49**:D412-D419.
828 Molisch H. 1907. Die Purpurbakterien nach neuen Untersuchungen (Jena: Gustav Fischer).
829 Möll A, Schlimpert S, Briegel A, Jensen GJ, Thanbichler M. 2010. DipM, a new factor required for
830 peptidoglycan remodelling during cell division in *Caulobacter crescentus*. *Molecular Microbiology*
831 **77**:90-107.
832 Moore RL. 1981. The biology of *Hyphomicrobium* and other prosthecate, budding bacteria. *Annual Review*
833 *of Microbiology* **35**:567-594.
834 Munk AC, Copeland A, Lucas S, Lapidus A, Del Rio TG, Barry K, Detter JC, Hammon N, Israni S, Pitluck S *et*
835 *al.* 2011. Complete genome sequence of *Rhodospirillum rubrum* type strain (S1). *Standards in Genomic*
836 *Sciences* **4**:293-302.

837 Nagai T, Ibata K, Park Es, Kubota M, Mikoshiba K, Miyawaki A. 2002. A variant of yellow fluorescent protein
838 with fast and efficient maturation for cell-biological applications. *Nature Biotechnology* **20**: 87-90.

839 Oviedo-Bocanegra LM, Hinrichs R, Rotter DAO, Dersch S, Graumann PL. 2021. Single molecule/particle
840 tracking analysis program SMTracker 2.0 reveals different dynamics of proteins within the RNA
841 degradosome complex in *Bacillus subtilis*. *Nucleic Acids Research* **49**:e112.

842 Paysan-Lafosse T, Blum M, Chuguransky S, Grego T, Pinto BL, Salazar GA, Bileschi ML, Bork P, Bridge A,
843 Colwell L *et al.* 2022. InterPro in 2022. *Nucleic Acids Research* **51**:D418-D427.

844 Persat A, Stone HA, Gitai Z. 2014. The curved shape of *Caulobacter crescentus* enhances surface
845 colonization in flow. *Nature Communications* **5**:3824.

846 Pfennig N, Trüper HG. 1971. Type and neotype strains of the species of phototrophic bacteria maintained
847 in pure culture. *International Journal of Systematic Bacteriology* **21**:19-24.

848 Plank M, Wadhams GH, Leake MC. 2009. Millisecond timescale slimfield imaging and automated
849 quantification of single fluorescent protein molecules for use in probing complex biological processes.
850 *Integrative Biology (Camb)* **1**:602-612.

851 Poggio S, Takacs CN, Vollmer W, Jacobs-Wagner C. 2010. A protein critical for cell constriction in the Gram-
852 negative bacterium *Caulobacter crescentus* localizes at the division site through its peptidoglycan-
853 binding LysM domains. *Molecular Microbiology* **77**:74-89.

854 Postma M, Goedhart J. 2019. PlotsOfData—A web app for visualizing data together with their summaries.
855 *PLOS Biology* **17**:e3000202.

856 R Development Core Team. 2012. R: a language and environment for statistical computing. The R
857 Foundation for Statistical Computing, Vienna, Austria.

858 Randich AM, Brun YV. 2015. Molecular mechanisms for the evolution of bacterial morphologies and
859 growth modes. *Frontiers in Microbiology* **6**:580.

860 Rohs PDA, Bernhardt TG. 2021. Growth and division of the peptidoglycan matrix. *Annual Review of*
861 *Microbiology* **75**:315-336.

862 Schindelin J, Arganda-Carreras I, Frise E, Kaynig V, Longair M, Pietzsch T, Preibisch S, Rueden C, Saalfeld S,
863 Schmid B *et al.* 2012. Fiji: an open-source platform for biological-image analysis. *Nature Methods*
864 **9**:676-682.

865 Schneider CA, Rasband WS, Eliceiri KW. 2012. NIH Image to ImageJ: 25 years of image analysis. *Nature*
866 *Methods* **9**:671-675.

867 Shaner NC, Campbell RE, Steinbach PA, Giepmans BN, Palmer AE, Tsien RY. 2004. Improved monomeric
868 red, orange and yellow fluorescent proteins derived from *Discosoma sp.* red fluorescent protein.
869 *Nature Biotechnology* **22**:1567-1572.

870 Shaner NC, Lambert GG, Chammas A, Ni Y, Cranfill PJ, Baird MA, Sell BR, Allen JR, Day RN, Israelsson M *et*
871 *al.* 2013. A bright monomeric green fluorescent protein derived from *Branchiostoma lanceolatum*.
872 *Nature Methods* **10**:407-409.

873 Shi C, Fricke P, Lin L, Chevelkov V, Wegstroth M, Giller K, Becker S, Thanbichler M, Lange A. 2015. Atomic-
874 resolution structure of cytoskeletal bactofilin by solid-state NMR. *Science Advances* **1**:e1501087.

875 Shi H, Bratton BP, Gitai Z, Huang KC. 2018. How to Build a bacterial cell: MreB as the foreman of *E. coli*
876 construction. *Cell* **172**:1294-1305.

877 Sichel SR, Bratton BP, Salama NR. 2022. Distinct regions of *H. pylori*'s bactofilin CcmA regulate protein-
878 protein interactions to control helical cell shape. *Elife* **11**:e80111.

879 Sycuro LK, Pincus Z, Gutierrez KD, Biboy J, Stern CA, Vollmer W, Salama NR. 2010. Peptidoglycan
880 crosslinking relaxation promotes *Helicobacter pylori*'s helical shape and stomach colonization. *Cell*
881 **141**:822-833.

882 Taylor JA, Bratton BP, Sichel SR, Blair KM, Jacobs HM, DeMeester KE, Kuru E, Gray J, Biboy J,
883 VanNieuwenhze MS *et al.* 2020. Distinct cytoskeletal proteins define zones of enhanced cell wall
884 synthesis in *Helicobacter pylori*. *Elife* **9**:e52482.
885 Taylor JA, Sichel SR, Salama NR. 2019. Bent bacteria: A comparison of cell shape mechanisms in
886 proteobacteria. *Annual Review of Microbiology* **73**:457-480.
887 Thanbichler M, Shapiro L. 2006. MipZ, a spatial regulator coordinating chromosome segregation with cell
888 division in *Caulobacter*. *Cell* **126**:147-162.
889 Typas A, Banzhaf M, Gross CA, Vollmer W. 2012. From the regulation of peptidoglycan synthesis to
890 bacterial growth and morphology. *Nature Reviews Microbiology* **10**:123-136.
891 Uehara T, Parzych KR, Dinh T, Bernhardt TG. 2010. Daughter cell separation is controlled by cytokinetic
892 ring-activated cell wall hydrolysis. *EMBO Journal* **29**:1412-1422.
893 van den Ent F, Johnson CM, Persons L, de Boer P, Löwe J. 2010. Bacterial actin MreB assembles in complex
894 with cell shape protein RodZ. *EMBO Journal* **29**: 1081-1090.
895 van Niel CB. 1944. The culture, general physiology, morphology, and classification of the non-sulfur purple
896 and brown bacteria. *Bacteriological Reviews* **8**:1-118.
897 van Teeseling MCF, de Pedro MA, Cava F. 2017. Determinants of bacterial morphology: from fundamen-
898 tals to possibilities for antimicrobial targeting. *Frontiers in Microbiology* **8**:1264.
899 Varadi M, Anyango S, Deshpande M, Nair S, Natassia C, Yordanova G, Yuan D, Stroe O, Wood G, Laydon A
900 *et al.* 2022. AlphaFold Protein Structure Database: massively expanding the structural coverage of
901 protein-sequence space with high-accuracy models. *Nucleic Acids Research* **50**:D439-D444.
902 Vasa S, Lin L, Shi C, Habenstein B, Riedel D, Kühn J, Thanbichler M, Lange A. 2015. β-Helical architecture
903 of cytoskeletal bactofilin filaments revealed by solid-state NMR. *Proceedings of the National Academy*
904 *of Sciences U S A* **112**:E127-136.
905 Vollmer W, Blanot D, de Pedro MA. 2008. Peptidoglycan structure and architecture. *FEMS Microbiology*
906 *Reviews* **32**:149-167.
907 Wagner JK, Brun YV. 2007. Out on a limb: how the *Caulobacter* stalk can boost the study of bacterial cell
908 shape. *Molecular Microbiology* **64**:28-33.
909 Wali TM, Hudson GR, Danald DA, Weiner RM. 1980. Timing of swarmer cell cycle morphogenesis and
910 macromolecular synthesis by *Hyphomicrobium neptunium* in synchronous culture. *Journal of*
911 *Bacteriology* **144**:406-412.
912 Wong F, Garner EC, Amir A. 2019. Mechanics and dynamics of translocating MreB filaments on curved
913 membranes. *Elife* **8**:e40472.
914 Yang DC, Blair KM, Salama NR. 2016. Staying in shape: the impact of cell shape on bacterial survival in
915 diverse environments. *Microbiology and Molecular Biology Reviews* **80**:187-203.
916 Zuckerman DM, Boucher LE, Xie K, Engelhardt H, Bosch J, Hoiczyk E. 2015. The bactofilin cytoskeleton
917 protein BacM of *Myxococcus xanthus* forms an extended beta-sheet structure likely mediated by
918 hydrophobic interactions. *PLoS One* **10**:e0121074.

919 ## Figure legends

920 **Figure 1. Bactofilin BacA is required for proper cell morphology in *H. neptunium*. (A)** Schematic repre-
921 sentation of the two bactofilin genes present in the *H. neptunium* genome. *bacA* lies adjacent to the M23
922 peptidase gene *lmdC*. Arrows indicate the direction of transcription. **(B)** Domain organization of BacA and
923 BacD from *H. neptunium*. The bactofilin polymerization domain (colored boxes) is flanked by non-struc-
924 tured N- and C-terminal regions. **(C)** Morphology of *H. neptunium* bactofilin mutants. Shown are represen-
925 tative cells of strains LE670 (wild type), EC28 (Δ*bacA*), EC23 (Δ*bacD*) and EC33 (Δ*bacAD*), imaged by
926 differential interference contrast (DIC) microscopy. Bar: 4 µm. **(D)** Transmission electron micrographs of
927 Δ*bacA* cells at the early stalked-cell stage. Bar: 1 µm. **(E)** Quantification of the proportion of phenotypically
928 abnormal stalked and budding cells in cultures of the strains analyzed in panel C (n = 100 cells per strain).
929 **(F)** Doubling times of the indicated *H. neptunium* strains. Bars represent the mean (± SD) of three indepen-
930 dent experiments (dots). Statistical significance was determined using Welch's non-paired t-test (*,
931 $p<0.05$; n.s., not significant). **(G)** Immunoblot analysis of the strains shown in panel C, performed using
932 anti-BacA antibodies.

933 **Figure 1—figure supplement 1. The dimorphic lifecycle of *H. neptunium*.** A motile, flagellated swimmer
934 sheds its flagellum and forms a stalk at the opposite cell pole. At a defined point in the cell cycle, the
935 terminal segment of the stalk dilates and develops into a new swimmer cell. After cell division, the new-
936 born swimmer cell first needs to differentiate into a stalked cell to initiate a new round of cell division,
937 whereas the stalked mother cell immediately enters the next replication cycle. The predominant growth
938 zones (Cserti et al., 2017) are indicated in red.

939 **Figure 1—figure supplement 2. Phenotypic analysis of *H. neptunium* bactofilin mutants. (A)** Immunoblot
940 analysis of strains LE670 (wild type), EC28 (Δ*bacA*) and EC41 (Δ*bacA* P_{Cu}::P_{Cu}-*bacA*) grown in the absence
941 (-*bacA*) and presence (+*bacA*) of 0.5 mM $CuSO_4$, performed with an anti-BacA antibody. **(B)** Rescue of the
942 phenotype of a Δ*bacA* mutant by ectopic expression of *bacA*. Cells of strain EC41 (Δ*bacA* P_{Cu}::P_{Cu}-*bacA*)
943 were grown in copper-free medium, induced by the addition of copper, and imaged after the indicated
944 time incubation times. Bar: 3 µm. **(C)** Quantification of the proportion of phenotypically abnormal stalked
945 and budding cells in the cultures of strains EC41 (Δ*bacA* P_{Cu}::P_{Cu}-*bacA*) and EC43 (Δ*bacA* P_{Zn}::P_{Zn}-*bacD*)
946 analyzed in panels B and E before (t=0 h) and 24 h after induction (n = 100 cells per time point). **(D)**
947 Doubling times of the indicated *H. neptunium* strains. Strain EC41 (Δ*bacA* P_{Cu}::P_{Cu}-*bacA*) as analyzed in the
948 absence (-) and presence (+) of copper. Strain LE670 (wild-type) grown in copper-free medium is shown
949 as a control. Bars represent the mean (± SD) of three independent experiments (dots). Statistical

950 significance was determined using Welch's non-paired t-test (n.s., not significant). **(E)** Transmission elec-
951 tron micrographs of Δ*bacD* cells at the swimmer and stalk cell stage. Bar: 1 µm. **(F)** DIC images of a Δ*bacA*
952 mutant overproducing BacD from a zinc-inducible promoter. Cells of strain EC43 (Δ*bacA* P_{Zn}::P_{Zn}-*bacD*)
953 were grown in inducer-free medium, induced by the addition of 0.5 mM $ZnSO_4$, and imaged after the
954 indicated incubation times. Bar: 3 µm.

955 **Figure 2. Lack of BacA leads to uncontrolled growth of the stalk and bud compartments. (A)** Immunoblot
956 showing the levels of BacA in strain EC41 (Δ*bacA* P_{Cu}-*bacA*) over the course of BacA depletion. Cells were
957 grown in copper-containing medium, washed and transferred to inducer-free medium. At the indicated
958 time points, samples were withdrawn and subjected to immunoblot analysis. Strains LE670 (wild type)
959 and EC28 (Δ*bacA*) were included as controls. The position of BacA is indicated. **(B)** Morphological defects
960 induced by BacA depletion. Cells of strains LE670 (wild type) and EC41 (Δ*bacA* P_{Cu}-*bacA*) were grown in
961 medium containing 0.5 mM $CuSO_4$, washed, and incubated for 6 h in inducer-free medium before they
962 were transferred onto ASS-agarose pads lacking inducer and imaged at the indicated time points. Bar: 2
963 µm. **(C)** Changes in the growth pattern of *H. neptunium* in the absence of bactofilins. Cells of strains LE670
964 (wild type) and EC33 (Δ*bacAD*) were stained with the fluorescent D-amino acid HADA prior to analysis by
965 fluorescence microscopy. Shown are representative images of cells at different developmental stages.
966 Bars: 2 µm.

967 **Figure 2—figure supplement 1. Growth of Δ*bacAD* cells in a microfluidic flow cell.** Cells of strain EC33
968 (Δ*bacAD*) were flushed into a microfluidic flow cell and imaged at the indicated time points (in h). Bar:
969 3 µm.

970 **Figure 2—video 1. Unconstrained growth of a bactofilin-deficient *H. neptunium* mutant.** Cells of strain
971 EC33 (Δ*badAD*) were grown in a microfluidic flow cell and imaged by DIC microsopy at 15 min intervals.
972 Bar: 2 µm.

973 **Figure 2—video 2. Normal growth of the *H. neptunium* wild-type strain.** Cells of strain LE670 (wild type)
974 were grown in a microfluidic flow cell and imaged by DIC microscopy at 5 min intervals. Bar: 2 µm.

975 **Figure 2—figure supplement 2. Muropeptide profiles of different *H. neptunium* strains.** Cell walls of
976 strains LE670 (wild type), EC28 (Δ*bacA*), EC23 (Δ*bacD*) and EC33 (Δ*bacAD*) were digested with cellosyl to
977 release muropeptides, which were reduced and separated by HPLC. The identities of major muropeptide
978 species, assigned based on the previously reported retention times (Cserti et al., 2017; Glauner, 1988),
979 are given above the corresponding peaks. Tri, Tetra and Penta stand for N-acetylglucosamine-N-

980 acetylmuramitol tripeptide, tetrapeptide and pentapeptide, respectively. “Anh” indicates muropeptides
981 containing 1,6-anhydromuramic acid.

982 **Figure 3. BacA and BacD co-polymerize into filamentous structures. (A)** Model of a BacA trimer gener-
983 ated with AlphaFold-Multimer (Evans et al., 2022). Only residues P34-D138 are shown for each subunit.
984 **(B)** Visualization of BacA polymers. Purified BacA-His_6 was stained with uranyl acetate and imaged by
985 transmission electron microscopy (TEM). Arrowheads point to BacA filaments. Asterisks indicate filament
986 bundles and sheets. Bars: 200 nm. **(C)** Copolymerization of BacA and BacD after heterologous co-
987 expression in *E. coli*. Cells of *E. coli* BL21(DE3) transformed with plasmid pEC121 (P_{T7}-*bacA-eyfp* P_{T7}-*bacD-*
988 *ecfp*) were grown in LB medium containing 5 % glucose and induced with 0.5 mM IPTG prior to imaging.
989 Bar: 3 µm.

990 **Figure 3—figure supplement 1.** Localization patterns of BacA-YFP and BacD-CFP upon heterologous over-
991 production in *E. coli*. **(A)** Co-localization of BacA-YFP and BacD-CFP in cells of *E. coli* BL21(DE3) transformed
992 with plasmid pEC121 (P_{T7}-*bacA-eyfp* P_{T7}-*bacD-ecfp*). **(B)** Localization of BacA-YFP in cells of *E. coli*
993 BL21(DE3) transformed with plasmid pEC119 (P_{T7}-*bacA-eyf*) **(C)** Localization of BacD-CFP in *E. coli*
994 BL21(DE3) transformed with plasmid pEC120 ($P_{T7\text{-}bacD\text{-}ecfp}$). All strains were grown in LB medium containing
995 5% glucose and induced with 0.5 mM IPTG prior to imaging. Bars: 2 µm.

996 **Figure 4. BacA and BacD show a dynamic, cell cycle-dependent localization pattern. (A)** Localization
997 pattern of BacA-YFP. Cells of strain EC61 (*bacA*::*bacA-eyfp*) were transferred to agarose pads and imaged
998 at 20-min intervals. Shown are overlays of DIC and fluorescence images of a representative cell, with YFP
999 fluorescence shown in red. Scale bar: 3 µm. **(B)** Demographic analysis of BacA-YFP localization in swimmer
1000 (left), stalked (middle), and budding (right) cells of strain EC61 (*bacA*::*bacA-eyfp*). The fluorescence inten-
1001 sity profiles measured for cells of each type were sorted according to cell length and stacked on each
1002 other, with the shortest cell shown at the top and the longest cell shown at the bottom (n=250 swimmer
1003 cells, 215 stalked cells and 49 budding cells). Dotted red lines indicate the positions to which cells were
1004 aligned. **(C)** Demographic analysis of BacD-Venus localization. Cells of strain EC67 (*bacD*::*bacD-venus*)
1005 were analyzed as described in panel B (n=416 swimmer cells, 248 stalked cells and 45 budding cells). **(D)**
1006 Co-localization of BacA and BacD in cells of strain EC68 (*bac*A::*bacA-eyfp bacD*::*bacD-mCherry*). Shown are
1007 DIC images and overlays of the YFP and mCherry signals of representative cells, arranged according to
1008 their developmental state. The individual signals are shown in **Figure S6A**. The Pearson’s Correlation Coef-
1009 ficient (PCC) of the two fluorescence signals in a random population of cells (n=454) is 0.506. Bar: 1 µm.

1010 **Figure 4—figure supplement 1. Stability of the fluorescently tagged bactofilin derivatives used in this**
1011 **study.** Cells of strains LE670 (wild type), EC61 (*bacA*::*bacA-eyfp*), MO78 (*bacA*::*bacA*$_{F130R}$*-eyfp*) and EC67
1012 (*bacD*::*bacD-venus*) were subjected to immunoblot analysis using anti-GFP antibodies.

1013 **Figure 4—figure supplement 2. Localization dynamics of BacA-YFP.** Cells of strain EC61 (*bacA*::*bacA-eyfp*)
1014 were flushed into a microfluidic flow cell and imaged at 15-min intervals over multiple cell cycles. Shown
1015 are overlays of DIC and fluorescence images. Bar: 2 µm.

1016 **Figure 4—video 1. Localization dynamics of BacA-YFP (example 1).** Cells of strain EC61 (*bacA::bacA-eyfp*)
1017 were grown in a microfluidic flow cell and imaged at 15 min intervals. Shown are overlays of DIC and
1018 fluorescence images. YFP fluorescence is shown in red for better visibility. Bar: 2 µm.

1019 **Figure 4—video 2. Localization dynamics of BacA-YFP (example 2).** Cells of strain EC61 (*bacA::bacA-eyfp*)
1020 were grown in a microfluidic flow cell and imaged at 15 min intervals. Shown are overlays of DIC and
1021 fluorescence images. YFP fluorescence is shown in red for better visibility. Bar: 2 µm.

1022 **Figure 4—video 3. Localization dynamics of BacA-YFP (example 3).** Cells of strain EC61 (*bacA::bacA-eyfp*)
1023 were grown in a microfluidic flow cell and imaged at 15 min intervals. Shown are overlays of DIC and
1024 fluorescence images. YFP fluorescence is shown in red for better visibility. Bar: 2 µm.

1025 **Figure 4—figure supplement 3. Co-localization of BacA and BacD.** Shown are the individual fluorescence
1026 images of strain EC68 (*bac*A::*bacA-eyfp bacD*::*bacD-mCherry*) used to generate the overlays in **Figure 4D**.
1027 Bar: 1 µm.

1028 **Figure 4—figure supplement 4. Partial independence of BacA and BacD localization at the onset of the**
1029 **budding process.** Shown are exemplary cells of strain EC68 (*bacA*::*bacA-eyfp bacD*::*bacD-mCherry*) in
1030 which BacA-YFP and BacD-CHY do not fully co-localize. Bar: 2 µm.

1031 **Figure 4—figure supplement 5. Random localization of BacD complexes in the absence of BacA.** Cells of
1032 strain EC60 (Δ*bacA* P_{Zn}::P_{Zn}-*bacD-venus*) were grown in inducer-free medium and then induced for 4 h
1033 with 0.5 mM $ZnSO_4$ prior to imaging. Bar: 3 µm.

1034 **Figure 4—figure supplement 6. Localization and functionality of BacA$_{F130R}$-YFP.** Cells of strain MO78
1035 (*bacA*::*bacA*$_{F130R}$*-eyfp*), producing the polymerization-deficient BacA$_{F130R}$-YFP variant instead of the native
1036 protein, were grown to exponential phase and imaged. Bar: 3 µm.

1037 **Figure 5. The bactofilin cytoskeleton is required to confine the elongasome to the mother cell and bud**
1038 **compartments.** Localization of eYFP-RodZ in the *H. neptunium* wild-type and Δ*bacAD* backgrounds.

1039 Shown are representative cells of strain EC93 (*rodZ*::*eyfp-rodZ*) and SP221 (Δ*bacAD rodZ*::*eyfp-rodZ*)
1040 imaged by DIC and fluorescence microscopy and arranged according to their developmental state.
1041 Arrowheads indicate cellular extensions that show eYFP-RodZ foci. Bar: 2 µm.

1042 **Figure 5—video 1. Localization of YFP-RodZ during stalk synthesis in the wild-type background.** Cells of
1043 strain EC93 (*rodZ*::*eyfp-rodZ*) were immobilized on pads made of 1% agarose in ASS medium and imaged
1044 at 2 min intervals. Bar: 2 µm.

1045 **Figure 5—video 2. Localization of YFP-RodZ during bud formation in the wild-type background.** Cells of
1046 strain EC93 (*rodZ*::*eyfp-rodZ*) were immobilized on pads made of 1% agarose in ASS medium and imaged
1047 at 2 min intervals. Bar: 2 µm.

1048 **Figure 5—video 3. Localization of YFP-RodZ during pseudo stalk synthesis in the Δ*bacAD* background.**
1049 Cells of strain SP221 (Δ*bacAD rodZ*::*eyfp-rodZ*) were immobilized on pads made of 1% agarose in ASS
1050 medium and imaged at 2 min intervals. Bar: 2 µm.

1051 **Figure 5—video 4. Localization of YFP-RodZ within within early stalks in the Δ*bacAD* background.** Cells
1052 of strain SP221 (Δ*bacAD rodZ*::*eyfp-rodZ*) were immobilized on pads made of 1% agarose in ASS medium
1053 and imaged at 2 min intervals. Bar: 2 µm.

1054 **Figure 5—video 5. Localization of YFP-RodZ in amorphous cells in the Δ*bacAD* background.** Cells of strain
1055 SP221 (Δ*bacAD rodZ*::*eyfp-rodZ*) were immobilized on pads made of 1% agarose in ASS medium and
1056 imaged at 2 min intervals. Bar: 2 µm.

1057 **Figure 6. The single-particle dynamics of BacA change over the course of the cell cycle. (A)** Representa-
1058 tive heat maps showing the sum of single-particle positions observed in live-cell single-particle localization
1059 microscopy studies of a swimmer, stalked and budding cell producing BacA-YFP (EC61) or a mutant cell
1060 producing the polymerization-deficient $BacA_{F130R}$-YFP variant (MO78). Insets show the corresponding
1061 bright-field images. Bars: 1 µm. **(B)** Mean-squared displacement (MSD) analysis of the mobility of BacA-
1062 YFP in wild-type swimmer (n=100), stalked (n=105) and budding (n=101) cells (EC61). Cells (n=110) produc-
1063 ing the $BacA_{F130R}$-YFP were analyzed as a control (MO78). Error bars indicate the standard deviation. **(C)**
1064 Bubble plots showing the proportions of mobile and immobile particles (size of the bubbles) and the cor-
1065 responding average diffusion constants (y-axis) in the cells analyzed in panel B.

1066 **Figure 6—video 1. Tracking of single BacA-YFP particles in representative cells at different stages of the**
1067 **cell cycle.** Shown are stream acquisitions (20-ms intervals) of *H. neptunium* cells producing wild-type

1068 BacA-YFP (EC61) or the polymerization-deficient $BacA_{F130R}$-YFP variant (MO78) in place of the native BacA
1069 protein at different developmental stages. Bar: 1 µm

1070 **Figure 6—figure supplement 1. Single-particle tracking analysis of BacA-YFP.** The images show the sums
1071 of all single-molecule tracks obtained for individual *H. neptunium* swimmer, stalked and budding cell
1072 producing BacA-YFP (EC61) or for a mutant cell producing the polymerization-deficient $BacA_{F130R}$-YFP
1073 variant (MO78). Cell outlines are indicated by white lines. Inserts show the corresponding bright-field
1074 images. Bars: 1 µm.

1075 **Figure 6—figure supplement 2. Single-particle tracking analysis of BacA-YFP mobility.** Shown is a
1076 Gaussian mixture model (GMM) analysis of the mobility of the BacA-YFP variants plotted in **Figure 5C**. The
1077 distributions of the frame-to-frame displacements in both x and y direction from single-particle tracking
1078 experiments were fitted to a two-component Gaussian function (sum in black), assuming a fast-diffusing
1079 mobile (dotted blue lines) and a slow-diffusing (dotted red lines) population.

1080 **Figure 7. Putative operons comprising adjacent BacA and M23 peptidase genes are widely conserved**
1081 **among bacteria. (A)** Arrangement of *bacA* and *lmdC* genes in species whose BacA homolog has a proven
1082 role in cell morphogenesis. **(B)** Co-conservation of BacA and M23 peptidase genes across different bacte-
1083 rial phyla. Bioinformatic analysis was used to identify genomes that contained a bactofilin gene located
1084 next to an M23 peptidase gene. After retrieval of the taxonomy IDs of the corresponding species from the
1085 National Center for Biotechnology Information (NCBI) website, a phylogenetic tree of the species was
1086 created using the iTOL server (Letunic and Bork, 2021). Abbreviations: DT (Deinococcus-Thermus group),
1087 FCB (Fibrobacteres-Chlorobi-Bacteroidetes group), β (β-proteobacteria), δ (δ-proteobacteria). The full list
1088 of species used and details on the genes identified are provided in **Figure 7—Dataset 1.**

1089 **Figure 8. LmdC is a peptidoglycan hydrolase with DD-endopeptidase activity. (A)** Predicted domain archi-
1090 tecture of *H. neptunium* LmdC. The predicted positions of the transmembrane helix (TM), the three coiled-
1091 coil regions (CC) and the M23 peptidase domain are indicated. **(B)** Alignment of the amino acid sequences
1092 of multiple M23 peptidases showing the conservation of the catalytic residues in LmdC. Residues required
1093 to coordinate the catalytic Zn^{2+} ion of LytM from *S. aureus* (Firczuk et al., 2005) are indicated by arrow-
1094 heads. The proteins shown are EnvC from *E. coli* (UniProt: P37690), NlpD from *E. coli* (P0ADA3), LytM from
1095 *S. aureus* (O33599), MepM from *E. coli* (P0AFS9) and LmdC from *H. neptunium* (Q0BYX6). **(C)** Predicted
1096 molecular structure of *H. neptunium* LmdC, generated with Alphafold2 (Jumper et al., 2021). The different
1097 domains of the protein and the position of proline 66, which terminates the N-terminal fragment of LmdC
1098 used for the *in vivo* analyses in this study ($LmdC_{1-66}$) are indicated. **(D)** HPLC traces showing the muro-

1099 peptide profile of peptidoglycan treated with LmdC. Cell walls were incubated with the isolated M23 pep-
1100 tidase domain of LmdC at pH 5.0 and pH 7.5. Subsequently, muropeptides were released with cellosyl,
1101 reduced and separated by HPLC. A control sample lacking LmdC (No protein). The nature of the major
1102 products is indicated above the peaks. Tri, Tetra and Penta stand for N-acetylglucosamine-N-acetylmura-
1103 mitol tripeptide, tetrapeptide and pentapeptide, respectively. A quantification of the relative abundance
1104 of different muropeptide species in each condition, based on a comparison of the relative integrated peak
1105 areas, is provided in **Figure 8—Dataset 1**. **(E)** Structure of a TetraTetra muropeptide. Abbreviations: G (N-
1106 acetylglucosamine), M (N-acetylmuramic acid). The cleavage site of LmdC is indicated by a red arrowhead.

1107 **Figure 9. LmdC interacts with BacA to mediate *H. neptunium* morphogenesis. (A)** Schematic represen-
1108 tation of the integrative plasmid pdCas9Entry, enabling CRISPR interference (CRISPRi) in *H. neptunium*.
1109 The plasmid harbors a chromosomal fragment containing the copper-inducible P_{Cu} promoter, followed by
1110 a gene encoding a nuclease-deficient variant of Cas9 (dCas9). It also contains an sgRNA expression cassette
1111 composed of the constitutive $P_{HNE0038}$ promoter, a BbsI cloning site for the insertion of target-specific DNA
1112 fragments, a sequence encoding an optimized sgRNA handle (Chen et al., 2013) and a transcriptional ter-
1113 minator (ter). Other features of the plasmid are a replication initiator gene (*rep*), a kanamycin resistance
1114 gene (*npt1*), an origin of transfer (*oriT*) and a strong transcriptional terminator (*rrnB*T1T2) that is placed
1115 upstream of the P_{Cu}-containing fragment. The DNA sequence of the sgRNA expression cassette is given in
1116 **Figure 9–figure supplement 1**. **(B)** Schematic showing the integration of a pdCas9Entry derivative into the
1117 *H. neptunium* chromosome by single homologous recombination at the P_{Cu} locus. **(C)** Mechanism of the
1118 CRISPRi-mediated repression of *lmdC* expression. In the presence of inducer, dCas9 interacts with a con-
1119 stitutively produced sgRNA that targets bases 51-72 of the non-coding strand of *lmdC* (sg*lmdC*). The
1120 formation of the interference complex creates a roadblock that blocks the transcription of *lmdC* by RNA
1121 polymerase. **(D)** Immunoblot analysis verifying the CRISPRi-mediated depletion of LmdC. Strain SU34
1122 (*lmdC*::*lmdC-HA*), which produces a fully functional variant of LmdC carrying the HA affinity tag inserted
1123 in between the transmembrane helix and the coiled-coil domain, was transformed with pdCas9Entry
1124 (empty vector) or plasmid pJH13 (sg*lmdC*). The resulting strains (SP249 and SP236) were grown for 24 h
1125 in the absence (-) or presence (-) of 0.3 mM $CuSO_4$ and subjected to immunoblot analysis with an anti-HA
1126 antibody. The wild-type strain (LE670), the parental strain SU34 as well as the uninduced pre-cultures
1127 (pre) of strains SP249 and SP236 used for the experiment were analyzed as controls. A non-specific band
1128 served as a loading control (LC). **(E)** Morphology of *H. neptunium* cells depleted of LmdC. Shown are
1129 representative cells of strains SP236 (*lmdC*::*lmdC*-HA pJH13) (sg*lmdC*) and SP249 (*lmdC*::*lmdC*-HA
1130 pCas9Entry) (empty vector) grown for 24 h in the absence (control) or presence (+ dCas9) of 0.3 mM

1131 $CuSO_4$. Cells were imaged by DIC and fluorescence microscopy. Bar: 2 µm. **(F)** Quantification of the
1132 proportion of phenotypically abnormal stalked and budding cells in the cultures of strain SP236
1133 (*lmdC*::*lmdC*-HA pJH13) analyzed in panel E (n=100 cells per condition). **(G)** Bio-layer interferometric
1134 analysis of the interaction between cytoplasmic domain of LmdC and BacA. Sensors derivatized with a
1135 biotinylated synthetic peptide comprising the N-terminal cytoplasmic region of LmdC (amino acids 1-38)
1136 were probed with the indicated concentrations of BacA. After the association of BacA, the sensors were
1137 transferred to protein-free buffer to induce BacA dissociation. The interaction kinetics were followed by
1138 monitoring the wavelength shifts resulting from changes in the optical thickness of the sensor surface
1139 during association or dissociation of the analyte. The extent of non-specific binding of BacA to the sensor
1140 surface was negligible (control). **(H)** Affinity of the BacA-LmdC interaction. The maximal wavelength shifts
1141 measured in the experiment shown in panel D were plotted against the corresponding BacA concentra-
1142 tion. The data were fitted to a one-site binding model, yielding an apparent K_d value of ~15 µM.

1143 **Figure 9—figure supplement 1. Characterization of the phenotype induced by the CRISPRi-mediated**
1144 **depletion of LmdC in *H. neptunium*. (A)** Sequence of the sgRNA expression cassette of pdCas9Entry. The
1145 different parts of the sequence are colored as defined in the schematic on top. The BsbI recognition and
1146 cut sites are indicated by arrows. **(B)** Morphological diversity of *H. neptunium* cells depleted of LmdC.
1147 Shown are representative cells of strains SP236 (*lmdC*::*lmdC*-HA pJH13) (sg*lmdC*) and SP249 (*lmdC*::*lmdC*-
1148 HA pCas9Entry) (empty vector) grown for 24 h in the absence (control) or presence (+ dCas9) of 0.3 mM
1149 $CuSO_4$. Cells were imaged by DIC microscopy. Bar: 2 µm. **(C)** Doubling times of the strains analyzed in panel
1150 B in the absence (-Cu) or presence (+Cu) of 0.3 mM $CuSO_4$. Bars represent the mean (± SD) of three
1151 independent experiments (dots). Statistical significance was determined using Welch's non-paired t-test
1152 (n.s., not significant).

1153 **Figure 10. BacA and LmdC contribute to cell morphogenesis in *R. rubrum*. (A)** Schematic representation
1154 of the *bacA*-*lmdC* operon in *R. rubrum*. **(B)** Domain organization of LmdC and BacA from *R. rubrum*. LmdC
1155 consists of a transmembrane helix (TM) followed by a coiled-coil-rich region and a C-terminal M23 pepti-
1156 dase domain (M23). The bactofilin polymerization domain (green box) is flanked by non-structured N- and
1157 C-terminal regions. Numbers indicate the first and last amino acid of a domain. **(C)** Phenotypes of *R. rub-*
1158 *rum* wild-type (S1), Δ$bacA_{Rs}$ (SP70), Δ$lmdC_{Rs}$ (SP68) and Δ$bacA_{Rs}$ Δ$lmdC_{Rs}$ (SP116) cells, imaged using phase-
1159 contrast microscopy. Bar: 5 µm. **(D)** Superplots showing the distribution of cell sinuosities in populations
1160 of the indicated *R. rubrum* strains. Small dots represent the data points, large dots represent the median
1161 values of the three independent experiments shown in the graphs (dark blue, light blue, grey). The mean

1162 of the three median values is indicated by a horizontal red line. Whiskers represent the standard deviation.
1163 *** p<0.005; ns, not significant; t-test). **(E)** Co-localization of BacA$_{Rs}$-CHY and LmdC$^{N}_{Rs}$-mNG in the Δ*lmdC*$_{Rs}$
1164 background (SP119). The Pearson's Correlation Coefficient (PCC) of the two fluorescence signals in a
1165 random subpopulation of cells is 0.916. Scale bar: 5 µm. **(F)** Schematic showing the approach used to
1166 quantify the distribution of proteins along the outer and inner curve of a cell in panel G. **(G)** Demographs
1167 showing the enrichment of BacA-CYH and LmdC^{N}-mNG at the inner curve the populations of strain SP119
1168 analyzed in panel E (n=200 per strain). The white dashed line represents the point of transition from the
1169 outer to the inner curve. **(H)** Localization of BacA$_{Rs}$-mNG in the Δ*lmdC*$_{Rs}$ background (SP98). Bar: 5 µm. **(I)**
1170 Localization of LmdC$_{Rs}$-mNG in the Δ*bacA*$_{Rs}$ background (SP118). Bar: 5 µm. **(J)** Demographs showing the
1171 outer-versus-inner curve distribution of BacA$_{Rs}$-mNG in the Δ*lmdC*$_{Rs}$ background (SP98; n=200) and
1172 LmdC$^{N}_{Rs}$-mNG in the Δ*bacA*$_{Rs}$ background (SP118; n=200). The white dashed line represents the point of
1173 transition from the outer to the inner curve.

1174 **Figure 10—figure supplement 1. Analysis of BacA and LmdC from *R. rubrum*. (A)** Clearer visualization of
1175 the abnormal curvature of BacA- and LmdC-deficient *R. rubrum* cells by inhibition of cell division. Cells of
1176 strains SP68 (Δ*lmdC*), SP70 (Δ*bacA*) and SP116 (Δ*lmdC* Δ*bacA*) were treated with 5 µg/ml cefalexin (Cfx)
1177 for 6 h. Bar: 5 µm. **(B)** Muropeptide profiles of different *R. rubrum* strains. Cell walls of strains S1 (wild
1178 type), SP70 (Δ*bacA*$_{Rs}$) and SP68 (Δ*lmdC*) were digested with cellosyl to release muropeptides, which were
1179 reduced and separated by HPLC chromatography. The identities of major muropeptide species, assigned
1180 based on the previously reported retention times (Glauner, 1988), are given above the corresponding
1181 peaks. Tetra stands for N-acetylglucosamine-N-acetylmuramitol tetrapeptide. "Anh" indicates muropep-
1182 tides containing 1,6-anhydromuramic acid.

1183 **Figure 10—figure supplement 2. Cell lengths of *R. rubrum* strains.** Superplots showing the distribution of
1184 cell sinuosities in populations of strains S1 (wild type), SP105 (Δ*bacA*$_{Rs}$ P$_{bacA}$-*bacA*$_{Rs}$) and SP109
1185 (*bacA*$_{Rs}$::*bacA*$_{Rs}$-*mCherry*). Small dots represent the data points, large dots represent the median values of
1186 the three independent experiments shown in the graphs (dark blue, light blue, grey). The mean of the
1187 three median values is indicated by a horizontal line. Whiskers represent the standard deviation. ***
1188 p<0.005; ns, not significant; t-test).

1189 **Figure 10—figure supplement 3. Lysis of *E. coli* upon heterologous expression of full-length *R. rubrum***
1190 ***lmdC*.** Shown are cells of *E. coli* Rosetta(DE3)pLysS harboring pSP120 (P$_{T7}$-*lmdC*$_{Rs}$) or the corresponding
1191 empty vector imaged 4h after the induction of gene expression with 0.5 mM IPTG. Arrowheads indicate
1192 ghost cells, cell debris, lysing cells or strongly elongated cells. Scale bar: 5 µm.

1193 **Figure 10—figure supplement 4. Analysis of *R. rubrum* strains producing fluorescent protein fusions. (A)**
1194 Domain architectures of the native LmdC$_{Rs}$ protein and the truncated LmdC$^{N}_{Rs}$-mNG reporter construct
1195 used for localization studies. The transmembrane helix is shown in purple. Abbreviations: CC (coiled-coil
1196 domain), M23 (M23 peptidase domain), mNG (mNeongreen). **(B)** Levels of the LmdC$^{N}_{Rs}$-mNG fusion in
1197 different *R. rubrum* strains. Strains SP98 (Δ*lmdC$_{Rs}$ bacA$_{Rs}$*::*bacA$_{Rs}$-mNeongreen*), SP114 (*bacA$_{Rs}$*::*bacA$_{Rs}$-*
1198 *mCherry* P$_{lmdC}$-*lmdC$^{N}_{Rs}$-mNeongreen*), SP118 (Δ*bacA* Δ*lmdC* P$_{lmdC}$-*lmdC$_{1-80}$-mNeongreen*) and SP119
1199 (*bacA*::*bacA-mCherry* Δ*lmdC* P$_{lmdC}$-*lmdC$_{1-80}$-mNeongreen*) were subjected to immunoblot analysis with an
1200 anti-mNeonGreen antibody. Predicted molecular weights: BacA$_{Rs}$-mNG (44.8 kDa), LmdC$^{N}_{Rs}$-mNG fusion
1201 (35.9 kDa) **(C)** Levels of the BacA$_{Rs}$-CHY fusion in different *R. rubrum* strains. Strains SP109 (*bacA$_{Rs}$*::*bacA$_{Rs}$-*
1202 *mCherry*), SP114 (*bacA$_{Rs}$*::*bacA$_{Rs}$-mCherry* P$_{lmdC}$-*lmdC$^{N}_{Rs}$-mNeongreen*), SP117 (*bacA$_{Rs}$*::*bacA$_{Rs}$-mCherry*
1203 Δ*lmdC*) and SP119 (*bacA$_{Rs}$*::*bacA$_{Rs}$-mCherry* Δ*lmdC* P$_{lmdC}$-*lmdC$^{N}_{Rs}$-mNeongreen*) were subjected to
1204 immunoblot analysis with an anti-mCherry antibody. The predicted molecular weight of BacA$_{Rs}$-CHY is 44.9
1205 kDa. **(D)** Co-localization of BacA$_{Rs}$-CHY and LmdC$_{Rs}$-mNG in *R. rubrum* cells carrying the native *lmdC$_{Rs}$* gene.
1206 The Pearson's Correlation Coefficient (PCC) of the two fluorescence signals in a random subpopulation of
1207 cells (n=177) is 0.54. Scale bar: 5 µm.

1208 **Figure 11. The β-hairpin in the cytoplasmic region of LmdC is critical for BacA binding. (A)** Predicted
1209 structure of LmdC^{N}, comprising the first 80 amino acids of LmdC. The transmembrane domain is colored
1210 light blue. The cytoplasmic domain includes a conserved β-hairpin motif. **(B)** Clusters of amino acids
1211 mutated for the analysis of BacA-LmdC interaction. Mutated amino acids are shown as red sticks. **(C)**
1212 Localization of BacA$_{Rs}$-CHY and the indicated LmdC$^{N}_{Rs}$-mNG variants in the Δ*lmdC$_{Rs}$* background. The
1213 Pearson's Correlation Coefficient (PCC) of the two fluorescence signals in a random subpopulation of cells
1214 is 0.914 for the wild type fusion (SP119), 0.887 for the R25A-H26A-L27A variant (SP237) and 0.827 for the
1215 R30A S31A variant (SP238). Scale bar: 5 µm. **(D,E)** Demographs showing the distribution of BacA-mCherry
1216 and (D) R25A-H26A-L27A variant (SP237) or R31A-S31A variant (SP238) of LmdC^{N}-mNG along the outer
1217 and inner curve of the cell (n=200 per strain). The white line marks the point of transition from the outer
1218 and the inner curve. The analysis was performed as described in **Figure 10F**.

1219 **Figure 12. Model of the roles of BacA and LmdC in *H. neptunium* and *R. rubrum* cell morphogenesis. (A)**
1220 Cell morphogenesis in *H. neptunium* wild-type (top) and Δ*bacAD* cells (bottom). In wild-type cells, BacA
1221 polymers form a complex with the DD-endopeptidase LmdC at the future stalked pole. The hydrolytic
1222 activity of LmdC, possibly stimulated by its interaction with BacA, helps to curve the cell wall at the
1223 incipient stalk base and thus determine stalk morphology. The zone of high positive inner cell curvature

1224 and, potentially, the physical barrier constituted by the bactofilin polymer prevent the movement of
1225 elongasome complexes from the mother cell body into the stalk, thereby limiting peptidoglycan biosyn-
1226 thesis to the stalked cell pole. At a later stage, the bactofilin-LmdC complex localizes close to the tip of the
1227 stalk and again generates a ring-shaped zone of positive cell curvature, thereby promoting the remodeling
1228 of the stalk tip into a spherical bud. At the onset of the budding process, elongasome complexes accumu-
1229 late in the nascent bud by a so-far unknown mechanism. The positively curved bud neck and the bactofilin
1230 polymers prevent the movement of elongasome complexes from the bud into the stalk, thereby limiting
1231 cell growth to the bud compartment. In the Δ*bacAD* mutant, cells fail to concentrate LmdC at the future
1232 stalk base and bud neck. As a consequence, peptidoglycan biosynthesis is no longer limited to the different
1233 growth zones, leading to pseudo-stalk formation and unregulated bud expansion. **(B)** Bactofilin-mediated
1234 modulation of cell helicity in *R. rubrum*. $BacA_{Rs}$ (yellow) recruits $LmdC_{Rs}$ (red) to the inner cell curvature.
1235 The hydrolytic activity of LmdC ultimately stimulates peptidoglycan biosynthesis at this position, leading
1236 to a reduction in cell helicity.

Figures

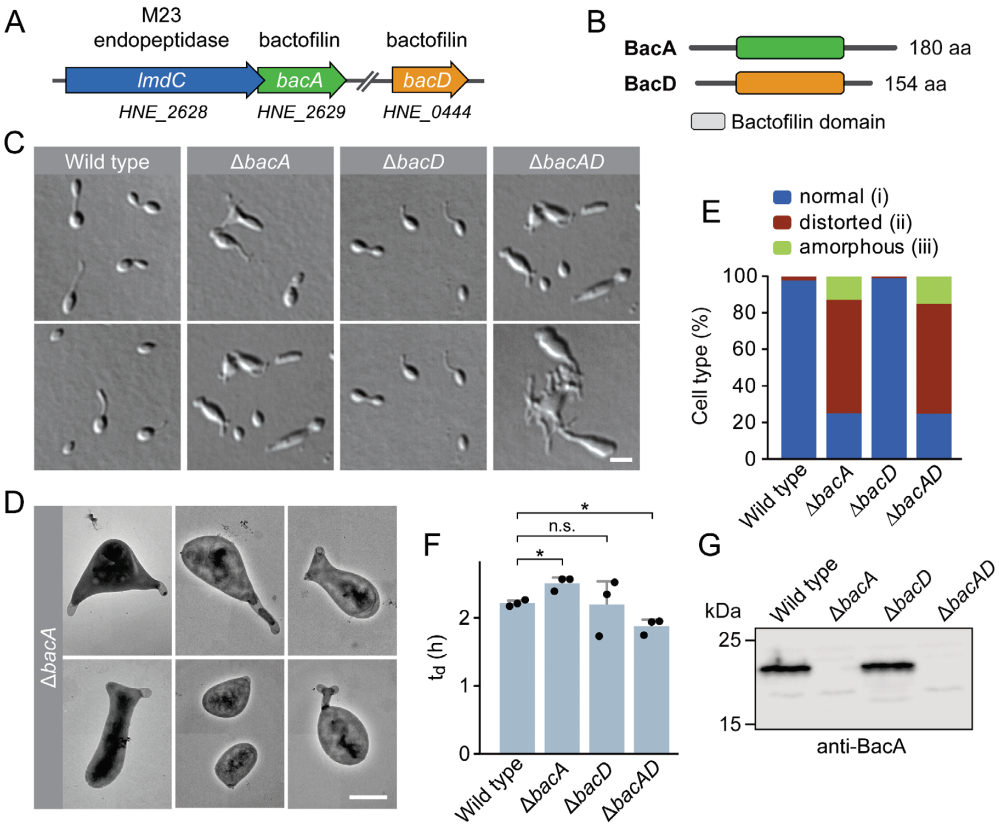

Figure 1. Bactofilin BacA is required for proper cell morphology in *H. neptunium*. (A) Schematic representation of the two bactofilin genes present in the *H. neptunium* genome. *bacA* lies adjacent to the M23 peptidase gene *lmdC*. Arrows indicate the direction of transcription. **(B)** Domain organization of BacA and BacD from *H. neptunium*. The bactofilin polymerization domain (colored boxes) is flanked by non-structured N- and C-terminal regions. **(C)** Morphology of *H. neptunium* bactofilin mutants. Shown are representative cells of strains LE670 (wild type), EC28 (Δ*bacA*), EC23 (Δ*bacD*) and EC33 (Δ*bacAD*), imaged by differential interference contrast (DIC) microscopy. Bar: 4 µm. **(D)** Transmission electron micrographs of Δ*bacA* cells at the early stalked-cell stage. Bar: 1 µm. **(E)** Quantification of the proportion of phenotypically abnormal stalked and budding cells in cultures of the strains analyzed in panel C (n = 100 cells per strain). **(F)** Doubling times of the indicated *H. neptunium* strains. Bars represent the mean (± SD) of three independent experiments (dots). Statistical significance was determined using Welch's non-paired t-test (*, $p<0.05$; n.s., not significant). **(G)** Immunoblot analysis of the strains shown in panel C, performed using anti-BacA antibodies.

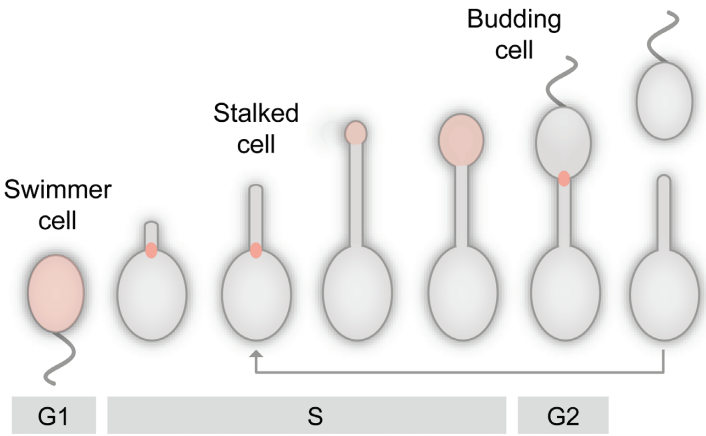

1247 **Figure 1—figure supplement 1. The dimorphic lifecycle of *H. neptunium*.** A motile, flagellated swimmer sheds its flagellum and
1248 forms a stalk at the opposite cell pole. At a defined point in the cell cycle, the terminal segment of the stalk dilates and develops
1249 into a new swimmer cell. After cell division, the newborn swimmer cell first needs to differentiate into a stalked cell to initiate a
1250 new round of cell division, whereas the stalked mother cell immediately enters the next replication cycle. The predominant
1251 growth zones (Cserti et al., 2017) are indicated in red.
1252

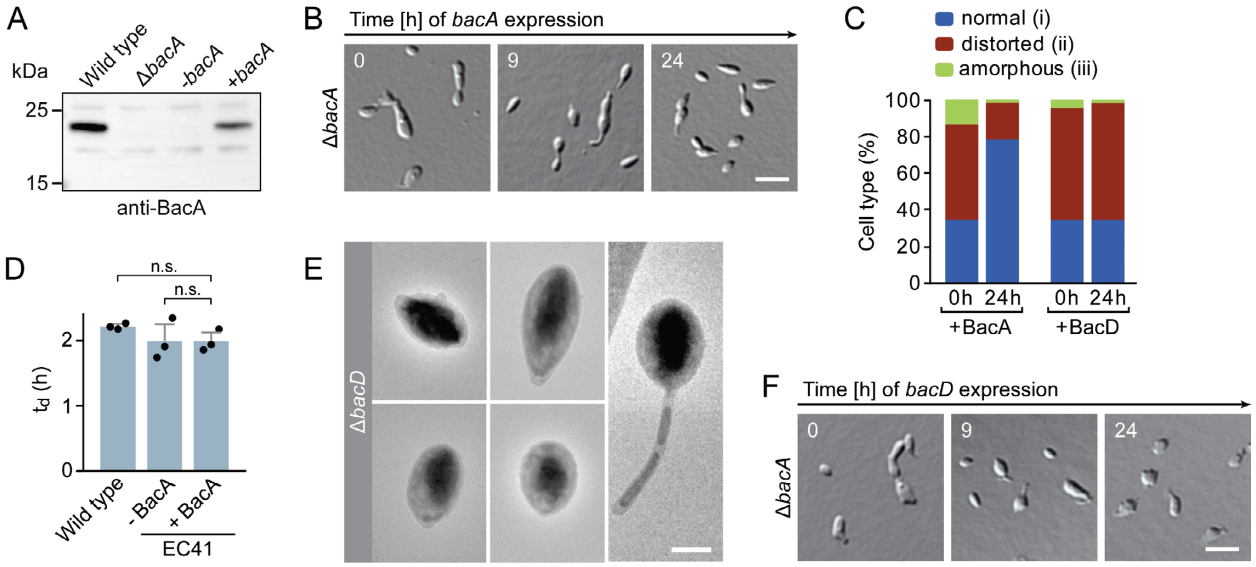

Figure 1—figure supplement 2. Phenotypic analysis of *H. neptunium* bactofilin mutants. (A) Immunoblot analysis of strains LE670 (wild type), EC28 (Δ*bacA*) and EC41 (Δ*bacA* P_{Cu}::P_{Cu}-*bacA*) grown in the absence (-*bacA*) and presence (+*bacA*) of 0.5 mM $CuSO_4$, performed with an anti-BacA antibody. **(B)** Rescue of the phenotype of a Δ*bacA* mutant by ectopic expression of *bacA*. Cells of strain EC41 (Δ*bacA* P_{Cu}::P_{Cu}-*bacA*) were grown in copper-free medium, induced by the addition of copper, and imaged after the indicated time incubation times. Bar: 3 µm. **(C)** Quantification of the proportion of phenotypically abnormal stalked and budding cells in the cultures of strains EC41 (Δ*bacA* P_{Cu}::P_{Cu}-*bacA*) and EC43 (Δ*bacA* P_{Zn}::P_{Zn}-*bacD*) analyzed in panels B and E before (t=0 h) and 24 h after induction (n = 100 cells per time point). **(D)** Doubling times of the indicated *H. neptunium* strains. Strain EC41 (Δ*bacA* P_{Cu}::P_{Cu}-*bacA*) as analyzed in the absence (-) and presence (+) of copper. Strain LE670 (wild-type) grown in copper-free medium is shown as a control. Bars represent the mean (± SD) of three independent experiments (dots). Statistical significance was determined using Welch's non-paired t-test (n.s., not significant). **(E)** Transmission electron micrographs of Δ*bacD* cells at the swimmer and stalk cell stage. Bar: 1 µm. **(F)** DIC images of a Δ*bacA* mutant overproducing BacD from a zinc-inducible promoter. Cells of strain EC43 (Δ*bacA* P_{Zn}::P_{Zn}-*bacD*) were grown in inducer-free medium, induced by the addition of 0.5 mM $ZnSO_4$, and imaged after the indicated incubation times. Bar: 3 µm.

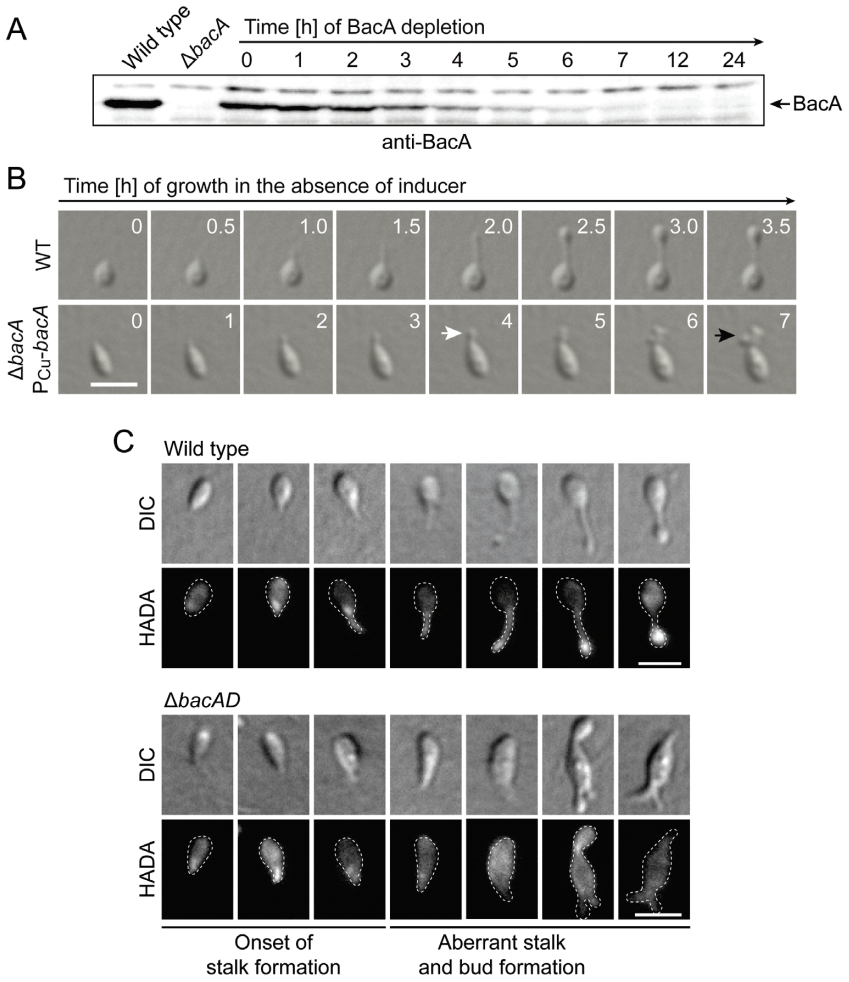

Figure 2. Lack of BacA leads to uncontrolled growth of the stalk and bud compartments. (A) Immunoblot showing the levels of BacA in strain EC41 (Δ*bacA* P_{Cu}-*bacA*) over the course of BacA depletion. Cells were grown in copper-containing medium, washed and transferred to inducer-free medium. At the indicated time points, samples were withdrawn and subjected to immunoblot analysis. Strains LE670 (wild type) and EC28 (Δ*bacA*) were included as controls. The position of BacA is indicated. **(B)** Morphological defects induced by BacA depletion. Cells of strains LE670 (wild type) and EC41 (Δ*bacA* P_{Cu}-*bacA*) were grown in medium containing 0.5 mM $CuSO_4$, washed, and incubated for 6 h in inducer-free medium before they were transferred onto ASS-agarose pads lacking inducer and imaged at the indicated time points. Bar: 2 µm. **(C)** Changes in the growth pattern of *H. neptunium* in the absence of bactofilins. Cells of strains LE670 (wild type) and EC33 (Δ*bacAD*) were stained with the fluorescent D-amino acid HADA prior to analysis by fluorescence microscopy. Shown are representative images of cells at different developmental stages. Bars: 2 µm.

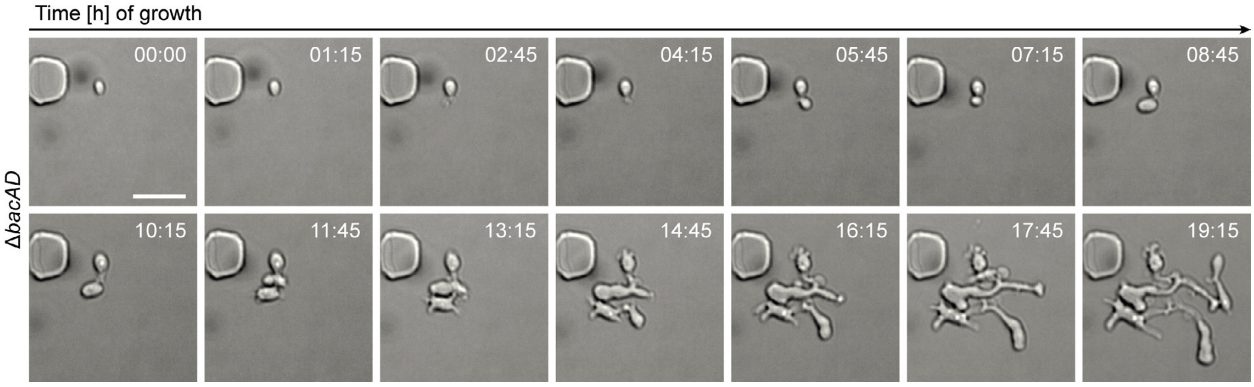

1276 **Figure 2—figure supplement 1. Growth of Δ*bacAD* cells in a microfluidic flow cell.** Cells of strain EC33 (Δ*bacAD*) were flushed
1277 into a microfluidic flow cell and imaged at the indicated time points (in h). Bar: 3 µm.

1278 **Figure 2—video 1. Unconstrained growth of a bactofilin-deficient *H. neptunium* mutant.** Cells of strain EC33 (Δ*badAD*) were
1279 grown in a microfluidic flow cell and imaged by DIC microsopy at 15 min intervals. Bar: 2 µm.

1280 **Figure 2—video 2. Normal growth of the *H. neptunium* wild-type strain.** Cells of strain LE670 (wild type) were grown in a
1281 microfluidic flow cell and imaged by DIC microscopy at 5 min intervals. Bar: 2 µm.

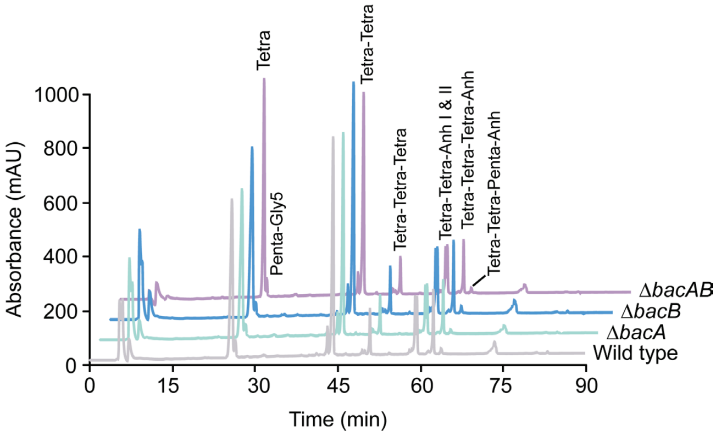

1282 **Figure 2—figure supplement 2. Muropeptide profiles of different *H. neptunium* strains.** Cell walls of strains LE670 (wild type),
1283 EC28 (Δ*bacA*), EC23 (Δ*bacD*) and EC33 (Δ*bacAD*) were digested with cellosyl to release muropeptides, which were reduced and
1284 separated by HPLC. The identities of major muropeptide species, assigned based on the previously reported retention times
1285 (Cserti et al., 2017; Glauner, 1988), are given above the corresponding peaks. Tri, Tetra and Penta stand for N-acetylglucosamine-
1286 N-acetylmuramitol tripeptide, tetrapeptide and pentapeptide, respectively. "Anh" indicates muropeptides containing 1,6-
1287 anhydromuramic acid.

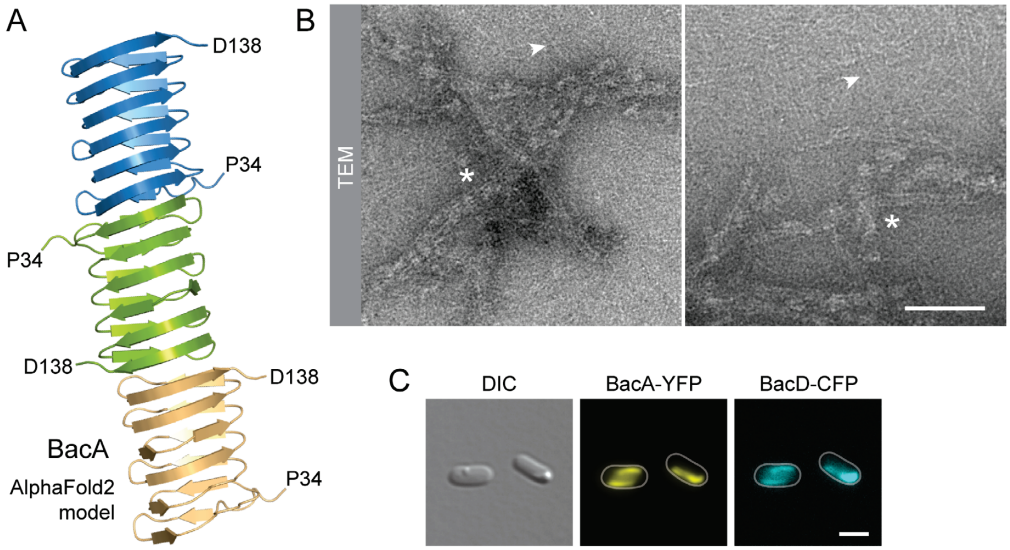

1288 **Figure 3. BacA and BacD co-polymerize into filamentous structures. (A)** Model of a BacA trimer generated with AlphaFold-
1289 Multimer (Evans et al., 2022). Only residues P34-D138 are shown for each subunit. **(B)** Visualization of BacA polymers. Purified
1290 BacA-His$_6$ was stained with uranyl acetate and imaged by transmission electron microscopy (TEM). Arrowheads point to BacA
1291 filaments. Asterisks indicate filament bundles and sheets. Bars: 200 nm. **(C)** Copolymerization of BacA and BacD after
1292 heterologous co-expression in *E. coli*. Cells of *E. coli* BL21(DE3) transformed with plasmid pEC121 (P_{T7}-*bacA-eyfp* P_{T7}-*bacD-ecfp*)
1293 were grown in LB medium containing 5 % glucose and induced with 0.5 mM IPTG prior to imaging. Bar: 3 µm.

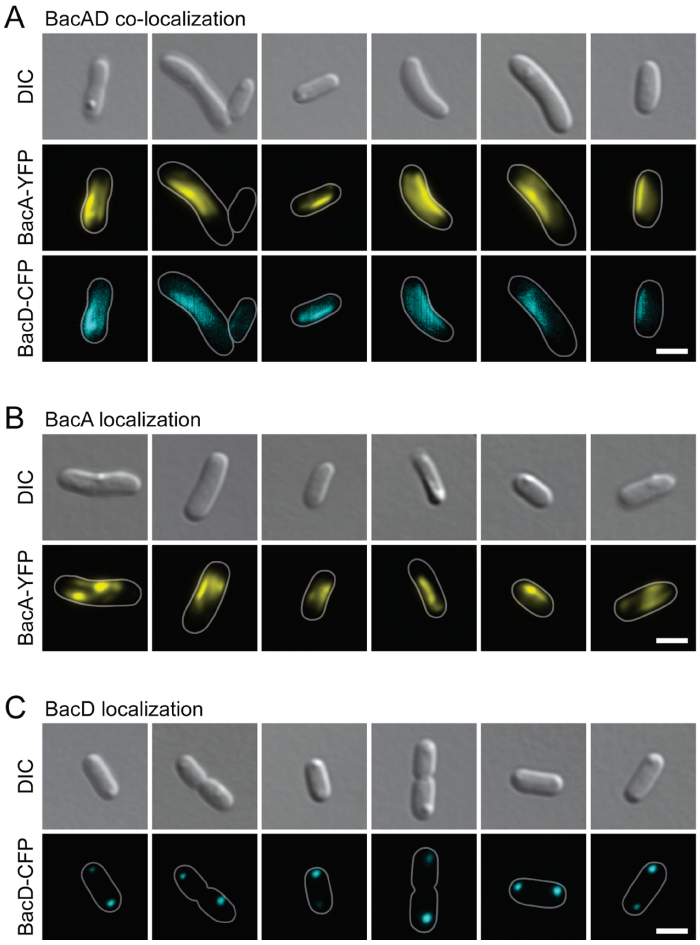

1294 **Figure 3—figure supplement 1.** Localization patterns of BacA-YFP and BacD-CFP upon heterologous overproduction in *E. coli*. **(A)**
1295 Co-localization of BacA-YFP and BacD-CFP in cells of *E. coli* BL21(DE3) transformed with plasmid pEC121 (P_{T7}-*bacA-eyfp* P_{T7}-*bacD-*
1296 *ecfp*). **(B)** Localization of BacA-YFP in cells of *E. coli* BL21(DE3) transformed with plasmid pEC119 (P_{T7}-*bacA-eyf*) **(C)** Localization of
1297 BacD-CFP in *E. coli* BL21(DE3) transformed with plasmid pEC120 (P_{T7}-$_{bacD-ecfp}$). All strains were grown in LB medium containing 5%
1298 glucose and induced with 0.5 mM IPTG prior to imaging. Bars: 2 µm.

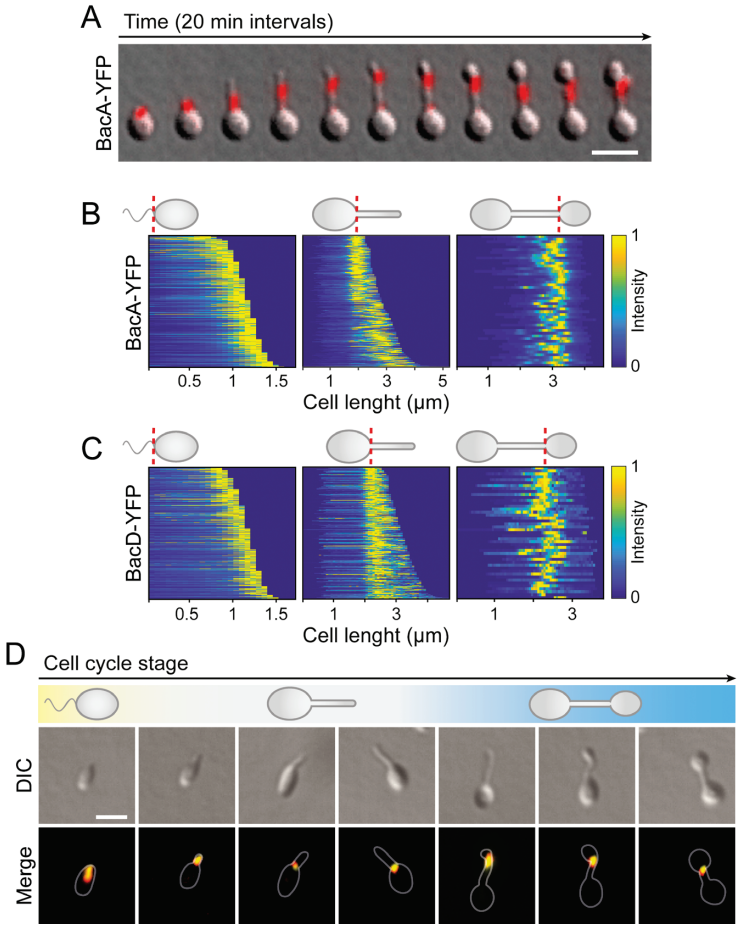

Figure 4. BacA and BacD show a dynamic, cell cycle-dependent localization pattern. (A) Localization pattern of BacA-YFP. Cells of strain EC61 (*bacA*::*bacA-eyfp*) were transferred to agarose pads and imaged at 20-min intervals. Shown are overlays of DIC and fluorescence images of a representative cell, with YFP fluorescence shown in red. Scale bar: 3 µm. **(B)** Demographic analysis of BacA-YFP localization in swimmer (left), stalked (middle), and budding (right) cells of strain EC61 (*bacA*::*bacA-eyfp*). The fluorescence intensity profiles measured for cells of each type were sorted according to cell length and stacked on each other, with the shortest cell shown at the top and the longest cell shown at the bottom (n=250 swimmer cells, 215 stalked cells and 49 budding cells). Dotted red lines indicate the positions to which cells were aligned. **(C)** Demographic analysis of BacD-Venus localization. Cells of strain EC67 (*bacD*::*bacD-venus*) were analyzed as described in panel B (n=416 swimmer cells, 248 stalked cells and 45 budding cells). **(D)** Co-localization of BacA and BacD in cells of strain EC68 (*bac*A::*bacA-eyfp bacD*::*bacD-mCherry*). Shown are DIC images and overlays of the YFP and mCherry signals of representative cells, arranged according to their developmental state. The individual signals are shown in **Figure S6A**. The Pearson's Correlation Coefficient (PCC) of the two fluorescence signals in a random population of cells (n=454) is 0.506. Bar: 1 µm.

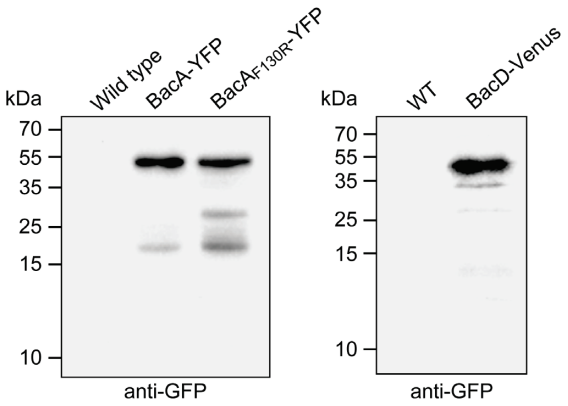

Figure 4—figure supplement 1. Stability of the fluorescently tagged bactofilin derivatives used in this study. Cells of strains LE670 (wild type), EC61 (*bacA*::*bacA-eyfp*), MO78 (*bacA*::*bacA*$_{F130R}$*-eyfp*) and EC67 (*bacD*::*bacD-venus*) were subjected to immunoblot analysis using anti-GFP antibodies.

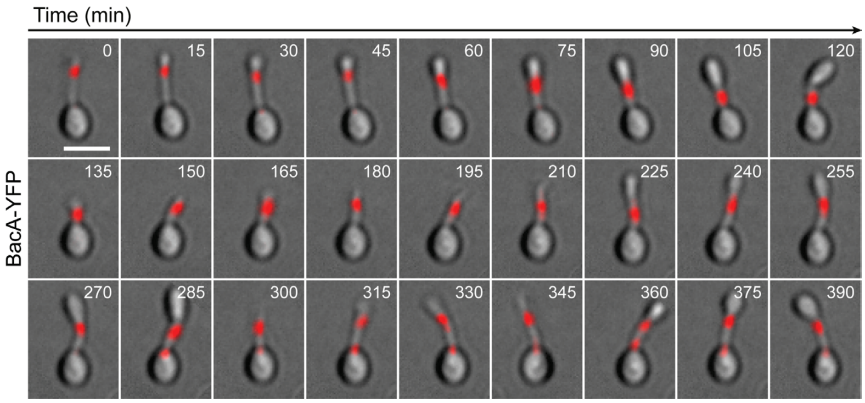

Figure 4—figure supplement 2. Localization dynamics of BacA-YFP. Cells of strain EC61 (*bacA*::*bacA-eyfp*) were flushed into a microfluidic flow cell and imaged at 15-min intervals over multiple cell cycles. Shown are overlays of DIC and fluorescence images. Bar: 2 µm.

Figure 4—video 1. Localization dynamics of BacA-YFP (example 1). Cells of strain EC61 (*bacA::bacA-eyfp*) were grown in a microfluidic flow cell and imaged at 15 min intervals. Shown are overlays of DIC and fluorescence images. YFP fluorescence is shown in red for better visibility. Bar: 2 µm.

Figure 4—video 2. Localization dynamics of BacA-YFP (example 2). Cells of strain EC61 (*bacA::bacA-eyfp*) were grown in a microfluidic flow cell and imaged at 15 min intervals. Shown are overlays of DIC and fluorescence images. YFP fluorescence is shown in red for better visibility. Bar: 2 µm.

Figure 4—video 3. Localization dynamics of BacA-YFP (example 3). Cells of strain EC61 (*bacA::bacA-eyfp*) were grown in a microfluidic flow cell and imaged at 15 min intervals. Shown are overlays of DIC and fluorescence images. YFP fluorescence is shown in red for better visibility. Bar: 2 µm.

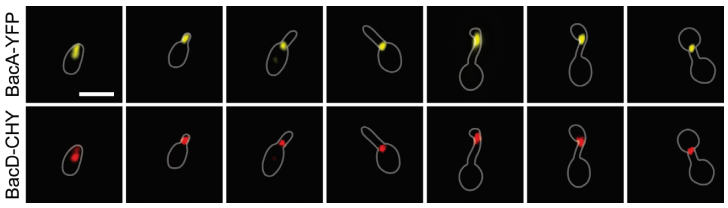

1326 **Figure 4—figure supplement 3. Co-localization of BacA and BacD.** Shown are the individual fluorescence images of strain EC68
1327 (*bac*A::*bacA-eyfp bacD*::*bacD-mCherry*) used to generate the overlays in **Figure 4D**. Bar: 1 µm.

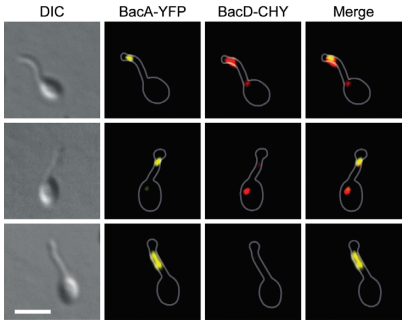

1328 **Figure 4—figure supplement 4. Partial independence of BacA and BacD localization at the onset of the budding process.** Shown
1329 are exemplary cells of strain EC68 (*bacA*::*bacA-eyfp bacD*::*bacD-mCherry*) in which BacA-YFP and BacD-CHY do not fully co-
1330 localize. Bar: 2 µm.

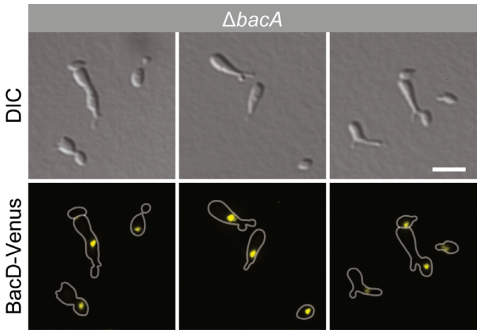

1331 **Figure 4—figure supplement 5. Random localization of BacD complexes in the absence of BacA.** Cells of strain EC60 (Δ*bacA*
1332 P_{Zn}::P_{Zn}-*bacD-venus*) were grown in inducer-free medium and then induced for 4 h with 0.5 mM $ZnSO_4$ prior to imaging. Bar: 3 µm.

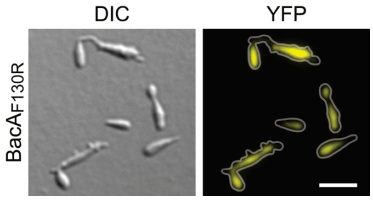

1333 **Figure 4—figure supplement 6. Localization and functionality of $BacA_{F130R}$-YFP.** Cells of strain MO78 (*bacA*::*$bacA_{F130R}$-eyfp*),
1334 producing the polymerization-deficient $BacA_{F130R}$-YFP variant instead of the native protein, were grown to exponential phase and
1335 imaged. Bar: 3 µm.
1336

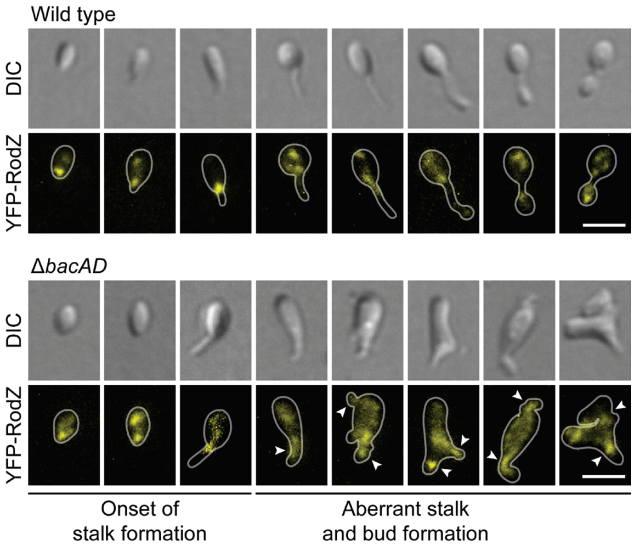

1337 **Figure 5. The bactofilin cytoskeleton is required to confine the elongasome to the mother cell and bud compartments.**
1338 Localization of eYFP-RodZ in the *H. neptunium* wild-type and Δ*bacAD* backgrounds. Shown are representative cells of strain EC93
1339 (*rodZ*::*eyfp-rodZ*) and SP221 (Δ*bacAD rodZ*::*eyfp-rodZ*) imaged by DIC and fluorescence microscopy and arranged according to
1340 their developmental state. Arrowheads indicate cellular extensions that show eYFP-RodZ foci. Bar: 2 µm.

1341 **Figure 5—video 1. Localization of YFP-RodZ during stalk synthesis in the wild-type background.** Cells of strain EC93 (*rodZ*::*eyfp-*
1342 *rodZ*) were immobilized on pads made of 1% agarose in ASS medium and imaged at 2 min intervals. Bar: 2 µm.

1343 **Figure 5—video 2. Localization of YFP-RodZ during bud formation in the wild-type background.** Cells of strain EC93 (*rodZ*::*eyfp-*
1344 *rodZ*) were immobilized on pads made of 1% agarose in ASS medium and imaged at 2 min intervals. Bar: 2 µm.

1345 **Figure 5—video 3. Localization of YFP-RodZ during pseudo stalk synthesis in the Δ*bacAD* background.** Cells of strain SP221
1346 (Δ*bacAD rodZ*::*eyfp-rodZ*) were immobilized on pads made of 1% agarose in ASS medium and imaged at 2 min intervals. Bar: 2
1347 µm.

1348 **Figure 5—video 4. Localization of YFP-RodZ within within early stalks in the Δ*bacAD* background.** Cells of strain SP221 (Δ*bacAD*
1349 *rodZ*::*eyfp-rodZ*) were immobilized on pads made of 1% agarose in ASS medium and imaged at 2 min intervals. Bar: 2 µm.

1350 **Figure 5—video 5. Localization of YFP-RodZ in amorphous cells in the Δ*bacAD* background.** Cells of strain SP221 (Δ*bacAD*
1351 *rodZ*::*eyfp-rodZ*) were immobilized on pads made of 1% agarose in ASS medium and imaged at 2 min intervals. Bar: 2 µm.

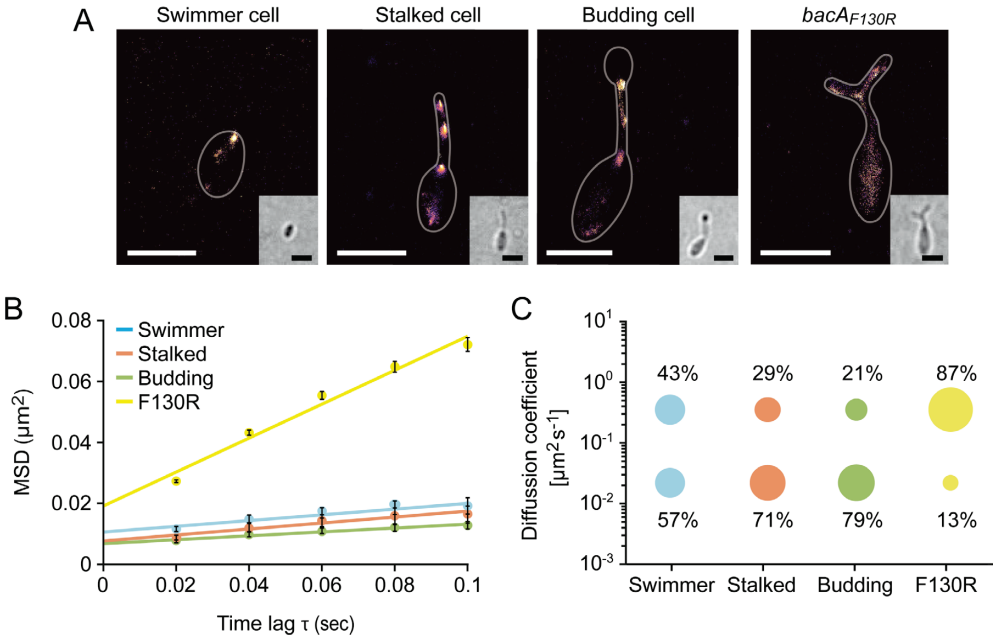

Figure 6. The single-particle dynamics of BacA change over the course of the cell cycle. (A) Representative heat maps showing the sum of single-particle positions observed in live-cell single-particle localization microscopy studies of a swimmer, stalked and budding cell producing BacA-YFP (EC61) or a mutant cell producing the polymerization-deficient $BacA_{F130R}$-YFP variant (MO78). Insets show the corresponding bright-field images. Bars: 1 µm. **(B)** Mean-squared displacement (MSD) analysis of the mobility of BacA-YFP in wild-type swimmer (n=100), stalked (n=105) and budding (n=101) cells (EC61). Cells (n=110) producing the $BacA_{F130R}$-YFP were analyzed as a control (MO78). Error bars indicate the standard deviation. **(C)** Bubble plots showing the proportions of mobile and immobile particles (size of the bubbles) and the corresponding average diffusion constants (y-axis) in the cells analyzed in panel B.

Figure 6—video 1. Tracking of single BacA-YFP particles in representative cells at different stages of the cell cycle. Shown are stream acquisitions (20-ms intervals) of *H. neptunium* cells producing wild-type BacA-YFP (EC61) or the polymerization-deficient $BacA_{F130R}$-YFP variant (MO78) in place of the native BacA protein at different developmental stages. Bar: 1 µm

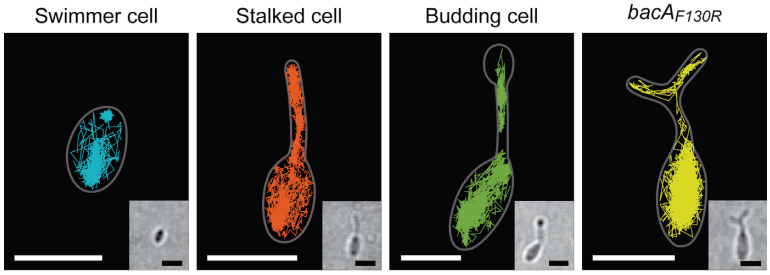

Figure 6—figure supplement 1. Single-particle tracking analysis of BacA-YFP. The images show the sums of all single-molecule tracks obtained for individual *H. neptunium* swimmer, stalked and budding cell producing BacA-YFP (EC61) or for a mutant cell producing the polymerization-deficient $BacA_{F130R}$-YFP variant (MO78). Cell outlines are indicated by white lines. Inserts show the corresponding bright-field images. Bars: 1 µm.

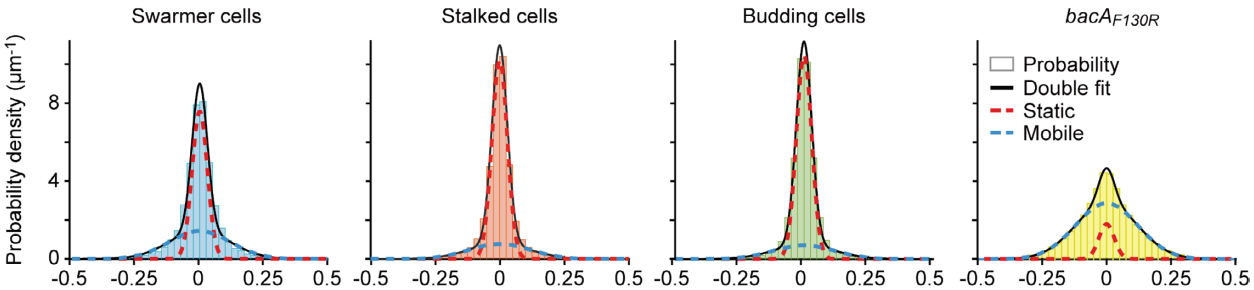

Figure 6—figure supplement 2. Single-particle tracking analysis of BacA-YFP mobility. Shown is a Gaussian mixture model (GMM) analysis of the mobility of the BacA-YFP variants plotted in **Figure 5C**. The distributions of the frame-to-frame displacements in both x and y direction from single-particle tracking experiments were fitted to a two-component Gaussian function (sum in black), assuming a fast-diffusing mobile (dotted blue lines) and a slow-diffusing (dotted red lines) population.

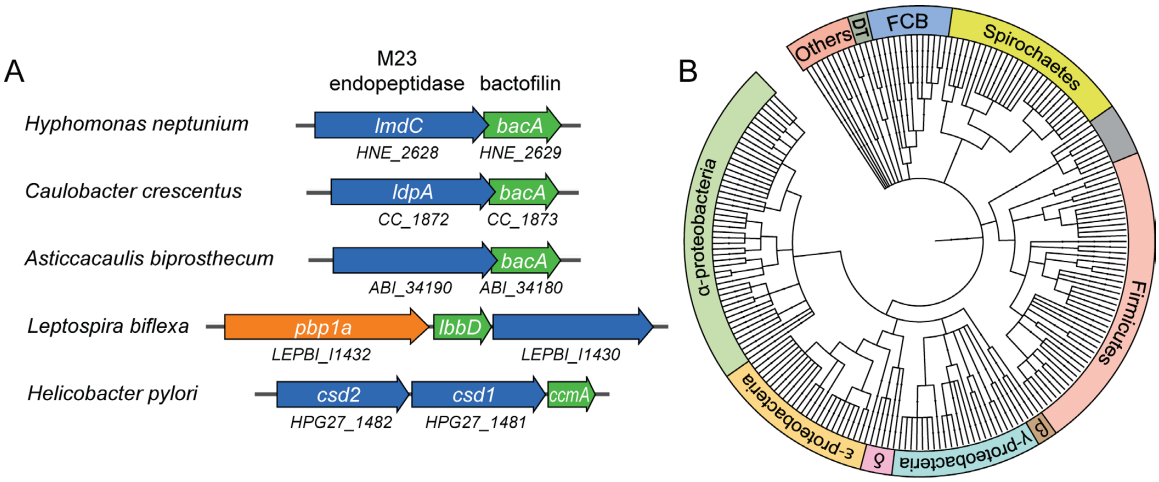

Figure 7. Putative operons comprising adjacent BacA and M23 peptidase genes are widely conserved among bacteria. (A) Arrangement of *bacA* and *lmdC* genes in species whose BacA homolog has a proven role in cell morphogenesis. **(B)** Co-conservation of BacA and M23 peptidase genes across different bacterial phyla. Bioinformatic analysis was used to identify genomes that contained a bactofilin gene located next to an M23 peptidase gene. After retrieval of the taxonomy IDs of the corresponding species from the National Center for Biotechnology Information (NCBI) website, a phylogenetic tree of the species was created using the iTOL server (Letunic and Bork, 2021). Abbreviations: DT (Deinococcus-Thermus group), FCB (Fibrobacteres-Chlorobi-Bacteroidetes group), β (β-proteobacteria), δ (δ-proteobacteria). The full list of species used and details on the genes identified are provided in **Figure 7—Dataset 1**.

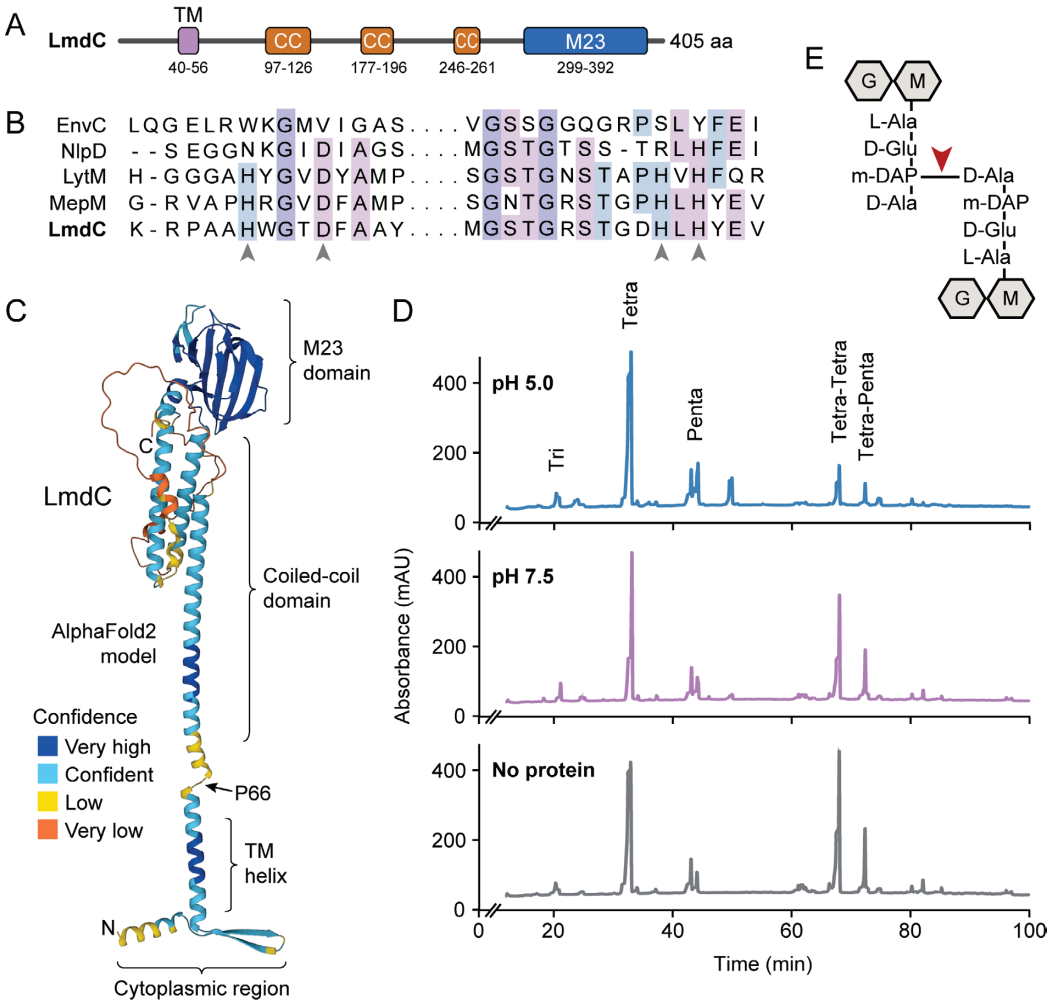

Figure 8. LmdC is a peptidoglycan hydrolase with DD-endopeptidase activity. (A) Predicted domain architecture of *H. neptunium* LmdC. The predicted positions of the transmembrane helix (TM), the three coiled-coil regions (CC) and the M23 peptidase domain are indicated. **(B)** Alignment of the amino acid sequences of multiple M23 peptidases showing the conservation of the catalytic residues in LmdC. Residues required to coordinate the catalytic Zn^{2+} ion of LytM from *S. aureus* (Firczuk et al., 2005) are indicated by arrowheads. The proteins shown are EnvC from *E. coli* (UniProt: P37690), NlpD from *E. coli* (P0ADA3), LytM from *S. aureus* (O33599), MepM from *E. coli* (P0AFS9) and LmdC from *H. neptunium* (Q0BYX6). **(C)** Predicted molecular structure of *H. neptunium* LmdC, generated with Alphafold2 (Jumper et al., 2021). The different domains of the protein and the position of proline 66, which terminates the N-terminal fragment of LmdC used for the *in vivo* analyses in this study ($LmdC_{1-66}$) are indicated. **(D)** HPLC traces showing the muropeptide profile of peptidoglycan treated with LmdC. Cell walls were incubated with the isolated M23 peptidase domain of LmdC at pH 5.0 and pH 7.5. Subsequently, muropeptides were released with cellosyl, reduced and separated by HPLC. A control sample lacked LmdC (No protein). The nature of the major products is indicated above the peaks. Tri, Tetra and Penta stand for N-acetylglucosamine-N-acetylmuramitol tripeptide, tetrapeptide and pentapeptide, respectively. **(E)** Structure of a TetraTetra muropeptide. Abbreviations: G (N-acetylglucosamine), M (N-acetylmuramic acid). The cleavage site of LmdC is indicated by a red arrowhead.

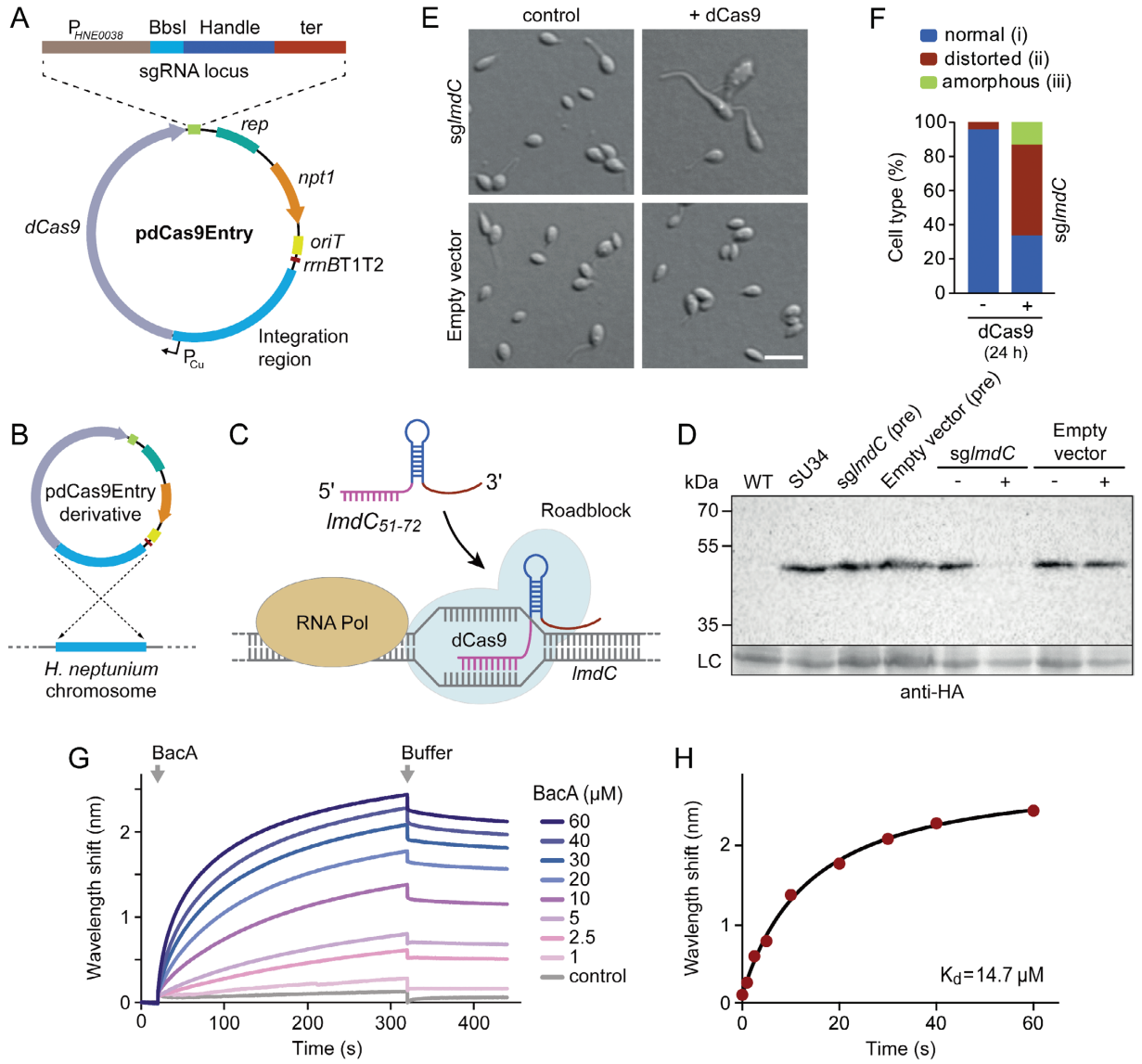

Figure 9. LmdC interacts with BacA to mediate *H. neptunium* morphogenesis. (A) Schematic representation of the integrative plasmid pdCas9Entry, enabling CRISPR interference (CRISPRi) in *H. neptunium*. The plasmid harbors a chromosomal fragment containing the copper-inducible P_{Cu} promoter, followed by a gene encoding a nuclease-deficient variant of Cas9 (dCas9). It also contains an sgRNA expression cassette composed of the constitutive $P_{HNE0038}$ promoter, a BbsI cloning site for the insertion of target-specific DNA fragments, a sequence encoding the sgRNA handle and a transcriptional terminator (ter). Other features of the plasmid are a replication initiator gene (*rep*), a kanamycin resistance gene (*npt1*), an origin of transfer (*oriT*) and a strong transcriptional terminator (*rrnB*T1T2) that is placed upstream of the P_{Cu}-containing fragment. The DNA sequence of the sgRNA expression cassette is given in **Figure 9–figure supplement 1**. **(B)** Schematic showing the integration of a pdCas9Entry derivative into the *H. neptunium* chromosome by single homologous recombination at the P_{Cu} locus. **(C)** Mechanism of the CRISPRi-mediated repression of *lmdC* expression. In the presence of inducer, dCas9 interacts with a constitutively produced sgRNA that targets bases 51-72 of the non-coding strand of *lmdC* (sg*lmdC*). The formation of the interference complex creates a roadblock that blocks the transcription of *lmdC* by RNA polymerase. **(D)** Immunoblot analysis verifying the CRISPRi-mediated depletion of LmdC. Strain SU34 (*lmdC*::*lmdC-HA*), which produces a fully functional variant of LmdC carrying the HA affinity tag inserted in between the transmembrane helix and the coiled-coil domain, was transformed with pdCas9Entry (empty vector) or plasmid pJH13 (sg*lmdC*). The resulting strains (SP249 and SP236) were grown for 24 h in the absence (-) or presence (-) of 0.3 mM $CuSO_4$ and subjected to immunoblot analysis with an anti-HA antibody. The wild-type strain (LE670), the parental strain SU34 as well as the uninduced pre-cultures (pre) of strains SP249 and SP236 used for the experiment were analyzed as controls. A non-specific band served as

a loading control (LC). **(E)** Morphology of *H. neptunium* cells depleted of LmdC. Shown are representative cells of strains SP236 (*lmdC*::*lmdC*-HA pJH13) (sg*lmdC*) and SP249 (*lmdC*::*lmdC*-HA pCas9Entry) (empty vector) grown for 24 h in the absence (control) or presence (+ dCas9) of 0.3 mM $CuSO_4$. Cells were imaged by DIC and fluorescence microscopy. Bar: 2 µm. **(F)** Quantification of the proportion of phenotypically abnormal stalked and budding cells in the cultures of strain SP236 (*lmdC*::*lmdC*-HA pJH13) analyzed in panel E (n=100 cells per condition). **(G)** Bio-layer interferometric analysis of the interaction between cytoplasmic domain of LmdC and BacA. Sensors derivatized with a biotinylated synthetic peptide comprising the N-terminal cytoplasmic region of LmdC (amino acids 1-38) were probed with the indicated concentrations of BacA. After the association of BacA, the sensors were transferred to protein-free buffer to induce BacA dissociation. The interaction kinetics were followed by monitoring the wavelength shifts resulting from changes in the optical thickness of the sensor surface during association or dissociation of the analyte. The extent of non-specific binding of BacA to the sensor surface was negligible (control). **(H)** Affinity of the BacA-LmdC interaction. The maximal wavelength shifts measured in the experiment shown in panel D were plotted against the corresponding BacA concentration. The data were fitted to a one-site binding model, yielding an apparent K_d value of ~15 µM.

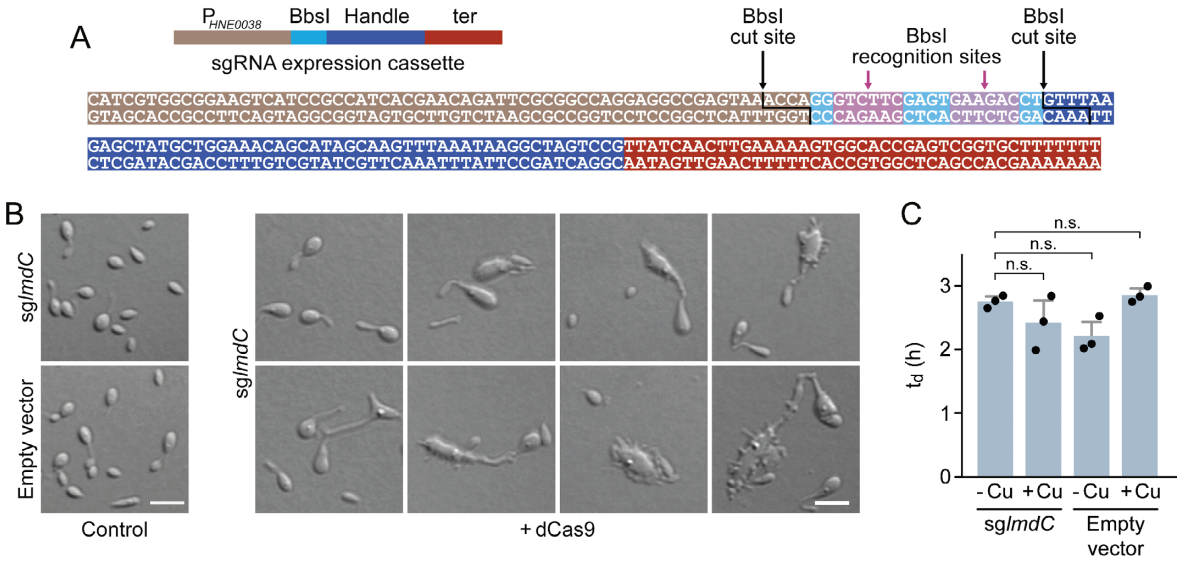

Figure 9—figure supplement 1. Characterization of the phenotype induced by the CRISPRi-mediated depletion of LmdC in *H. neptunium*. (A) Sequence of the sgRNA expression cassette of pdCas9Entry. The different parts of the sequence are colored as defined in the schematic on top. The BsbI recognition and cut sites are indicated by arrows. **(B)** Morphological diversity of *H. neptunium* cells depleted of LmdC. Shown are representative cells of strains SP236 (*lmdC*::*lmdC*-HA pJH13) (sg*lmdC*) and SP249 (*lmdC*::*lmdC*-HA pCas9Entry) (empty vector) grown for 24 h in the absence (control) or presence (+ dCas9) of 0.3 mM $CuSO_4$. Cells were imaged by DIC microscopy. Bar: 2 µm. **(C)** Doubling times of the strains analyzed in panel B in the absence (-Cu) or presence (+Cu) of 0.3 mM $CuSO_4$. Bars represent the mean (± SD) of three independent experiments (dots). Statistical significance was determined using Welch's non-paired t-test (n.s., not significant).

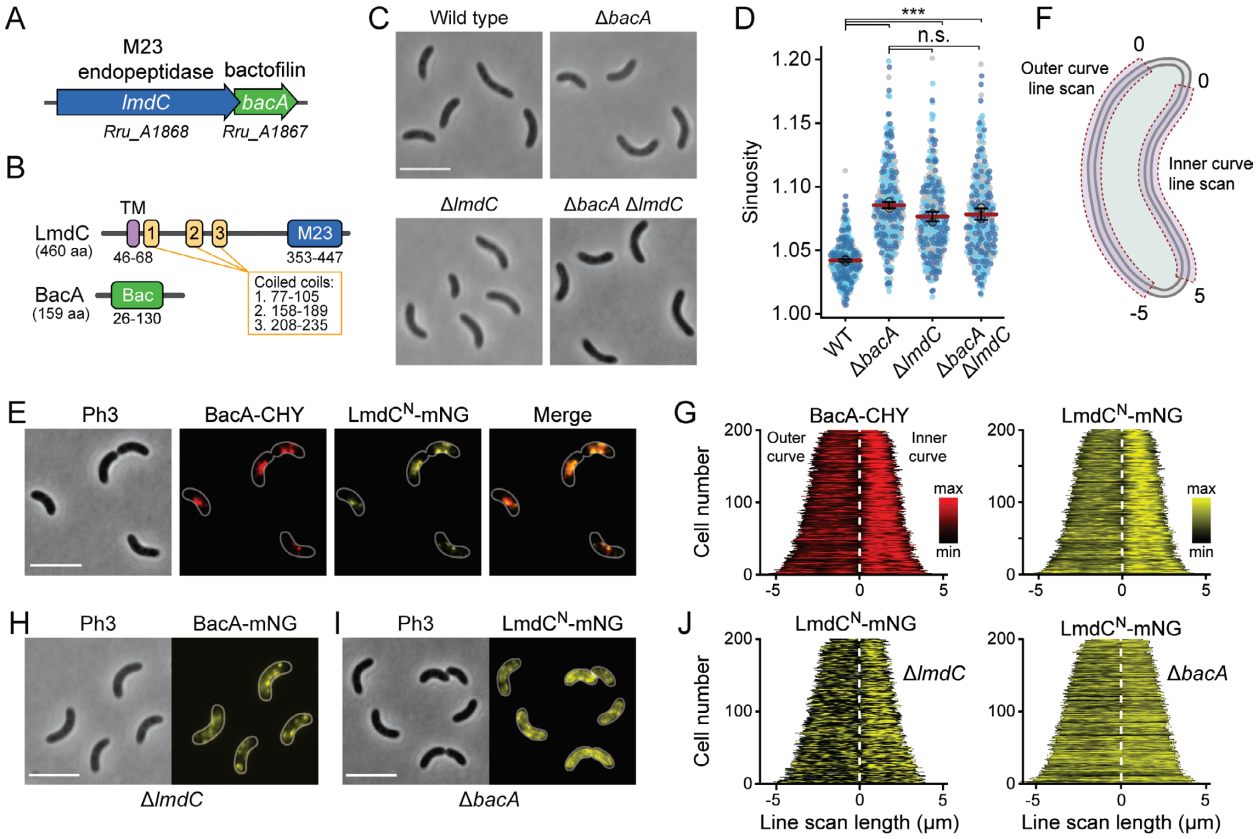

Figure 10. BacA and LmdC contribute to cell morphogenesis in *R. rubrum*. (A) Schematic representation of the *bacA-lmdC* operon in *R. rubrum*. **(B)** Domain organization of LmdC and BacA from *R. rubrum*. LmdC consists of a transmembrane helix (TM) followed by a coiled-coil-rich region and a C-terminal M23 peptidase domain (M23). The bactofilin polymerization domain (green box) is flanked by non-structured N- and C-terminal regions. Numbers indicate the first and last amino acid of a domain. **(C)** Phenotypes of *R. rubrum* wild-type (S1), Δ$bacA_{Rs}$ (SP70), Δ$lmdC_{Rs}$ (SP68) and Δ$bacA_{Rs}$ Δ$lmdC_{Rs}$ (SP116) cells, imaged using phase-contrast microscopy. Bar: 5 µm. **(D)** Superplots showing the distribution of cell sinuosities in populations of the indicated *R. rubrum* strains. Small dots represent the data points, large dots represent the median values of the three independent experiments shown in the graphs (dark blue, light blue, grey). The mean of the three median values is indicated by a horizontal red line. Whiskers represent the standard deviation. *** $p<0.005$; ns, not significant; t-test). **(E)** Co-localization of $BacA_{Rs}$-CHY and $LmdC^N_{Rs}$-mNG in the Δ$lmdC_{Rs}$ background (SP119). The Pearson's Correlation Coefficient (PCC) of the two fluorescence signals in a random subpopulation of cells is 0.916. Scale bar: 5 µm. **(F)** Schematic showing the approach used to quantify the distribution of proteins along the outer and inner curve of a cell in panel G. **(G)** Demographs showing the enrichment of BacA-CYH and $LmdC^N$-mNG at the inner curve the populations of strain SP119 analyzed in panel E (n=200 per strain). The white dashed line represents the point of transition from the outer to the inner curve. **(H)** Localization of $BacA_{Rs}$-mNG in the Δ$lmdC_{Rs}$ background (SP98). Bar: 5 µm. **(I)** Localization of $LmdC_{Rs}$-mNG in the Δ$bacA_{Rs}$ background (SP118). Bar: 5 µm. **(J)** Demographs showing the outer-versus-inner curve distribution of $BacA_{Rs}$-mNG in the Δ$lmdC_{Rs}$ background (SP98; n=200) and $LmdC^N_{Rs}$-mNG in the Δ$bacA_{Rs}$ background (SP118; n=200). The white dashed line represents the point of transition from the outer to the inner curve.

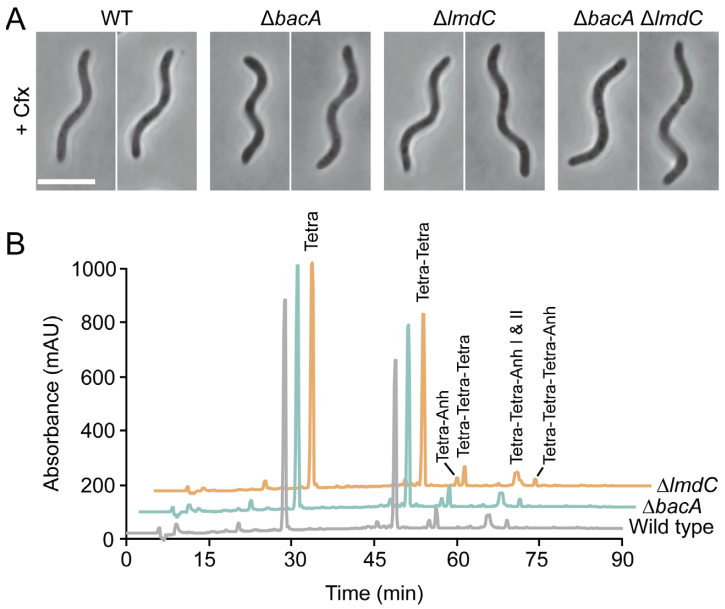

1447 **Figure 10—figure supplement 1. Analysis of BacA and LmdC from *R. rubrum*. (A)** Clearer visualization of the abnormal curvature
1448 of BacA- and LmdC-deficient *R. rubrum* cells by inhibition of cell division. Cells of strains SP68 (Δ*lmdC*), SP70 (Δ*bacA*) and SP116
1449 (Δ*lmdC* Δ*bacA*) were treated with 5 µg/ml cefalexin (Cfx) for 6 h. Bar: 5 µm. **(B)** Muropeptide profiles of different *R. rubrum*
1450 strains. Cell walls of strains S1 (wild type), SP70 (Δ$bacA_{Rs}$) and SP68 (Δ*lmdC*) were digested with cellosyl to release muropeptides,
1451 which were reduced and separated by HPLC chromatography. The identities of major muropeptide species, assigned based on
1452 the previously reported retention times (Glauner, 1988), are given above the corresponding peaks. Tetra stands for N-acetyl-
1453 glucosamine-N-acetylmuramitol tetrapeptide. "Anh" indicates muropeptides containing 1,6-anhydromuramic acid.

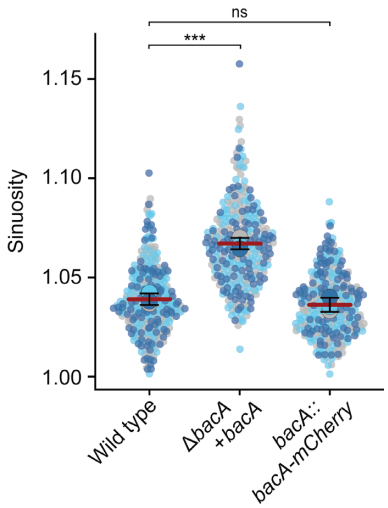

1454 **Figure 10—figure supplement 2. Cell lengths of *R. rubrum* strains.** Superplots showing the distribution of cell sinuosities in popu-
1455 lations of strains S1 (wild type), SP105 (Δ$bacA_{Rs}$ P_{bacA}-$bacA_{Rs}$) and SP109 ($bacA_{Rs}$::$bacA_{Rs}$-*mCherry*). Small dots represent the data
1456 points, large dots represent the median values of the three independent experiments shown in the graphs (dark blue, light blue,
1457 grey). The mean of the three median values is indicated by a horizontal line. Whiskers represent the standard deviation. ***
1458 p<0.005; ns, not significant; t-test).

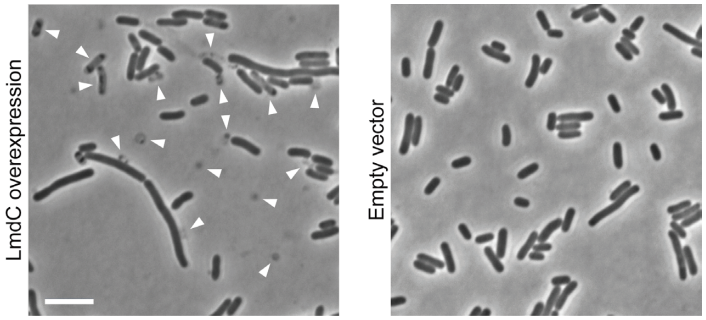

Figure 10—figure supplement 3. Lysis of *E. coli* upon heterologous expression of full-length *R. rubrum lmdC*. Shown are cells of *E. coli* Rosetta(DE3)pLysS harboring pSP120 (P_{T7}-$lmdC_{Rs}$) or the corresponding empty vector imaged 4h after the induction of gene expression with 0.5 mM IPTG. Arrowheads indicate ghost cells, cell debris, lysing cells or strongly elongated cells. Scale bar: 5 µm.

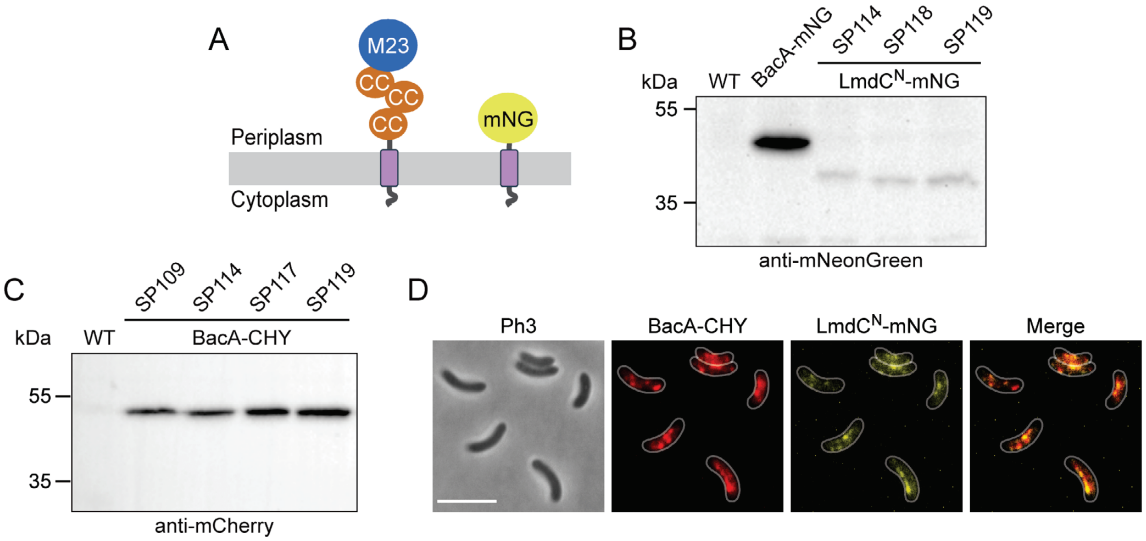

Figure 10—figure supplement 4. Analysis of *R. rubrum* strains producing fluorescent protein fusions. (A) Domain architectures of the native $LmdC_{Rs}$ protein and the truncated $LmdC^{N}_{Rs}$-mNG reporter construct used for localization studies. The transmembrane helix is shown in purple. Abbreviations: CC (coiled-coil domain), M23 (M23 peptidase domain), mNG (mNeongreen). **(B)** Levels of the $LmdC^{N}_{Rs}$-mNG fusion in different *R. rubrum* strains. Strains SP98 (Δ$lmdC_{Rs}$ $bacA_{Rs}$::$bacA_{Rs}$-*mNeongreen*), SP114 ($bacA_{Rs}$::$bacA_{Rs}$-*mCherry* P_{lmdC}-$lmdC^{N}_{Rs}$-*mNeongreen*), SP118 (Δ*bacA* Δ*lmdC* P_{lmdC}-$lmdC_{1\text{-}80}$-*mNeongreen*) and SP119 (*bacA*::*bacA*-*mCherry* Δ*lmdC* P_{lmdC}-$lmdC_{1\text{-}80}$-*mNeongreen*) were subjected to immunoblot analysis with an anti-mNeonGreen antibody. Predicted molecular weights: $BacA_{Rs}$-mNG (44.8 kDa), $LmdC^{N}_{Rs}$-mNG fusion (35.9 kDa) **(C)** Levels of the $BacA_{Rs}$-CHY fusion in different *R. rubrum* strains. Strains SP109 ($bacA_{Rs}$::$bacA_{Rs}$-*mCherry*), SP114 ($bacA_{Rs}$::$bacA_{Rs}$-*mCherry* P_{lmdC}-$lmdC^{N}_{Rs}$-*mNeongreen*), SP117 ($bacA_{Rs}$::$bacA_{Rs}$-*mCherry* Δ*lmdC*) and SP119 ($bacA_{Rs}$::$bacA_{Rs}$-*mCherry* Δ*lmdC* P_{lmdC}-$lmdC^{N}_{Rs}$-*mNeongreen*) were subjected to immunoblot analysis with an anti-mCherry antibody. The predicted molecular weight of $BacA_{Rs}$-CHY is 44.9 kDa. **(D)** Co-localization of $BacA_{Rs}$-CHY and $LmdC_{Rs}$-mNG in *R. rubrum* cells carrying the native $lmdC_{Rs}$ gene. The Pearson's Correlation Coefficient (PCC) of the two fluorescence signals in a random subpopulation of cells (n=177) is 0.54. Scale bar: 5 µm.

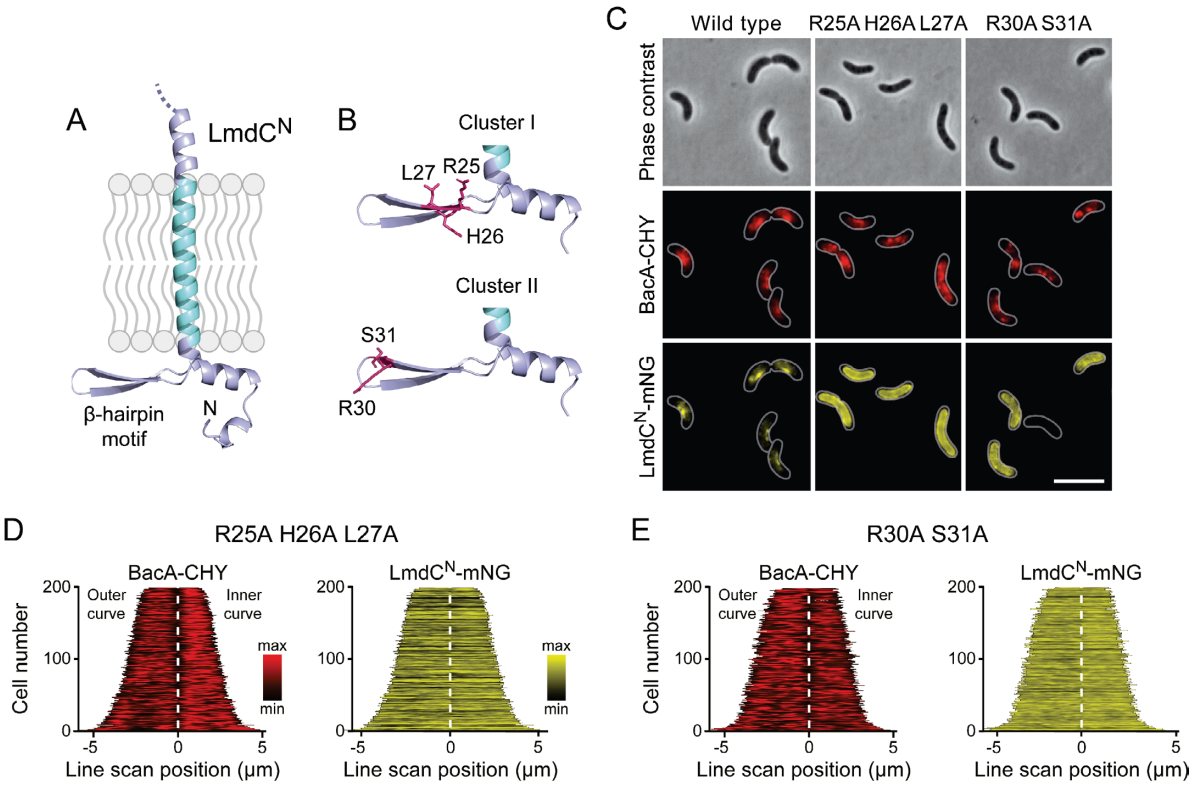

Figure 11. The β-hairpin in the cytoplasmic region of LmdC is critical for BacA binding. (A) Predicted structure of $LmdC^N$, comprising the first 80 amino acids of LmdC. The transmembrane domain is colored light blue. The cytoplasmic domain includes a conserved β-hairpin motif. **(B)** Clusters of amino acids mutated for the analysis of BacA-LmdC interaction. Mutated amino acids are shown as red sticks. **(C)** Localization of $BacA_{Rs}$-CHY and the indicated $LmdC^N_{Rs}$-mNG variants in the Δ$lmdC_{Rs}$ background. The Pearson's Correlation Coefficient (PCC) of the two fluorescence signals in a random subpopulation of cells is 0.914 for the wild type fusion (SP119), 0.887 for the R25A-H26A-L27A variant (SP237) and 0.827 for the R30A S31A variant (SP238). Scale bar: 5 µm. **(D,E)** Demographs showing the distribution of BacA-mCherry and (D) R25A-H26A-L27A variant (SP237) or R31A-S31A variant (SP238) of $LmdC^N$-mNG along the outer and inner curve of the cell (n=200 per strain). The white line marks the point of transition from the outer and the inner curve. The analysis was performed as described in **Figure 10F**.

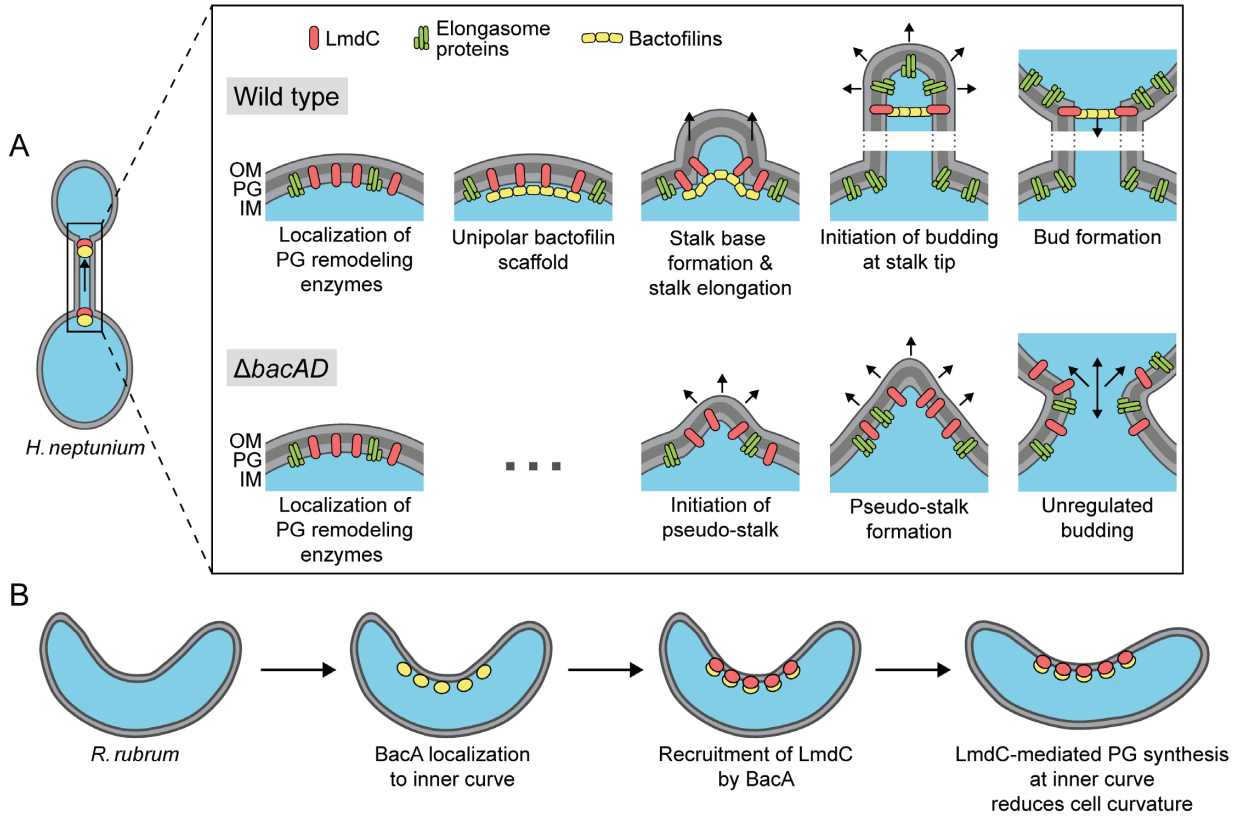

Figure 12. Model of the roles of BacA and LmdC in *H. neptunium* and *R. rubrum* cell morphogenesis. (A) Cell morphogenesis in *H. neptunium* wild-type (top) and Δ*bacAD* cells (bottom). In wild-type cells, BacA polymers form a complex with the DD-endopeptidase LmdC at the future stalked pole. The hydrolytic activity of LmdC, possibly stimulated by its interaction with BacA, helps to curve the cell wall at the incipient stalk base and thus determine stalk morphology. The zone of high positive inner cell curvature and, potentially, the physical barrier constituted by the bactofilin polymer prevent the movement of elongasome complexes from the mother cell body into the stalk, thereby limiting peptidoglycan biosynthesis to the stalked cell pole. At a later stage, the bactofilin-LmdC complex localizes close to the tip of the stalk and again generates a ring-shaped zone of positive cell curvature, thereby promoting the remodeling of the stalk tip into a spherical bud. At the onset of the budding process, elongasome complexes accumulate in the nascent bud by a so-far unknown mechanism. The positively curved bud neck and the bactofilin polymers prevent the movement of elongasome complexes from the bud into the stalk, thereby limiting cell growth to the bud compartment. In the Δ*bacAD* mutant, cells fail to concentrate LmdC at the future stalk base and bud neck. As a consequence, peptidoglycan biosynthesis is no longer limited to the different growth zones, leading to pseudo-stalk formation and unregulated bud expansion. **(B)** Bactofilin-mediated modulation of cell helicity in *R. rubrum*. $BacA_{Rs}$ (yellow) recruits $LmdC_{Rs}$ (red) to the inner cell curvature. The hydrolytic activity of LmdC ultimately stimulates peptidoglycan biosynthesis at this position, leading to a reduction in cell helicity.